

---

Electronic Thesis and Dissertation Repository

---

3-28-2013 12:00 AM

## Magnetic resonance imaging of brain tissue abnormalities: transverse relaxation time in autism and Tourette syndrome and development of a novel whole-brain myelin mapping technique


Yann Gagnon  
*The University of Western Ontario*

Supervisor  
Drs. Jean Théberge  
*The University of Western Ontario* Joint Supervisor  
Rob Nicolson  
*The University of Western Ontario*

Graduate Program in Medical Biophysics  
A thesis submitted in partial fulfillment of the requirements for the degree in Doctor of  
Philosophy

© Yann Gagnon 2013

Follow this and additional works at: <https://ir.lib.uwo.ca/etd>

 Part of the [Developmental Neuroscience Commons](#), [Medical Biophysics Commons](#), [Mental Disorders Commons](#), and the [Neurosciences Commons](#)

---

### Recommended Citation

Gagnon, Yann, "Magnetic resonance imaging of brain tissue abnormalities: transverse relaxation time in autism and Tourette syndrome and development of a novel whole-brain myelin mapping technique" (2013). *Electronic Thesis and Dissertation Repository*. 1189.  
<https://ir.lib.uwo.ca/etd/1189>

This Dissertation/Thesis is brought to you for free and open access by Scholarship@Western. It has been accepted for inclusion in Electronic Thesis and Dissertation Repository by an authorized administrator of Scholarship@Western. For more information, please contact [wlsadmin@uwo.ca](mailto:wlsadmin@uwo.ca).

**Magnetic resonance imaging of brain tissue abnormalities: transverse relaxation time in autism and Tourette syndrome and development of a novel whole-brain myelin mapping technique**

(Thesis format: Monograph)

by

Yann S. Gagnon

Faculty of Medicine and Dentistry  
Department of Medical Biophysics

Submitted in partial fulfillment  
of the requirements for the degree of  
Doctor of Philosophy

The School of Graduate and Postdoctoral Studies  
The University of Western Ontario  
London, Ontario, Canada

March 28, 2013

© Yann S. Gagnon, 2013

## Abstract

The transverse relaxation time (T2) is a fundamental parameter of magnetic resonance imaging sensitive to tissue microstructure and its water content, thus offering a non-invasive approach to evaluate abnormalities of brain tissue *in-vivo*. Prevailing hypotheses of two childhood psychiatric disorders were tested using quantitative T2 imaging and automated region of interest analyses. In autism, the under-connectivity theory, which proposes aberrant connectivity within white matter (WM), was assessed, finding T2 to be elevated in the WM of the frontal and parietal lobes, while dividing whole brain data into neurodevelopmentally relevant WM compartments found increased T2 in bridging and radiate WM. In Tourette syndrome, tissue abnormalities of deep gray matter structures implicated in the symptomology of this disorder were evaluated and increased T2 of the caudate was found.

Despite the sensitivity of quantitative T2 measurements to underlying pathophysiology, interpretation remain difficult. However, in WM, the compartmentalization of distinct water environments may lead to the detection of multi-exponential T2 decay. The metric of interest is principally the myelin water fraction (MWF), which is the proportion of the T2 signal arising from water trapped within layers of the myelin sheath.

As a proof of concept study, the ability to measure the MWF based on T2\* decay was evaluated and compared to a MWF measurements obtained from T2 decay. Data were analysed using both non-negative least squares and a two-pool model. Signal losses near sources of magnetic field inhomogeneity, such as the sinuses, rendered T2\* components inseparable, invalidating this approach for whole brain MWF measurements. However, this study demonstrated the suitability of a two-pool model to calculate the MWF in WM.

A novel approach, based on the multi-component gradient echo sampling of spin echoes (mcGESSE) and a two-pool model of WM, is proposed and its feasibility demonstrated using simulations. The *in-vivo* implementation of mcGESSE followed, with reproducibility of MWF measurements being assessed and the potential of an accelerated protocol using parallel imaging being investigated. While further work is needed to assess data quality, this approach shows great potential to obtain whole brain MWF data within a clinically relevant scan time.

**Keywords:** autism, Tourette Syndrome, under-connectivity, white matter, transverse relaxation, T2, multi-component, myelin water fraction

## Co-Authorship

This thesis contains material from manuscripts either submitted or in preparation for submission.

For the studies of chapter 2 investigating transverse relaxation times in autism and Tourette syndrome, Drs. Nicolson and Williamson completed the psychiatric evaluations and subject recruitment; Ms. Hendry and Drs. DeVito, Drost and Gelman designed the MRI acquisition protocol; Drs. DeVito, Drost, Gelman and Nicolson as well as Ms. Hendry acquired subject data; Dr. Rajakumar provided feedback and guidance in the context of neuroanatomy both in the study design as well as the following analyses. With feedback and guidance from Ms. Hendry, Densmore and Drs. Nicolson and Théberge, I designed and performed the data analyses, including the development of all computer code, and wrote the manuscripts.

For the study of chapter 3 assessing the feasibility of obtaining myelin water fraction measurements using a gradient echo sequence, data were acquired by Dr. DeVito and myself; Drs. Drost, Théberge, and Gelman provided technical feedback and guidance. I developed the computer code and performed all data analyses, under the supervision of Drs. Théberge and Nicolson.

For the study of chapter 3 assessing the feasibility of quantifying the myelin water fraction using multi-component gradient echo sampling of spin echoes (mcGESSE) using simulations, I developed the theory, the acquisition strategy, the computer code used for the simulations, and the data fitting routine under the supervision of Drs. Théberge and Nicolson.

For the study of chapter 4, outlining the *in vivo* implementation of mcGESSE, I performed the pulse sequence programming, designed the acquisition protocol, improved the data fitting routine with the technical guidance of Dr. Théberge. I recruited all study participants, acquired all imaging data and performed all analyses, under the supervision of Drs. Théberge and Nicolson.

## Acknowledgments

I am indebted to the many who have made my journey possible. Foremost, I wish to thank my supervisors, Dick Drost, Rob Nicolson and Jean Théberge, who stepped in upon the retirement of Dr. Drost. Their patience and support have allowed me to explore these projects with independence and autonomy.

I offer my regards to all those who contributed to this work with feedback, criticism, code snippets, or difficult questions.

I would like to acknowledge the financial support I received through the University of Western Ontario, Autism Ontario and the Ontario Mental Health Foundation.

I am forever grateful to my family and friends for their emotional support throughout my graduate studies. And most of all, my loving and encouraging wife Rae-Anne, who stands by me with unwavering support through all my endeavours.

# Contents

|   |            |
|---|------------|
| <b>Abstract</b>   | <b>ii</b>  |
| <b>Co-Authorship</b>  | <b>iv</b>  |
| <b>Acknowledgements</b>   | <b>v</b>   |
| <b>List of Tables</b>   | <b>xi</b>  |
| <b>List of Figures</b>  | <b>xii</b> |
| <b>List of Acronyms &amp; Abbreviations</b>                                 | <b>xiv</b> |
| <b>1 Autism, Tourette Syndrome and MRI</b>                                  | <b>1</b>   |
| 1.1 Thesis introduction . . . . .   | 1          |
| 1.2 Autism . . . . .  | 3          |
| 1.2.1 Background . . . . .  | 3          |
| 1.2.2 Characteristics of autism . . . . .                                   | 4          |
| 1.2.3 Magnetic resonance imaging in autism . . . . .                        | 5          |
| 1.2.4 The under-connectivity hypothesis . . . . .                           | 7          |
| 1.2.5 Neurodevelopment and myelination . . . . .                            | 8          |
| 1.2.6 Summary . . . . .   | 11         |
| 1.3 Tourette Syndrome . . . . .   | 11         |
| 1.3.1 Background . . . . .  | 11         |
| 1.3.2 Magnetic resonance imaging in Tourette Syndrome . . . . .             | 12         |
| 1.3.3 Implication of the cortico-striato-thalamo-cortical circuit . . . . . | 12         |
| 1.3.4 Summary . . . . .   | 13         |
| 1.4 Magnetic Resonance Imaging . . . . .                                    | 14         |
| 1.4.1 Fundamentals of Nuclear Magnetic Resonance . . . . .                  | 14         |
| 1.4.2 The Bloch Equations . . . . .   | 18         |
| 1.4.3 Imaging gradients . . . . .   | 21         |
| 1.4.4 Transverse relaxation <i>in vivo</i> . . . . .                        | 25         |
| 1.4.5 Quantitative T2 . . . . .   | 26         |

|          |  |           |
|----------|--|-----------|
| 1.4.6    | Summary . . . . .  | 28        |
| <b>2</b> | <b>Investigating T2 in autism and Tourette Syndrome</b>                  | <b>29</b> |
| 2.1      | T2 abnormalities of white matter in autism . . . . .                     | 29        |
| 2.1.1    | Introduction . . . . .   | 29        |
| 2.1.2    | Methods . . . . .  | 31        |
| 2.1.2.1  | Subjects . . . . .   | 31        |
| 2.1.2.2  | MRI acquisition . . . . .  | 33        |
| 2.1.2.3  | Image reconstruction and registration . . . . .                          | 33        |
| 2.1.2.4  | Mean lobar T2 calculations . . . . .                                     | 35        |
| 2.1.2.5  | Mean compartmental T2 calculations . . . . .                             | 37        |
| 2.1.2.6  | Statistical analysis . . . . .   | 37        |
| 2.1.3    | Results . . . . .  | 40        |
| 2.1.3.1  | Lobar . . . . .  | 41        |
| 2.1.3.2  | Compartmental . . . . .  | 42        |
| 2.1.4    | Discussion . . . . .   | 43        |
| 2.1.4.1  | Limitations . . . . .  | 43        |
| 2.1.4.2  | Relevance to other imaging studies . . . . .                             | 45        |
| 2.1.5    | Conclusion . . . . .   | 47        |
| 2.2      | T2 abnormalities of the basal ganglia in Tourette syndrome . . . . .     | 47        |
| 2.2.1    | Introduction . . . . .   | 47        |
| 2.2.2    | Methods . . . . .  | 48        |
| 2.2.2.1  | Subjects . . . . .   | 48        |
| 2.2.2.2  | MRI acquisition, image reconstruction and image registration . . . . .   | 49        |
| 2.2.2.3  | Mean T2 measurements . . . . .   | 49        |
| 2.2.2.4  | Statistical analysis . . . . .   | 50        |
| 2.2.3    | Results . . . . .  | 50        |
| 2.2.4    | Discussion . . . . .   | 53        |
| 2.2.5    | Conclusion . . . . .   | 55        |
| 2.3      | Summary . . . . .  | 55        |
| <b>3</b> | <b>Multi-component T2 in white matter and myelin mapping</b>             | <b>56</b> |
| 3.1      | Introduction . . . . .   | 56        |
| 3.2      | Multi-component T2 in human white matter . . . . .                       | 57        |
| 3.2.1    | Compartment model . . . . .  | 57        |
| 3.2.2    | Water exchange . . . . .   | 58        |
| 3.2.3    | T2 relaxation of brain tissue . . . . .                                  | 58        |
| 3.3      | Current multi-component T2 and myelin water mapping strategies . . . . . | 60        |
| 3.3.1    | mcT2: an ill-posed mathematical problem . . . . .                        | 60        |
| 3.3.2    | Spin echo based methods . . . . .  | 61        |
| 3.3.2.1  | Optimized single slice MESE as the gold standard . . . . .               | 61        |



|     |         |  |    |
|-----|---------|--|----|
|     | 3.3.2.2 | Linear combination of spin echoes . . . . .  | 62 |
|     | 3.3.2.3 | MESE with variable TR . . . . .  | 64 |
|     | 3.3.2.4 | T2 prep . . . . .  | 64 |
|     | 3.3.2.5 | MESE with stimulated echo correction . . . . .   | 65 |
|     | 3.3.2.6 | MESE with 3D GRASE . . . . .   | 65 |
|     | 3.3.3   | Gradient echo based methods . . . . .  | 66 |
|     | 3.3.4   | Steady state based methods . . . . .   | 67 |
| 3.4 | mcT2*   | <i>in vivo</i> : feasibility study . . . . .   | 67 |
|     | 3.4.1   | Introduction . . . . .   | 67 |
|     | 3.4.2   | Methods . . . . .  | 68 |
|     | 3.4.2.1 | Study subject and MRI acquisition . . . . .  | 68 |
|     | 3.4.2.2 | Data analysis . . . . .  | 70 |
|     | 3.4.3   | Results . . . . .  | 71 |
|     | 3.4.4   | Discussion . . . . .   | 72 |
|     | 3.4.5   | Conclusion . . . . .   | 80 |
| 3.5 |         | Feasibility of MWF quantification using gradient echo sampling of spin<br>echoes . . . . . | 81 |
|     | 3.5.1   | Introduction . . . . .   | 81 |
|     | 3.5.2   | Theory . . . . .   | 81 |
|     | 3.5.3   | Methods . . . . .  | 83 |
|     | 3.5.3.1 | Simulated model parameters . . . . .   | 83 |
|     | 3.5.3.2 | Simulated mcGESSE acquisition parameters . . . . .   | 86 |
|     | 3.5.3.3 | SNR . . . . .  | 86 |
|     | 3.5.3.4 | Iteratively re-weighted robust least squares . . . . .                                     | 87 |
|     | 3.5.3.5 | Simulations . . . . .  | 88 |
|     | 3.5.4   | Results . . . . .  | 89 |
|     | 3.5.4.1 | Inspection of previous 3T gradient echo image . . . . .                                    | 89 |
|     | 3.5.4.2 | Starting estimates . . . . .   | 89 |
|     | 3.5.4.3 | Sampling density and receiver bandwidth . . . . .  | 89 |
|     | 3.5.4.4 | SNR . . . . .  | 92 |
|     | 3.5.4.5 | Static dephasing (T2') . . . . .   | 92 |
|     | 3.5.5   | Discussion . . . . .   | 93 |
|     | 3.5.5.1 | Summary of results . . . . .   | 93 |
|     | 3.5.5.2 | Two-pool model . . . . .   | 94 |
|     | 3.5.5.3 | Influence of starting estimates . . . . .  | 95 |
|     | 3.5.5.4 | <i>In-vivo</i> implementation and SNR . . . . .  | 95 |
|     | 3.5.6   | Conclusion . . . . .   | 97 |
| 3.6 |         | Summary . . . . .  | 97 |

|          |  |            |
|----------|--|------------|
| <b>4</b> | <b>Myelin mapping of the human brain using mcGESSE</b>           | <b>100</b> |
| 4.1      | Introduction . . . . .   | 100        |
| 4.2      | Methods . . . . .  | 103        |
| 4.2.1    | Pulse sequence development and MR data acquisition . . . . .     | 103        |
| 4.2.2    | Subjects . . . . .   | 105        |
| 4.2.3    | mcGESSE data analysis . . . . .                                  | 105        |
| 4.2.4    | Image normalization and segmentation . . . . .                   | 106        |
| 4.2.5    | Creation of ROI . . . . .  | 107        |
| 4.2.6    | Statistical analysis . . . . .                                   | 108        |
| 4.3      | Results . . . . .  | 108        |
| 4.4      | Discussion . . . . .   | 114        |
| 4.4.1    | Relevance of previous simulations study . . . . .                | 115        |
| 4.4.2    | Filtering . . . . .  | 116        |
| 4.4.3    | Field inhomogeneities . . . . .                                  | 117        |
| 4.4.4    | Image segmentation and normalization . . . . .                   | 118        |
| 4.4.5    | MWF distributions . . . . .                                      | 119        |
| 4.4.6    | High-field imaging of white matter . . . . .                     | 121        |
| 4.4.7    | Accelerated protocol using parallel imaging . . . . .            | 121        |
| 4.4.8    | Future work . . . . .  | 121        |
| 4.5      | Conclusion . . . . .   | 122        |
| <b>5</b> | <b>Conclusions and summary</b>                                   | <b>123</b> |
| 5.1      | T2 abnormalities in autism . . . . .                             | 124        |
| 5.2      | T2 abnormalities in Tourette syndrome . . . . .                  | 125        |
| 5.3      | Feasibility of mcT2* <i>in vivo</i> for myelin mapping . . . . . | 125        |
| 5.4      | Feasibility of mcGESSE for myelin mapping: simulations . . . . . | 126        |
| 5.5      | Myelin mapping <i>in vivo</i> using mcGESSE . . . . .            | 127        |
| 5.6      | Significance of this work . . . . .                              | 128        |
| 5.7      | Future work . . . . .  | 129        |
|          | <b>Bibliography</b>  | <b>130</b> |
|          | References . . . . .   | 130        |
|          | <b>Appendices</b>  | <b>154</b> |
|          | <b>I Power image noise correction</b>                            | <b>155</b> |
|          | <b>II Iteratively re-weighted robust least squares</b>           | <b>157</b> |
|          | <b>III Ethics approval for the study of autism using MRI</b>     | <b>158</b> |
|          | <b>IV Ethics approval for the study of TS using MRI</b>          | <b>159</b> |

|   |            |
|---|------------|
| <b>V Ethics approval for pulse sequence development</b> | <b>160</b> |
| <b>Vita</b>   | <b>161</b> |

# List of Tables

|     |   |     |
|-----|---|-----|
| 2.1 | Subject demographics . . . . .                                      | 41  |
| 2.2 | Mean Lobar T2 results . . . . .                                     | 42  |
| 2.3 | Mean WM compartment T2 results . . . . .                            | 42  |
| 2.4 | Subject demographics . . . . .                                      | 52  |
| 2.5 | Mean basal ganglia T2 results . . . . .                             | 53  |
| 3.1 | MESE and MEGE acquisition parameters . . . . .                      | 70  |
| 3.2 | Simulation parameters to assess starting estimates . . . . .        | 90  |
| 3.3 | Sampling density/receiver bandwidth simulation parameters . . . . . | 91  |
| 3.4 | SNR simulation parameters . . . . .                                 | 92  |
| 3.5 | Degree of static dephasing simulation parameters . . . . .          | 93  |
| 4.1 | mcGESSE acquisition parameters . . . . .                            | 104 |
| 4.2 | Details of ROIs used . . . . .                                      | 107 |
| 4.3 | KS-test results for scan-rescan data . . . . .                      | 114 |
| 4.4 | KS-test results for accelerated acquisition . . . . .               | 115 |

# List of Figures

|      |  |    |
|------|--|----|
| 1.1  | Conceptual schematic of under-connectivity . . . . .                                       | 8  |
| 1.2  | Anatomical lobar division of the brain . . . . .   | 9  |
| 1.3  | Simple model and electron-micrograph of a myelinated axon. . . . .                         | 10 |
| 1.4  | Anatomical organization of major white matter tracts . . . . .                             | 10 |
| 1.5  | Schematic of the cortico-striato-thalamo-cortical circuitry . . . . .                      | 13 |
| 1.6  | Larmor precession of the magnetic moment vector . . . . .                                  | 15 |
| 1.7  | Alignment of spin populations . . . . .  | 15 |
| 1.8  | The magnetization isochromat as the net magnetization vector of a spin population. . . . . | 17 |
| 1.9  | Excitation of the macroscopic magnetization . . . . .                                      | 19 |
| 1.10 | Relaxation of the macroscopic magnetization . . . . .                                      | 19 |
| 1.11 | Slice selection gradient . . . . .   | 22 |
| 1.12 | Gradient echo pulse sequence . . . . .   | 24 |
| 1.13 | K-space data and the corresponding image . . . . .   | 25 |
| 1.14 | Spin echo pulse sequence and signal . . . . .  | 27 |
|      |  |    |
| 2.1  | GESFIDE pulse sequence diagram . . . . .   | 34 |
| 2.2  | Flowchart of image reconstruction and registration . . . . .                               | 36 |
| 2.3  | Lobar regions of interests and white matter probability maps . . . . .                     | 38 |
| 2.4  | Flowchart of image reconstruction and registration . . . . .                               | 39 |
| 2.5  | Bridging, sagittal and radiate WM ROIs . . . . .   | 40 |
| 2.6  | Flowchart of image reconstruction and registration . . . . .                               | 51 |
| 2.7  | Basal ganglia regions of interest . . . . .  | 52 |
|      |  |    |
| 3.1  | Compartment model in white matter . . . . .  | 57 |
| 3.2  | T2 distribution in white matter . . . . .  | 59 |
| 3.3  | MESE <sub>ss</sub> pulse sequence diagram . . . . .  | 63 |
| 3.4  | MEGE pulse sequence diagram. . . . .   | 69 |
| 3.5  | Slice location and frontal sinuses. . . . .  | 72 |
| 3.6  | Series of T2-weighted images . . . . .   | 73 |
| 3.7  | Series of T2*-weighted images . . . . .  | 74 |

|      |   |     |
|------|---|-----|
| 3.8  | Filtered T2-weighted image and relaxation maps. . . . .                 | 75  |
| 3.9  | Spin echo myelin water fraction maps . . . . .                          | 75  |
| 3.10 | T2* histogram . . . . .   | 76  |
| 3.11 | Gradient echo MWF maps . . . . .  | 76  |
| 3.12 | Symmetric gradient echo sampling of the spin echo . . . . .             | 84  |
| 3.13 | $s_{ratio}$ as an objective function . . . . .                          | 85  |
| 3.14 | Results simulations with various starting points. . . . .               | 90  |
| 3.15 | Results simulations with various sampling and bandwidths . . . . .      | 91  |
| 3.16 | Results simulations with various SNR. . . . .                           | 93  |
| 3.17 | Results simulations with various static dephasing. . . . .              | 94  |
| 4.1  | mcGESSE whole brain data . . . . .                                      | 109 |
| 4.2  | MWF in grey and white matter ROIs. . . . .                              | 110 |
| 4.3  | Cerebral grey and white matter MWF . . . . .                            | 110 |
| 4.4  | Scatterplots of within subject inter-scan reproducibility. . . . .      | 111 |
| 4.5  | MWF distributions in cerebral grey and white matter. . . . .            | 112 |
| 4.6  | Scatterplots of the accelerated vs. the unaccelerated protocol. . . . . | 113 |

# List of Acronyms & Abbreviations

|            |  |
|------------|--|
| 1-H        | most common hydrogen isotope                   |
| 2D         | two-dimensional                                |
| 3D         | three-dimensional                              |
| 1.5T       | operating field strength of 1.5 Tesla          |
| 3T         | operating field strength of 3.0 Tesla          |
| $\gamma$   | gyromagnetic ratio                             |
| $\omega_0$ | Larmor frequency                               |
| $\tau_c$   | correlation time                               |
| $\Theta$   | flip angle                                     |
| $A_{bl}$   | amplitude of baseline signal                   |
| $A_{ie}$   | amplitude of intra-extra cellular water signal |
| $A_{my}$   | amplitude of myelin water signal               |
| ADC        | analogue to digital converter                  |
| ADF        | anisotropic diffusion filter                   |
| ADHD       | attention deficit hyperactivity disorder       |
| ADI-R      | Autism Diagnostic Interview-Revised            |
| ADOS-R     | Autism Diagnostic Observation Schedule-Revised |
| ANCOVA     | analysis of covariance                         |
| ANOVA      | analysis of variance                           |
| $B_0$      | external, static magnetic field                |
| $B_1$      | radio-frequency field                          |

|           |  |
|-----------|--|
| BPP       | Bloembergen-Purcell-Pound  |
| CSF       | cerebrospinal fluid  |
| CSTC      | cortico-striato-thalamo-cortial  |
| df        | degrees of freedom   |
| DESPOT1   | Driven equilibrium single pulse observation of T1                          |
| DESPOT2   | Drive equilibrium single pulse observation of T2                           |
| DSM-IV-TR | Diagnostic and Statistical Manual of Mental Disorders-Text Revision        |
| DTI       | Diffusion tensor imaging   |
| E         | energy difference of spin states   |
| EMF       | electro-motive force   |
| FA        | fractional anisotropy  |
| fMRI      | functional magnetic resonance imaging                                      |
| $G_{pe}$  | applied magnetic field gradient for phase-encoding                         |
| $G_{ro}$  | applied magnetic field gradient for frequency readout                      |
| $G_x$     | applied magnetic field gradient in the x-direction                         |
| $G_y$     | applied magnetic field gradient in the y-drection                          |
| $G_{ss}$  | slice selection gradient   |
| GESFIDE   | gradient echo sampling of the free-induction decay and echo                |
| h         | Planck's constant  |
| Hz        | Hertz  |
| IRRLS     | iteratively re-weighted robust least squares                               |
| IQ        | intellectual quotient  |
| $k_x$     | spatial frequency in x-direction   |
| $k_y$     | spatial frequency in y-direction   |
| k         | Boltzmann's constant   |
| K         | correlation time proportionality constant                                  |
| KS        | Kolmogorov-Smirnov   |
| K-SADS    | Schedule for Affective Disorders and Schizophrenia for School-Age Children |



|                    |  |
|--------------------|--|
| $MAD$              | mean absolute deviation  |
| MHz                | mega Hertz   |
| $M_0$              | equilibrium magnetization  |
| $M_{xy}$           | transverse magnetization   |
| $M_x$              | x-component of the magnetization   |
| $M_y$              | y-component of the magnetization   |
| $M_z$              | longitudinal magnetization   |
| mcDESPOt           | multi-component driven equilibrium single pulse observation of T1 and T2 |
| mcGESSE            | multi-component gradient echo sampling of spin echoes                    |
| mcT2               | multi-component T2   |
| mcT2*              | multi-component T2*  |
| ms                 | milliseconds   |
| MEGE               | multi-echo gradient echo   |
| MESE               | multi-echo spin echo   |
| MESE <sub>ss</sub> | single slice multi-echo spin echo  |
| MRI                | magnetic resonance imaging   |
| MRS                | magnetic resonance spectroscopy  |
| MS                 | multiple sclerosis   |
| MTR                | magnetization transfer ratio   |
| MWF                | myelin water fraction  |
| $N_-$              | upper (spin down) energy state of the spin population                    |
| $N_+$              | lower (spin up) energy state of the spin population                      |
| NAA                | N-acetyl-aspartate   |
| NNLS               | non-negative least squares   |
| OCD                | obsessive compulsive disorder  |
| PET                | positron emission tomography   |
| px                 | pixel  |
| R2                 | transverse relaxation rate   |

|                          |   |
|--------------------------|---|
| R2*                      | effective transverse relaxation rate                            |
| R2'                      | reversible transverse relaxation rate                           |
| rBW                      | receiver bandwidth  |
| ROI                      | region of interest  |
| RF                       | radio-frequency   |
| rNLS                     | regularized non-negative least squares                          |
| <i>s<sub>ratio</sub></i> | spin echo envelope signal ratio                                 |
| SAR                      | specific absorption rate  |
| SNR                      | signal to noise ratio   |
| T                        | Tesla   |
| $T_K$                    | temperature in Kelvins  |
| T1                       | longitudinal relaxation time                                    |
| T2                       | transverse relaxation time                                      |
| T2*                      | effective transverse relaxation time                            |
| T2'                      | reversible transverse relaxation time                           |
| T2 <sub>ie</sub>         | intra-extra cellular water transverse relaxation time           |
| T2 <sub>my</sub>         | myelin water transverse relaxation time                         |
| T2* <sub>ie</sub>        | intra-extra cellular water effective transverse relaxation time |
| T2* <sub>my</sub>        | myelin water effective transverse relaxation time               |
| TE                       | echo time   |
| TR                       | repetition time   |
| TS                       | Tourette syndrome   |
| voxel                    | volume element  |
| WISC-III                 | Wechsler Intelligence Scale for Children, 3rd edition           |
| WMPM                     | white matter parcellation map                                   |
| YGTSS                    | Yale Global Tic Severity Scale                                  |

# Chapter 1

## Autism, Tourette Syndrome and MRI

### 1.1 Thesis introduction

The flexibility afforded by magnetic resonance imaging (MRI) has enabled continuing innovation in the study of the human brain. This thesis describes a series of projects which seek to better understand brain tissue abnormalities in autism and Tourette syndrome (TS); two psychiatric conditions with childhood onsets. Further, the work presented extends on current MRI methodologies used in quantitative brain imaging with a focus on myelin, a component of brain tissue critical for proper neurotransmission. This introductory section serves to describe the organization of this thesis as well as the aim and scope of each chapter.

Chapter 1 is devoted to introductory material of the subject matter. Descriptions of autism and TS highlight the developmental nature of the disorder, as well as summarize what is known about their onset, prevalence and co-morbidities. Current evidence of brain dysfunction and tissue abnormalities is summarized within the scope of MRI research. This review of the state of research in autism and TS sets

the stage for our own imaging findings, presented in chapter 2. The last section of chapter 1 covers the fundamentals of MRI physics and sets the foundation for the novel MRI methodology presented in chapters 3 and 4.

Chapter 2 presents studies which use existing methodologies for the measurement of the transverse relaxation time (T2), a parameter of MRI sensitive to cellular structure and water content, is employed to investigate both autism and TS. Novel approaches to perform automated, atlas-based, group comparisons are described and implemented. The results are discussed in light of their implications and limitations, which motivate the work presented in chapters 3 and 4.

Chapter 3 is concerned with the quantitative assessment of the myelin water fraction (MWF), a metric which describes the proportion of the T2 signal attributable to motionally restricted water found between layers of the myelin sheath. First, existing methods for MWF quantification are reviewed. A short proof of concept study is then presented based on a method which had, at the time, never been implemented *in vivo*. However, we conclude that shortcomings restrict application to *in vivo* studies within our lab's research program. A new approach is proposed, based on a novel sampling strategy and addressing drawbacks of previous methods. Termed mcGESSE (multi-component gradient echo sampling of spin echoes), its ability to measure the MWF is assessed with computer simulations using realistic temporal signal to noise (SNR) profiles and acquisition parameters.

Chapter 4 describes the implementation of mcGESSE for whole brain MWF mapping in a clinically relevant scan time on our lab's 3T MRI scanner. Parameters gleaned from the simulation studies of chapter 3 were combined with specific considerations of *in vivo* imaging to establish a preferred protocol. Healthy volunteers underwent imaging, with all subjects but one being imaged twice to assess repro-

ducibility of MWF measurements. Additionally, the feasibility of an accelerated protocol, using parallel imaging, was assessed in a subset of volunteers with a third scan. Image and data quality issues are discussed in light of their influence on MWF measurements. Specific suggestions are made in this regard for future work to address these issues.

Chapter 5 presents concise summaries of each study presented in this thesis. The results of T2 abnormalities in autism and TS are summarized and related to current findings. The methodological studies of chapter 3 and 4 are also summarized and their contributions assessed on their own merit. The chapter ends with final views on the implications of whole-brain MWF mapping in the study of autism.

## **1.2 Autism**

### **1.2.1 Background**

Autism is a childhood-onset neurodevelopmental disorder which has received increasing public, media and legislative attention in the past decade. The first description of autism was published in Leo Kanner's seminal paper in 1943 [1], describing the case studies of 11 children. To this day, many of the observations described by Kanner in this small group remain remarkably relevant and the traits he described are still hallmarks of the current diagnostic criteria [2].

Many factors have contributed to the reported rise in the prevalence of autism [3]. These include, but are not limited to, a broadening of the diagnostic criteria, changes in public health policy and referral processes, and a decreasing age of diagnosis [3]. It is however unclear if these factors can fully account for the increase. Current

estimates of today's prevalence vary widely and the most recent Canadian epidemiological study was conducted in Montreal, Québec, and found a rate of approximately 22 cases in 10 000 children [4]. Additionally, autism is more common in males in a ratio of about 4 to 1 [5]. Autism also has a high-comorbidity with other conditions such as mental retardation and epilepsy [3, 6, 7] .

Autism is a disabling condition with the lifetime public expenditure estimate to be \$3.2 million per person (United States dollars) [8]. Additionally, raising a child with autism places a tremendous burden on families, and higher levels of family stress, reduced family income, and increased rates of divorce have been reported among parents and families of children with autism [9, 10].

### **1.2.2 Characteristics of autism**

Autism is characterized by a triad of impairments, namely social deficits, impaired communication and restricted and repetitive patterns of behaviour [5, 11]. These areas of deficits were discussed and conceptually grouped in Kanner's original paper in terms of aloneness, sameness, rigidity and atypical language use [1, 5]. All facets of social functioning can be affected in autism. For example, difficulties with face recognition, eye gaze and the understanding of social cues are abilities often affected. Even at a very young age, toddlers with autism may refuse to play with others or simply ignore those in their surroundings. Deficits in communication beyond language delay are also observed. Involuntary and immediate repetition of sounds and vocalizations made by others (echolalia) and the misuse of pronouns are two common examples. Interestingly, some skills often associated with language performance are sometimes unaffected or even enhanced, such as memory, vocabulary and spelling. Certain patterns of behaviour in autism are often observed to be restricted and repetitive. For example, an individual may resist changes, such as the furniture arrangement in a

room, or changes to a daily routine. Repetitive behaviours are also often exhibited which may include performing the same task over and over or repeating previously heard phrases. Due to the spectral nature of the disorder, there is great variation in breadth and range in all deficit areas and not all areas need to be affected for a diagnosis [2].

### 1.2.3 Magnetic resonance imaging in autism

There is strong evidence that autism has a neurobiological basis, but the extent and timing of the abnormalities involved in the disorder remain largely unknown. Kan-ner’s discerning observation of increased head circumference was an early suggestion of a neurobiological basis for autism. Increased head size has since been substantiated in many studies assessing head circumference measurements. In fact, about a quarter of children with autism have a head circumference higher than the 97th percentile [5]. Along with sparse post-mortem studies, head circumference studies led to the early notion that overall brain volumes are increased in autism [12].

The advent of MRI has enabled the direct *in vivo* assessment of brain volumes of developing children with autism. Differences in the diagnostic criteria and age of patient cohorts, as well as the analysis methods used to calculate volumes from the imaging data may, in part, explain the many conflicting reports as to the degree and chronological span of reported volume abnormalities. To some extent, inconsistencies in the literature may be explained by an abnormal brain growth trajectory in autism, a notion which has gained increasing traction. Studies investigating this possibility have suggested an early period of accelerated brain overgrowth, compared to peers, followed by a period of normalized growth into adulthood [13–15].

The many studies examining the differential contributions of grey and white

matter to the overall brain enlargement have also failed to reach congruent conclusions [12]. Reports of increased white matter have been more consistent, to some extent, while reports of grey matter volume differences more inconsistently cite increased or no significant differences compared to typically developing children [16]. Studies have found both global and regional differences contributing to the cerebral volume abnormalities seen in grey and white matter in children with autism [16]. One study of young children with autism noted a posterior to anterior gradient, with enlargement of grey and white matter in the frontal lobes but not in the occipital lobes [17]. Another study of young children with autism, however, reported generalized increases in grey and white matter throughout the cerebrum [18].

Functional magnetic resonance imaging (fMRI) studies have used task based studies to reveal differences of brain function in individuals with autism. Extensive evidence exists of abnormal brain function and functional connectivity encompassing all areas of aberrant function in autism. These predominantly include motor tasks, executive function tasks, visual-spatial processing tasks, auditory and language tasks, and both basic and complex social processing and cognition tasks [14, 15, 19]. Age related differences in the processing style, the influence of demands and stimulus, modulation, and the lack of preference for social stimuli are all aspects of brain function which differ in autism when compared to healthy controls [19].

Other quantitative magnetic resonance techniques have been attractive in the investigation of brain abnormalities in autism. Magnetic resonance spectroscopy (MRS) can be used to quantify the relative concentrations of various brain metabolites. N-acetylaspartate (NAA), usually construed as a marker of neuronal integrity and function, has typically been reported to be reduced in autism which does not support hypotheses of neuronal overgrowth or reduced apoptosis [13, 14, 20, 21]. Changes have been reported in other metabolites, such as creatine, glutamate/glutamine and myo-



inositol, but with less consistency [13,14]

Diffusion tensor imaging (DTI) is a technique sensitive to the diffusion characteristics of water within brain tissue microstructure. DTI has been especially amenable to the study of white matter, since the presence of nerve fibre bundles results in geometrically restricted water diffusion. Metrics based on diffusivity and the geometric anisotropy of diffusion, such as fractional anisotropy (FA), are most often reported in studies investigating white matter. DTI publications in autism have undergone quasi exponential growth in recent years. Methodological approaches vary greatly but reductions in FA is the most frequent report [22]. Ensuring robust data and statistical comparisons in DTI is not trivial and processing pipelines are faced with many potential pitfalls [23]. Further, the interpretation of quantitative metrics such as FA calls for caution in light of their dependence on the complex organization of nerve fibres [24].

The reconciliation of imaging findings is hindered by our relatively poor understanding of neurodevelopmental processes. How the underlying brain abnormalities in autism, whether cause of effect, interfere with development is a difficult but critical research question to consider. Healthy brain development is a dynamic process with regional and temporal underpinnings which raises critical considerations in autism research.

#### **1.2.4 The under-connectivity hypothesis**

In imaging research, the attribution of a specific, localized cause of autism has been largely abandoned in favour of the conceptualization of autism as a distributed disorder. A proposed unified concept of deficient complex information processing has been supported by cognitive testing [25] and functional imaging [26,27]. This idea

was recaptured and expanded in terms of aberrant neural connectivity, purported to lead to disruption of psychological or neurological functions that are dependent on the coordination or integration of several brain regions [28–30]. This under-connectivity theory proposes atypical development of the long-distance, integrative connections within and between cortical systems combined with overrepresented short range connections (figure 1.1).

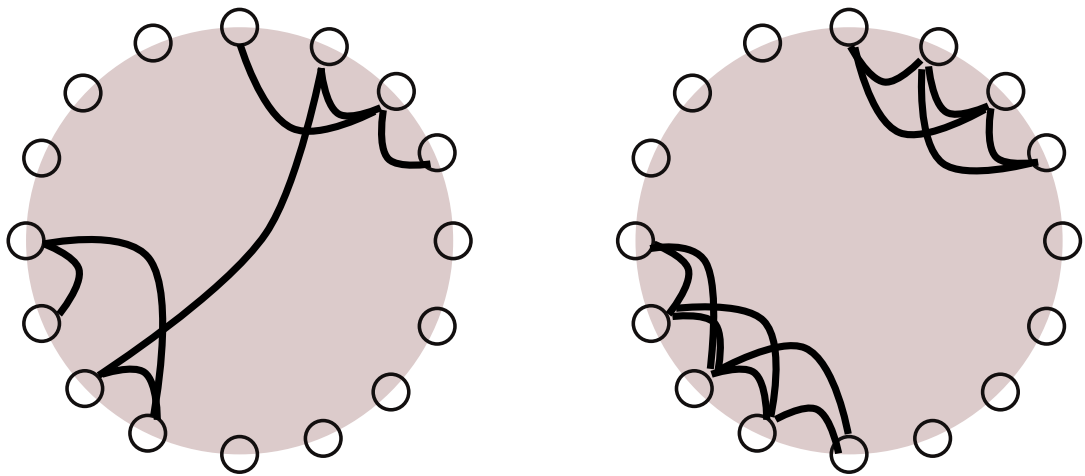


Fig. 1.1: Schematic representing the concept of under-connectivity as proposed by Belmonte et al. A normal brain (left) contrasted to a brain with aberrant connectivity (right).

### 1.2.5 Neurodevelopment and myelination

Reports of white matter abnormalities from MRI studies, and the profile of affected and spared brain functions, support the concept of aberrant connectivity in autism. Many studies have categorized white matter volume abnormalities in autism using the anatomical lobar divisions of the brain (see figure 1.2). However, this approach may not be the most suitable when testing hypotheses of neurodevelopment and functional organization.

Physiologically, white matter is principally distinguished from grey matter by the presence of myelin, consisting of oligodendrocytes, wrapped in a concentric sheath around axons to improve electrical conductivity (figure 1.3) [31]. Formation of the myelin sheath, or myelination, is one of the central underlying processes of brain development and maturation. Myelination begins prenatally and follows a non-uniform spatial and temporal profile [32] until at least adolescence [33].

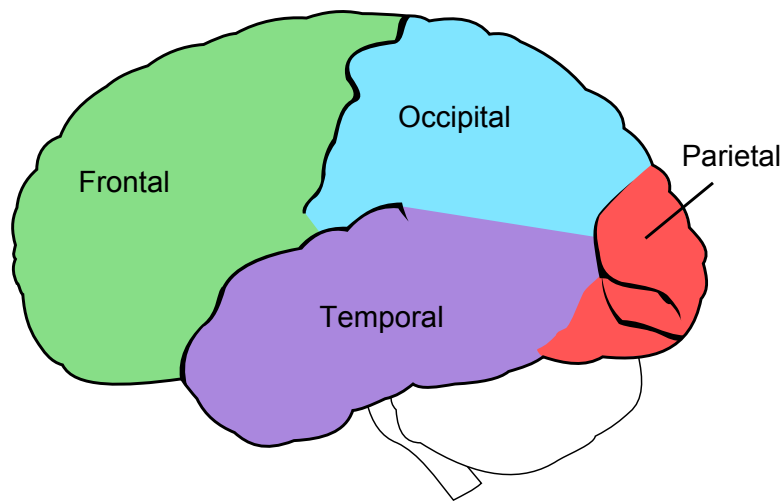


Fig. 1.2: The frontal, occipital, temporal and parietal lobar divisions of the human brain.

The relative bulk alignment of neighbouring myelinated white matter axons results in macroscopic fibre bundles called white matter tracts. These tracts are anatomically categorized into projection, association and commissural white matter fibres (figure 1.4). Within these types, white matter fibre tracts are further divided according to anatomical location and span [34]. Fibre tract organization offers a functionally and neurodevelopmentally relevant classification scheme for the assessment of white matter abnormalities in autism.

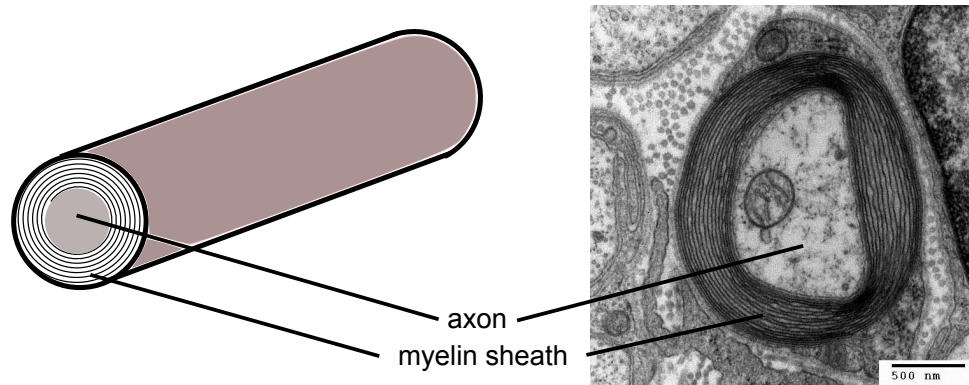


Fig. 1.3: (Left) Simplified model of a myelinated axon, showing the myelin sheath wrapped concentrically around the axon. (Right) Electron-micrograph giving a cross-sectional view of the myelin sheath and axon.

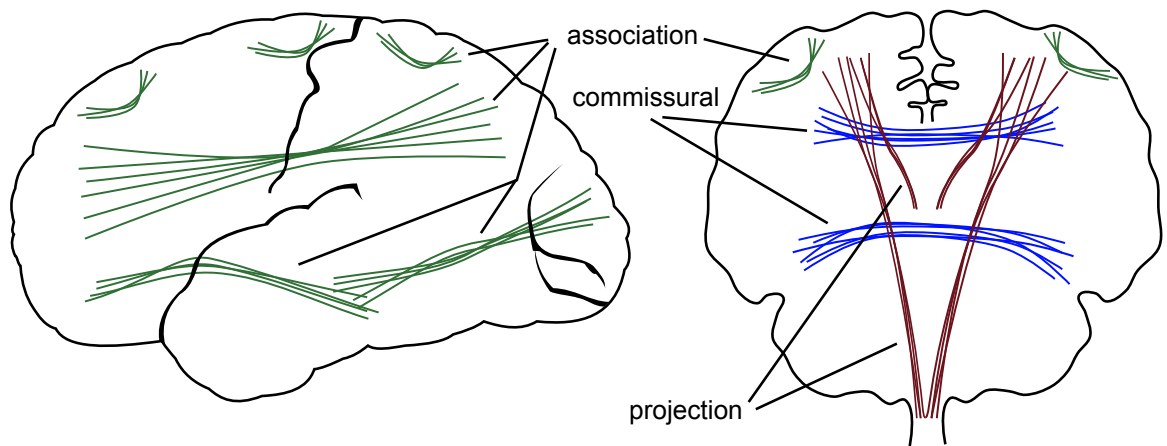


Fig. 1.4: Anatomical organization of major white matter tracts presented in sagittal (left) and coronal (right) views; association fibres (green), commissural fibres (blue) and projection fibres (magenta).

## **1.2.6 Summary**

The study of autism with MRI has lent strong evidence to a neurobiological basis though many research questions remain unanswered. Histological and genetic research in autism have recently undergone significant growth due to the founding of programs such as the Autism Tissue Program [35] and advancement of techniques enabling the identification of genetic abnormalities such as chromosomal abnormalities and copy number variations. However, the lines of research afforded by these methods of basic science alone remain distant to the functional and developmental aspects of autism. To date, no genetic abnormalities have been found to be specific to autism. Instead, it has been suggested that genetic factors may act through some common final neurodevelopmental pathway and that linking genetic information and neuroimaging could help us identify these pathways [36]. In this spirit, the work presented in this thesis gives special consideration to the under-connectivity theory through the investigation of white matter abnormalities in autism.

## **1.3 Tourette Syndrome**

### **1.3.1 Background**

TS is a neuropsychiatric disorder first described by Gilles de la Tourette in 1885, reporting on nine patients who displayed involuntary movements and phonic sounds [37]. TS remains characterized by vocal and motor tics which exhibit a convoluted temporal pattern of severity and frequency. These tics are usually accompanied by sensory symptoms and premonitory urges. The mean age of onset is 6 years of age with the majority of cases developing before age 11 [38]. Severity peaks at about age 12 and most patients are tic-free by the end of adolescence [38]. Once thought to be rare, reports on the phenomenology and prevalence of TS around the world have

shown great similarity. Prevalence in the majority of cultures is around 1%, with variation being explained by methods of ascertainment, differing study populations and clinical criteria [39–42]. However, TS appears to be rarer in females [43] and individuals of black african descent [42]. Comorbidity with other neuropsychiatric conditions such as obsessive-compulsive disorder (OCD) and attention-deficit/hyperactivity disorder (ADHD) is exceedingly common and perhaps as high as 90% [44].

### **1.3.2 Magnetic resonance imaging in Tourette Syndrome**

Neuroimaging studies have provided support for the involvement of various brain structures in the pathophysiology of TS. Studies of brain function using positron emission topography (PET) and fMRI have reported abnormalities of the basal ganglia, thalamus, prefrontal cortex and primary motor area [45–47]. Structural MRI studies have found volumetric reductions of the putamen, caudate and the globus pallidus, as well as abnormal volumetric asymmetry of basal ganglia structures [45, 48]. Additionally, studies have reported volumetric abnormalities of the dorsal prefrontal area [49], frontal white matter [50, 51], and frontal grey matter [51, 52]. Abnormalities of neurochemistry of these regions in TS have also previously been noted: one MRS study found reduced levels of NAA, suggesting reduced functional neuronal integrity, in the frontal lobes and left putamen of patients with TS [53].

### **1.3.3 Implication of the cortico-striato-thalamo-cortical circuit**

Research studies have implicated abnormalities of cortico-striato-thalamo-cortical (CSTC) circuits in the etiology of TS, though the specific neurophysiological abnormalities underlying the disorder remain unknown [54, 55]. CSTC circuits connect the

basal ganglia and related thalamic and cortical structures within multiple networks implicated in many motor, association and inhibitory neural systems (see figure 1.5). Previous work has suggested that TS could be associated with the improper inhibition of subsets of the CSTC circuits [44, 54, 55]. Whether these changes are compensatory in nature or point to the underlying etiology of TS remains an unanswered question.

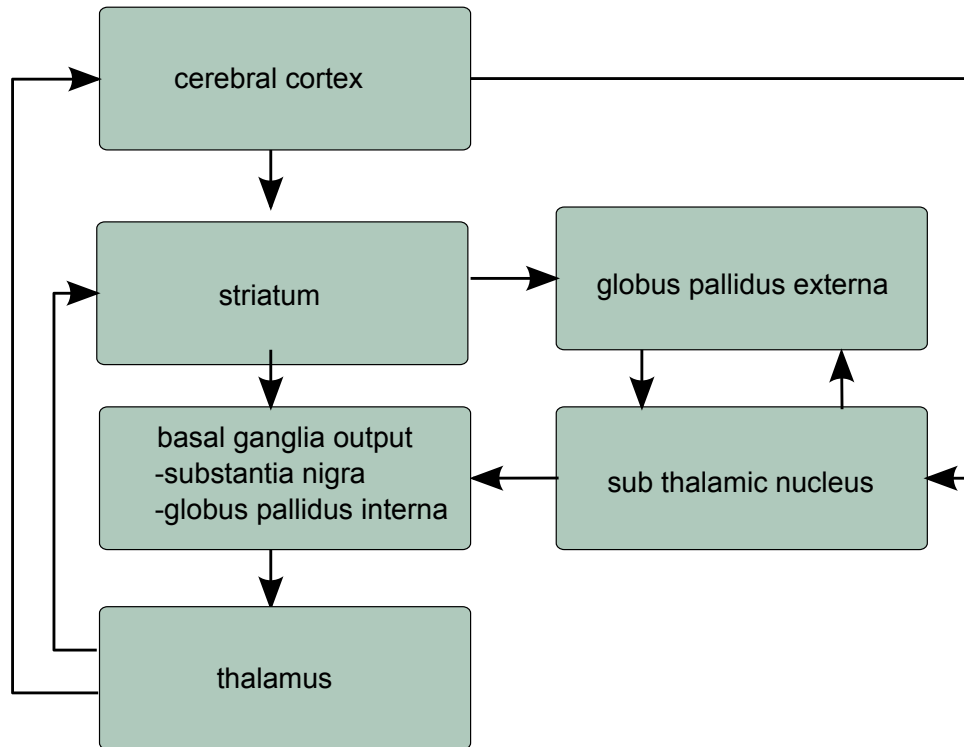


Fig. 1.5: Schematic of the CSTC circuitry proposed as a neural substrate in the etiology of TS.

### 1.3.4 Summary

As with autism research, neuroimaging findings lend strong evidence to aberrant neural function and structure in individuals with TS. Though the heritability of TS and its associated comorbid conditions is high [56], the specifics of the underlying genetic components have not been uncovered [42]. The CSTC circuitry and its pathways

have lent a framework within which to reconcile symptomatology and imaging findings [57]. The research study of TS presented in this thesis aims to further evaluate abnormalities of the basal ganglia by quantitatively assessing T2, given its sensitivity to changes in neurobiology reflected by changes in the tissue microstructure.

## 1.4 Magnetic Resonance Imaging

MRI exploits a fundamental property of the atomic nuclei called “spin”. Though the manifestation of atomic spin is most thoroughly explained by quantum mechanics, the population of spins required to give rise to a detectable signal is large enough to render a description of MRI using classical mechanics appropriate. In the case of hydrogen, a single unpaired proton results in a net nuclear spin of  $1/2$ . The natural concentration of water molecules in the human body has led to hydrogen being the primary nuclei of interest in MRI, termed proton or 1-H imaging. However, other nuclei present in the human body have a net non-zero spin and can also be used as a source of signal. The rest of this section will describe the basic concepts which make MRI possible.

### 1.4.1 Fundamentals of Nuclear Magnetic Resonance

The hydrogen nuclei possesses a magnetic moment represented by a vector which interacts with an external magnetic field. Two energy states are possible, corresponding to an alignment against and with the external field. This is further characterized by precession of the nucleus’ magnetic moment, about the direction of the external field, known as Larmor precession (figure 1.6).

The alignment of the nuclei’s magnetic moment vector with or against the external



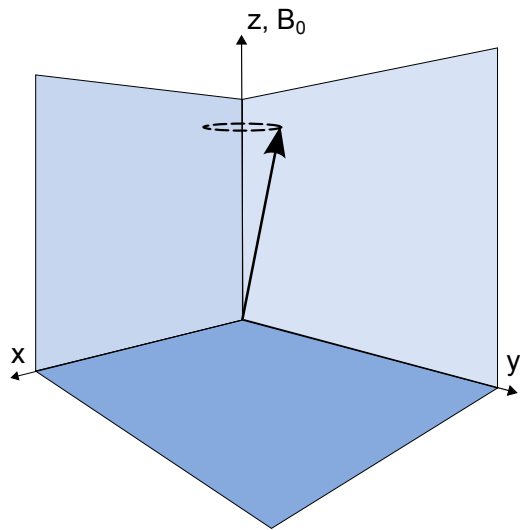


Fig. 1.6: Larmor precession of the magnetic moment vector about an external, static magnetic field  $\mathbf{B}_0$ , conventionally assigned in the direction of the z-axis.

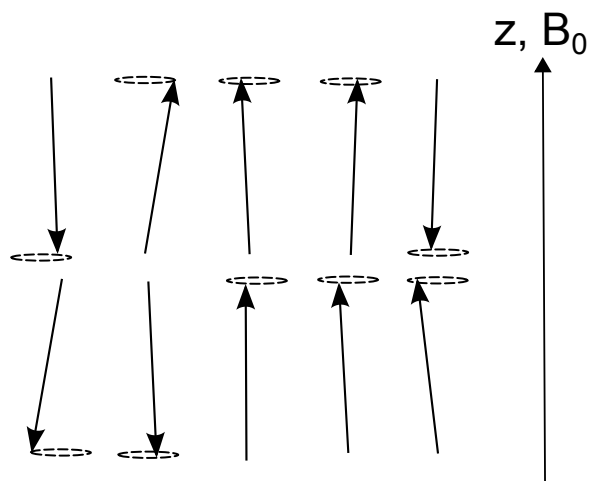


Fig. 1.7: Spin populations aligned with and against the external magnetic field  $\mathbf{B}_0$ .

field describes one of two possible energy states (figure 1.7). The population of each energy state is given by the Boltzmann distribution:

$$\frac{N_-}{N_+} = e^{\frac{-E}{kT_K}} \quad (1.1)$$

where  $N_-$  describes the upper energy state,  $N_+$  the lower energy state,  $E$  the energy difference between the spin states,  $k$  is Boltzmann's constant and  $T$  is the temperature in Kelvins. The energy difference between the two spin states depends on the nuclei of interest via its gyromagnetic ratio, and the external magnetic field:

$$E = h\gamma B_0 \quad (1.2)$$

where  $h$  represents Planck's constant,  $\gamma$  the gyromagnetic ratio (42.58 MHz/T for hydrogen) and  $B_0$  is the field strength of the MRI scanner, typically ranging from 1.5 to 9.4 T in modern clinical and research systems.

The populations of spins in either energy state in the external magnetic field reaches an equilibrium equilibrium state after a short interval (typically a few seconds for tissues) and remains in equilibrium if the field is held constant, as is the case with the main magnetic field within an MRI scanner. The energy difference between the two states corresponds to electromagnetic radiation in the radio-frequency (RF) range and thus, the population ratio of the two states can be perturbed with an RF excitation pulse of the appropriate frequency, given by  $\omega_0$  and called the Larmor frequency:

$$\omega_0 = \gamma B_0 \quad (1.3)$$

Following this excitation, the spins progressively return to their equilibrium populations. However, it is unnecessary to continue tracking spins in terms of their energy state populations. An appropriate and useful simplification is to consider the aggre-

gate magnetization, over a macroscopic scale, of a group of spins experiencing the same electromagnetic effects and therefore having the same precession frequency (figure 1.8).

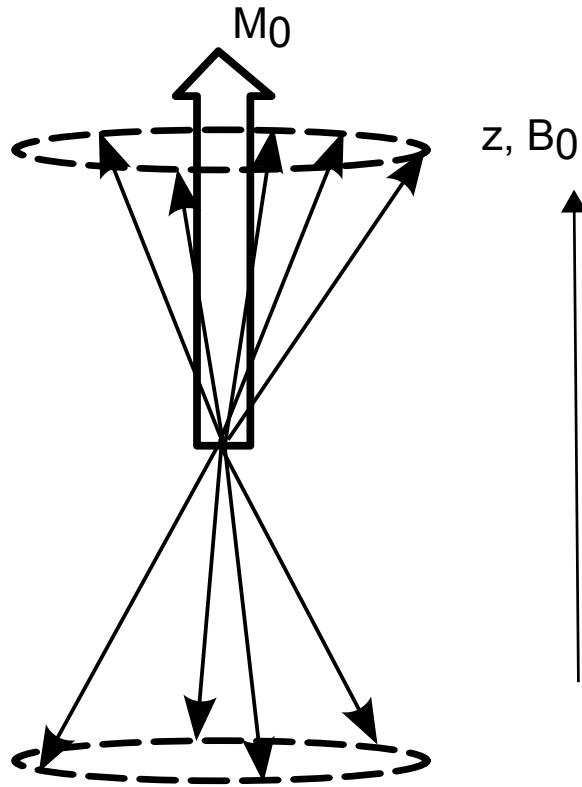


Fig. 1.8: The magnetization isochromat as the net magnetization vector of a spin population.

As such, we can depict a magnetization isochromat in an external field  $\mathbf{B}_0$  as a macroscopic magnetization vector at an equilibrium  $M_0$  until disturbed by the magnetic field of a RF excitation pulse  $B_1$  on resonance at the Larmor frequency. Though Larmor precession is still taking place, the random phase of each spin results in the macroscopic magnetization vector being perfectly aligned with the external magnetic field (figure 1.9a). In a three dimensional plane, the direction of  $\mathbf{B}_0$  is conventionally assigned to the  $z$ , or longitudinal, axis.  $B_1$  is typically applied perpendicular to the  $z$  axis and varies with  $\omega_0$ . In those conditions, the effective field experienced by  $M_0$

will cause nutation towards the x-y, or transverse, plane (figure 1.9b).  $B_1$  is usually prescribed in terms of the flip angle  $\Theta$ , which depends both on the power and duration of the RF pulse.

Following excitation, all the spins are now in phase and still subject to a static external field. The macroscopic magnetization precesses about the z axis, inducing an electromotive force (EMF) in any nearby conductor (figure 1.10). The EMF is only induced by the component of the magnetization vector in the transverse plane,  $M_{xy}$ , and is responsible for any recorded signal in an MRI experiment. Carefully designed coils are used in MRI to detect this signal and are optimized for different parts of the human anatomy. The macroscopic magnetization returns towards its equilibrium state via relaxation processes which are dependent on properties of the sample being imaged.

### 1.4.2 The Bloch Equations

The Bloch equations serve as a phenomenological description of the evolution in time of the magnetization vector [58] and introduce two time constants, T1 and T2, which describe the characteristic rates of the two distinct relaxation processes:

$$\frac{d}{dt}M(t) = \gamma[\vec{M}(t) \times \vec{B}] - \frac{M_x(t)}{T_2}\hat{x} - \frac{M_y(t)}{T_2}\hat{y} + \frac{M_0 - M_z(t)}{T_1}\hat{z} \quad (1.4)$$

where T1 is called the longitudinal (or spin-lattice) relaxation time and T2 the transverse or (spin-spin) relaxation time. We can separate the component of the magneti-

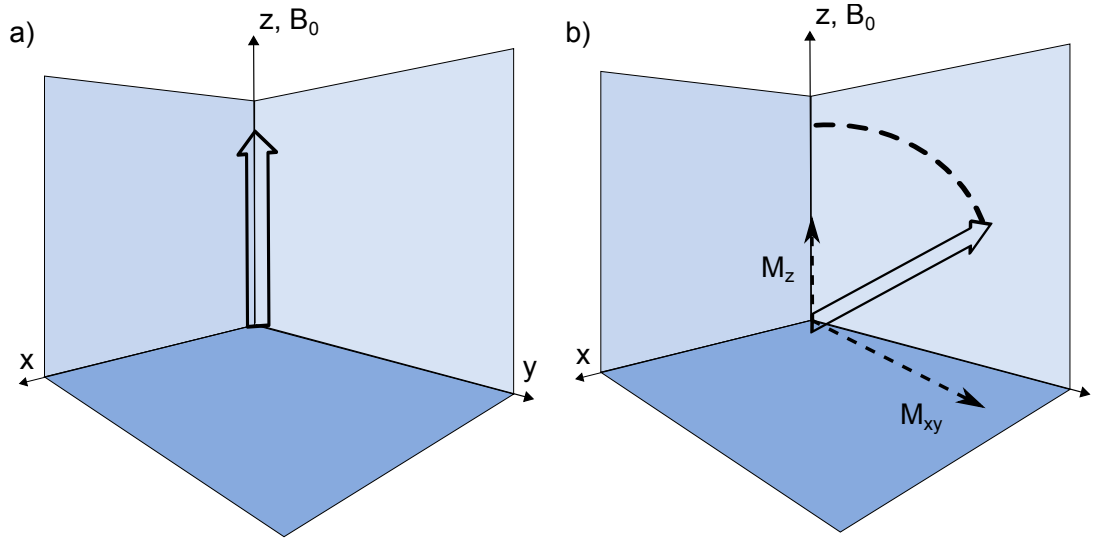


Fig. 1.9: Excitation of the macroscopic magnetization. (a) The magnetization is initially in an equilibrium position aligned with the external magnetic field represented by the equilibrium magnetization vector  $\vec{M}_0$  (b) An RF pulse applied along x nutates  $\vec{M}_0$  away from the z-axis and towards the x-y plane resulting in a magnetization vector  $\vec{M}$  with transverse component  $M_{xy}$ .

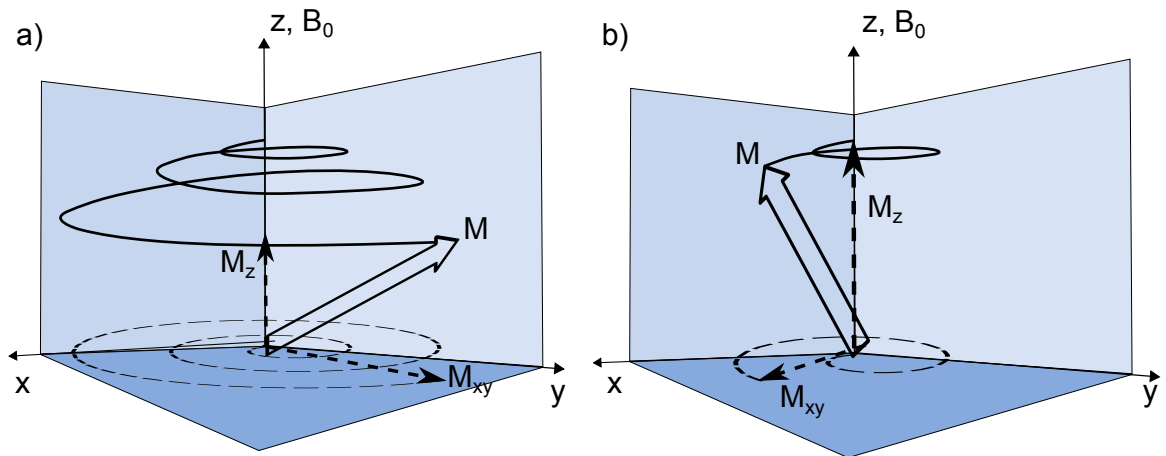


Fig. 1.10: Relaxation of the macroscopic magnetization. (a) The component of  $\vec{M}$  in the transverse plane,  $M_{xy}$ , is responsible for all recorded signal in a MRI experiment. (b) The magnetization returns to its equilibrium condition  $M_0$  until another RF excitation pulse.

zation vector in each direction:

$$\frac{d}{dt}M_x(t) = \gamma M_y B_0 - \frac{M_x}{T_2} \quad (1.5)$$

$$\frac{d}{dt}M_y(t) = \gamma M_x B_0 - \frac{M_y}{T_2} \quad (1.6)$$

$$\frac{d}{dt}M_z(t) = -\frac{M_z - M_0}{T_1} \quad (1.7)$$

The solution to these differential equations is as follows:

$$M_x(t) = [M_x(0) \cos(\omega_0 t) - M_y(0) \sin(\omega_0 t)] \cdot e^{-\frac{t}{T_2}} \quad (1.8)$$

$$M_y(t) = [M_x(0) \sin(\omega_0 t) + M_y(0) \cos(\omega_0 t)] \cdot e^{-\frac{t}{T_2}} \quad (1.9)$$

$$M_z(t) = M_0 + [M_z(0) - M_0] \cdot e^{-\frac{t}{T_1}} \quad (1.10)$$

By defining the total magnetization in the transverse plane as  $M_{xy} = M_x + iM_y$ , a formalism appropriate given the usual quadrature detection [59] of the EMF, and the longitudinal magnetization as  $M_z$ , we obtain the relationships describing T1 recovery and T2 decay, assuming all of the initial equilibrium macroscopic magnetization was nutated into the transverse plane:

$$M_{xy}(t) = M_0 e^{-\frac{t}{T_2}} e^{i\omega_0 t} \quad (1.11)$$

$$M_z(t) = M_0 (1 - e^{-\frac{t}{T_1}}) \quad (1.12)$$

Demodulation of the EMF is typically performed before the data is recorded which removes the Larmor frequency component from equation 1.11. This yields a recorded signal intensity  $s(t)$  in the magnetization isochromat's rotating frame of reference dependent on T2:

$$s(t) \propto M_0 e^{-\frac{t}{T_2}} \quad (1.13)$$

T2, the decay constant of this signal, is of primary interest in this thesis. Specifically, its significance in the study of the properties brain tissue will be the focus of the following chapters.

### 1.4.3 Imaging gradients

Obtaining an image of the sample requires additional manipulation of its magnetization. Three gradient coils, one for each orthogonal direction, are used to achieve this. The details of how the signal localization is implemented are different in each imaging direction. However, each approach makes use of the MRI system's gradient coils to induce phase and/or frequency shifts of the precessing magnetization with a known spatial dependence to encode the positional information into the recorded signal.

In two-dimensional (2D) imaging, slice selection is achieved by using an excitation RF pulse of known bandwidth in tandem with an applied gradient in the slice select direction conventionally assigned to the  $z$  direction. Recalling the dependence of the Larmor frequency on the externally applied field, the Larmor frequency now becomes spatially dependent according to:

$$\omega(z) = \gamma(B_0 + G_{ss}z) \quad (1.14)$$

where  $G_{ss}$  is the applied slice selection gradient. Figure 1.11 depicts the relationship between slice selection and RF pulse bandwidth. However, as explained by Fourier theory, a truly rectangular slice profile is not possible as the Fourier relationship between the time and frequency domains require an RF pulse of infinite length. Imperfect slice profiles can lead to mis-registered signal and cross-talk, effects which can be mitigated through pulse sequence design.

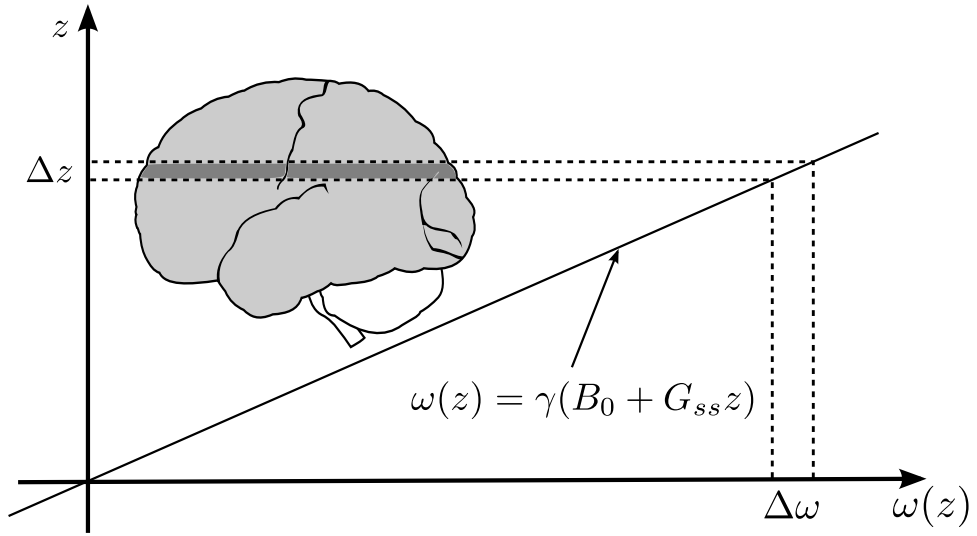


Fig. 1.11: The relationship between RF pulse bandwidth, slice selection gradient and slice excitation of the sample

Within the in-slice imaging plane, the remaining two dimensions are assigned to a phase encoding direction and a frequency readout direction. The k-space formalism describes the frequency and phase encoded data and relates it to the final image with the Fourier relationship:

$$S(k_x, k_y) = \int_x \int_y M(x, y) e^{ixk_x} e^{iyk_y} dy dx \quad (1.15)$$

where  $S(k_x, k_y)$  is k-space data and  $M(x, y)$  is the magnetization of the sample in image space. K-space is traversed using the following relation:

$$k_x = \gamma \int_0^t G_x(t) dt \quad (1.16)$$

$$k_y = \gamma \int_0^t G_y(t) dt \quad (1.17)$$

where  $G_x(t)$  and  $G_y(t)$  describe the gradient waveforms.

Frequency readout is conventionally assigned to the x-direction and is achieved by



collecting an entire line of k-space data with the system's digital receiver or analog-to-digital converter (ADC) in the presence of the readout gradient  $G_{ro}$ . Before signal sampling begins, a gradient of opposing polarity and half the area is used along the readout direction to purposely pre-wind the magnetization, corresponding to a displacement to the left-most edge of k-space. The readout gradient then rewinds the magnetization during signal collection such that complete rephasing, called the gradient echo, occurs at the centre of the ADC acquisition window. This corresponds to a traversal of k-space from the left-most edge to the right-most edge.

The sampling rate of the ADC is associated with receiver bandwidth ( $rBW$ ) during signal readout, usually expressed as the total receiver bandwidth (in Hz) or as the frequency per imaging pixel (Hz/px). The receiver bandwidth influences the signal-to-noise ratio (SNR) of the collected signal. A wider bandwidth will include more noise as noise is uniformly distributed in frequency (equation 1.18). However, a higher bandwidth also implies a faster gradient readout and faster imaging.

$$SNR \propto \frac{1}{\sqrt{rBW}} \quad (1.18)$$

Phase encoding is achieved by incrementally altering the  $k_y$  position before each readout with a brief y-gradient pulse,  $G_{pe}$ . A simple pulse sequence diagram is shown in figure 1.12 presenting slice selection, phase encoding and the readout gradients used to collect a gradient echo. The brief phase encoding gradient pulses are represented by the phase encoding table, where traversal in the  $k_y$  direction is achieved by sequentially repeating this cycle for a predefined number of phase encoding steps, separated by a repetition time (TR). All these elements constitute a simple, but complete, gradient echo imaging experiment (figure 1.12). In this way, a complete k-space dataset is obtained, from which the image data can be reconstructed via a two-dimensional inverse Fourier transformation (figure 1.13).

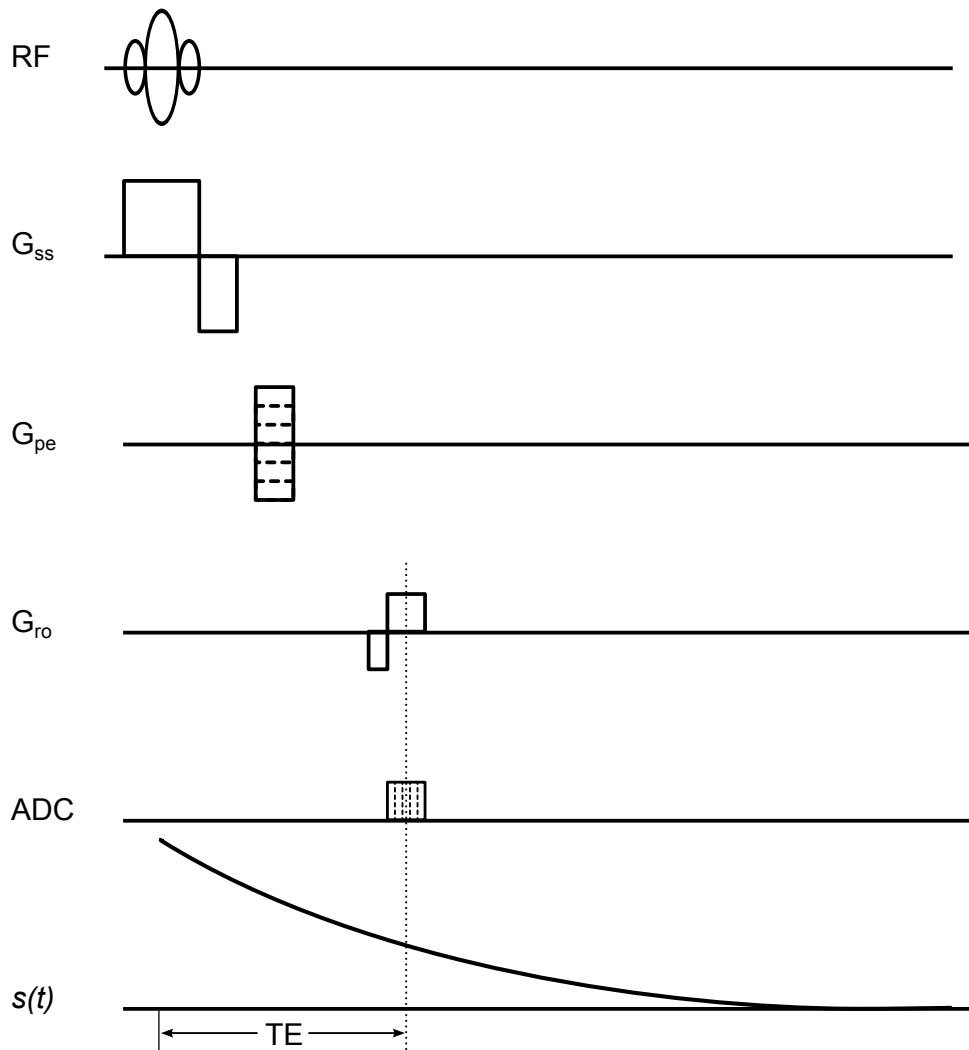


Fig. 1.12: A gradient echo pulse sequence diagram with all elements needed for a complete imaging experiment. The RF pulse nutates the equilibrium magnetization into the transverse plane, while  $G_{ss}$ ,  $G_{pe}$  and  $G_{ro}$  are gradient waveforms achieving slice selection, phase encoding and frequency readout respectively. These imaging gradients are a source of signal loss and recovery, which are omitted for clarity in this and subsequent pulse sequence diagrams. The signal is collected with the ADC, effectively sampling the signal decay at time  $TE$ .

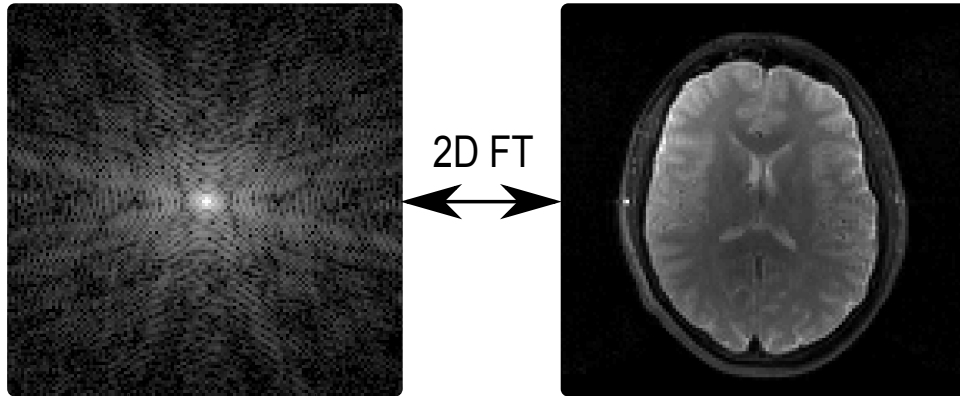


Fig. 1.13: K-space data (left) and the corresponding reconstructed brain image (right) are linked by a two-dimensional Fourier transform.

#### 1.4.4 Transverse relaxation *in vivo*

The net transverse magnetization is possible due to the phase coherence of the individual spins making up the macroscopic magnetization, following the excitation by the  $B_1$  field. The progressive loss of this phase coherence is described by the Bloembergen-Purcell-Pound (BPP) theory of relaxation [60] which formulates the decay rate as follows and introduces the correlation time  $\tau_c$ :

$$\frac{1}{T_2} = \frac{K}{2} \left[ 3\tau_c + \frac{5\tau_c}{1 + \omega_0^2\tau_c^2} + \frac{2\tau_c}{1 + 4\omega_0^2\tau_c^2} \right] \quad (1.19)$$

where  $K$  is a proportionality constant composed of nuclear parameters, the gyromagnetic ratio and the inter-nuclear distance of the spins.  $T_2$  depends on the resonant frequency experienced by the spin,  $\omega_0$ , and the correlation time,  $\tau_c$ .

In complex biological systems, many factors interplay to affect the phase coherence of the transverse magnetization. The BPP theory generally proves inadequate to predict the measured relaxation times of complex samples such as brain tissue. Nevertheless, the correlation time describes the time scale of molecular motion and affects the relaxation rate by way of magnetic interactions between neighbouring protons,

where greater mobility results in greater motional averaging of interacting field and a longer relaxation time. In this way, T2 depends on the local cellular structure and environment, rendering it very sensitive to changes in the neurobiology of brain tissue.

The presence of static sources of magnetic field perturbations will contribute to additional transverse magnetization dephasing across an imaging volume element (or voxel), resulting in an effective transverse relaxation time T2\*:

$$\frac{1}{T2^*} = \frac{1}{T2} + \frac{1}{T2'} \quad (1.20)$$

Here, T2' is the reversible transverse relaxation time describing the additional phase dispersion which can be recovered when the source of the disturbance is static. Such sources include susceptibility induced inhomogeneities caused by tissue boundaries and thus vary throughout the brain. As such, T2\* shortening due to T2' effects has important implications with respect to quantitative T2 measurements.

### 1.4.5 Quantitative T2

The spin echo is a basic approach to recover signal losses due to static sources of dephasing. A spin echo pulse sequence is similar to the gradient echo pulse sequence but with an additional 180 degree RF pulse applied at time  $\frac{TE}{2}$  following the initial excitation pulse, which effectively flips all magnetization about an axis in the transverse plane to create the spin echo at time TE. The pulse sequence diagram of a basic spin echo experiment and the time evolution of the recorded transverse magnetization are shown in figure 1.14. TR is another important pulse sequence parameter. Since the magnetization present in the transverse plane after an excitation pulse depends on the longitudinal magnetization present immediately before the pulse, a suitably long TR is used as a time delay to allow the longitudinal magnetization's return to equilibrium and avoid the introduction of T1-weighting to the measurement. Repeated

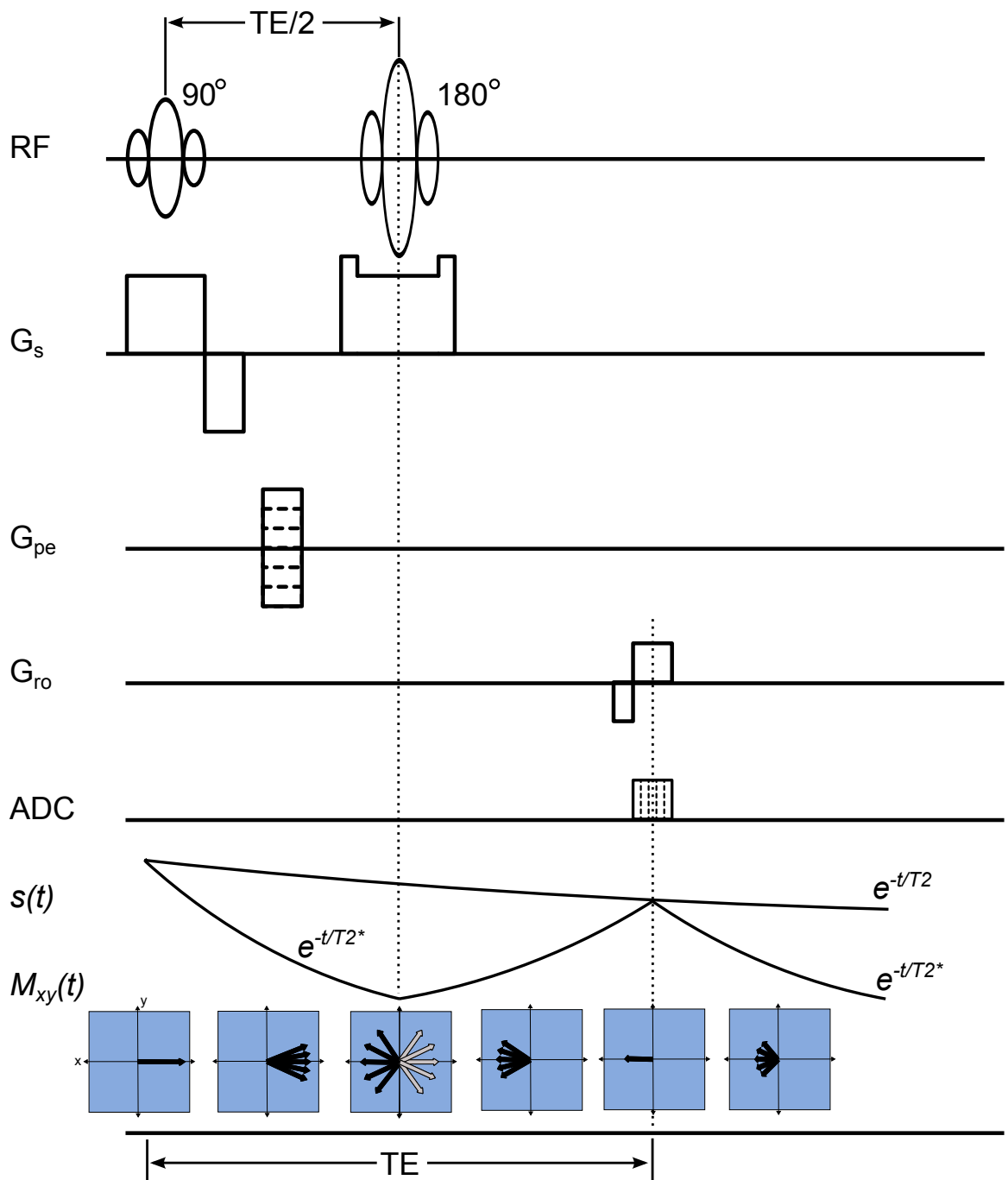


Fig. 1.14: Pulse sequence diagram of a spin echo experiment and the respective vector representation of the time evolution of a voxel's transverse magnetization (bottom). A  $90^\circ$  degree excitation pulse nutates the magnetization in the transverse plane, which begins dephasing until a  $180^\circ$  degree re-focussing pulse inverts the magnetization at time  $TE/2$ . Once the magnetization is inverted, the effect of the static magnetic field inhomogeneities is reversed which leads to the spin echo at time  $TE$ .

measurements obtained over a range of TE values allow the calculation of T2 on a voxel-by-voxel basis, or in regions-of-interest (ROIs).

#### **1.4.6 Summary**

The utility of T2 measurements in the human brain resides in the sensitivity of T2 to interactions of water with cell structures. T2 mapping affords an opportunity to investigate the effect of psychiatric disorders on neurodevelopment and test hypotheses for a neurobiological basis. The work contained in the remainder of this thesis first assesses T2 abnormalities in autism and TS syndrome and then pursues novel methodology to obtain more specificity from transverse relaxation data.

## Chapter 2

# Investigating T2 in autism and Tourette Syndrome

## 2.1 T2 abnormalities of white matter in autism

### 2.1.1 Introduction

The tissue abnormalities underlying the reported increased brain volumes in autism are unclear. Image-based T2 measurements provide an opportunity for the *in vivo* investigation of tissue abnormalities. It was noted in chapter 1 that detection of the MRI signal is enabled by the phase coherence of the intra-voxel transverse magnetization present after excitation and is subject to both reversible and irreversible dephasing (T2 and T2'). The combination of both dephasing regimes gives rise to an effective relaxation time (T2\*). T2 is influenced by tissue water and cellular structure. T2', on the other hand, is more sensitive to static magnetic field inhomogeneities and thus may provide a specific measure of brain iron stores [61, 62]. Studies have reported T2 differences in other neuropsychiatric conditions, including multiple sclerosis (MS) [63], temporal lobe epilepsy [64], and schizophrenia [65]

Despite the potential utility of T2 imaging in furthering our understanding of the pathophysiology of autism, only three previous studies have reported on T2 measurements in autism. The first study investigating T2 in autism assessed the T2 values of the amygdala and hippocampus using a single slice through these regions [66]. No significant differences were found between patients with autism and controls. The second study from our group and based on a sample overlapping with the data presented in this chapter [67], was the first to examine whole brain T2 in autism and noted a significant increase in global white matter T2 (but not global grey matter T2) among boys with autism. Additionally, regional differences were investigated using voxel-based relaxometry and regions of increased T2 were found bilaterally in the grey matter and white matter of the parietal and occipital lobes and in the frontal white matter. A third study [68] found elevated T2 in the cortical grey matter of young children with autism. However, differences in patient cohort selection criteria and T2 quantification methodologies prevent us from making any direct comparisons between this last study and earlier studies.

The aforementioned previous study from our group was the first to perform a whole cerebrum assessment of T2 [67]. However, the nature of its voxel-based analysis calls for a cautious interpretation since voxel-based assessments have been shown to sometimes yield different results than ROI-based analyses of the same datasets [69, 70]. The result of increased global white matter T2 motivated further assessment of T2 abnormalities within this patient sample, presented in this chapter. The concurrent absence of total grey matter T2 differences alongside elevated total white matter T2 lends evidence for tissue abnormalities of white matter which generally corroborates volumetric abnormalities reported in autism.

No previous study has assessed regional differences of T2 of the entire cerebrum in autism using ROI analyses. To further investigate correspondence of T2 abnormal-



ities with volume abnormalities reported in the literature, two parcellation schemes were devised. The first divides cerebral white matter into standard anatomical lobes: frontal, parietal, temporal and occipital. The second invokes the scheme used by Herbert et al, [71] where three neurodevelopmentally relevant white matter compartments are described. These are comprised of radiate, bridging and sagittal white matter compartments. The objective of this study was to investigate the differential contributions of white matter based on these two parcellation schemes.

Based upon previous findings of volumetric, DTI and MRS abnormalities in the frontal lobes of children with autism [17,72,73], we hypothesized that the increase in white matter T2 among patients with autism would be localized to the frontal lobes in the lobar analysis. In the compartmental analysis, we hypothesized, based on the findings of Herbert and colleagues [71], that the late-myelinating radiate white matter would be the only compartment with increased T2.

## **2.1.2 Methods**

### **2.1.2.1 Subjects**

As the present study is a follow-up study to Hendry et al. [67], subject selection, recruitment and imaging had already been conducted. However the relevant methodology is included here for completeness. All calculations and analyses following the data acquisition were conducted independently of the previous study.

Twenty-seven males with autism between the ages of 6 years and 16 years participated in this study. The diagnosis of autistic disorder was made using the Autism Diagnostic Interview-Revised (ADI-R) [72], the Autism Diagnostic Observation Schedule (ADOS-R) [73] and clinical observation. All patients met the Diagnostic and Sta-

tistical Manual of Mental Disorders-Text Revision (DSM-IV-TR) criteria for autism [2] as well as ADI-R and ADOS algorithm criteria. Handedness was determined through clinical observation and the report of the patients and their parents. Patients were also assessed using the Wechsler Intelligence Scale for Children, 3rd Edition (WISC-III) or the Leiter International Performance Scale, depending upon their verbal ability (i.e., subjects whose limited verbal abilities precluded the use of the WISC-III were tested using the Leiter, a non-verbal test of intelligence). Patients with a non-verbal IQ below 70 were excluded from participation. All patients had a physical examination prior to participation in this study, and subjects with a seizure disorder, other neurological condition, a cytogenetic abnormality, or genetic syndrome (such as Fragile X syndrome) were also excluded from participation. At the time of the scan, 10 patients were medication naive, while three others had discontinued their previous medications at least a month prior to the scan. Among the remainder, three were being treated with dopamine antagonists, four were taking stimulants, and two were receiving serotonin re-uptake inhibitors. In order to complete their MRI scans, 15 patients required oral sedation with midazolam.

Twenty-five males between the ages of 6 years and 16 years, drawn from the local community through advertisement and word of mouth, participated as control subjects in this study. They were assessed with the Schedule for Affective Disorders and Schizophrenia-Childhood Version [74] in order to ensure that none had a major psychiatric disorder. Additionally, none had a personal history of neurological disorders or a family history of autism or mental retardation. Controls were also assessed with the WISC-III or the Wechsler Abbreviated Scale of Intelligence, and a full-scale IQ of less than 70 was exclusionary. No control subjects received medication in order to complete their MRI scan.

The Health Sciences Research Ethics Board at The University of Western Ontario

approved this study. The parents of all subjects provided written consent for participation in this study, while the subjects provided written assent.

### **2.1.2.2 MRI acquisition**

All subject scans were obtained using a 3T head-only MRI scanner (IMRIS, Winnipeg, Canada) with a quadrature birdcage head coil. A Gradient Echo Sampling of the Free Induction Decay and Echo (GESFIDE) sequence [75] was used for the data acquisition. This sequence is an extension of the spin echo technique presented in chapter 1 with additional gradient echo sampling of the initial free induction decay after the excitation of a 90 degree RF pulse and the recovery towards a spin echo after a 180 degree refocussing pulse (see figure 2.1). The sequence parameters were: repetition time = 2800 ms; matrix size = 192 x 256; field of view = 220 mm; slice thickness = 4 mm<sup>2</sup> with 1.5 mm gap; 22 slices; resolution = 1.15 mm x 0.86 mm x 4 mm; total scan time = 9 min. In this acquisition five gradient echo images with a first echo time of 9 ms and an inter-echo spacing of 8.7 ms were acquired prior to the refocusing pulse, while six gradient echo images separated by 8.78 ms followed, after the spin echo. The spin echo was formed at an echo time of 102 ms.

### **2.1.2.3 Image reconstruction and registration**

The image data acquired with the GESFIDE sequence lend themselves to calculations using the relaxation rates rather than relaxation times. Thus, R2 maps were created, where  $R2 = 1/T2$  and  $R2' = 1/T2'$ . A voxel-by-voxel natural mono-exponential logarithmic fit of the signal decay versus echo time during the first five gradient echoes measures  $R2^*$ , where  $R2^* = R2 + R2'$ . Similarly, a natural logarithmic fit of the last six echoes gives  $R2^-$ , where  $R2^- = R2 - R2'$ . These values were then combined, on a voxel-by-voxel basis, to calculate R2 and R2'. A power image noise correction was used in the fitting algorithm to avoid non-linear contributions from zero-mean

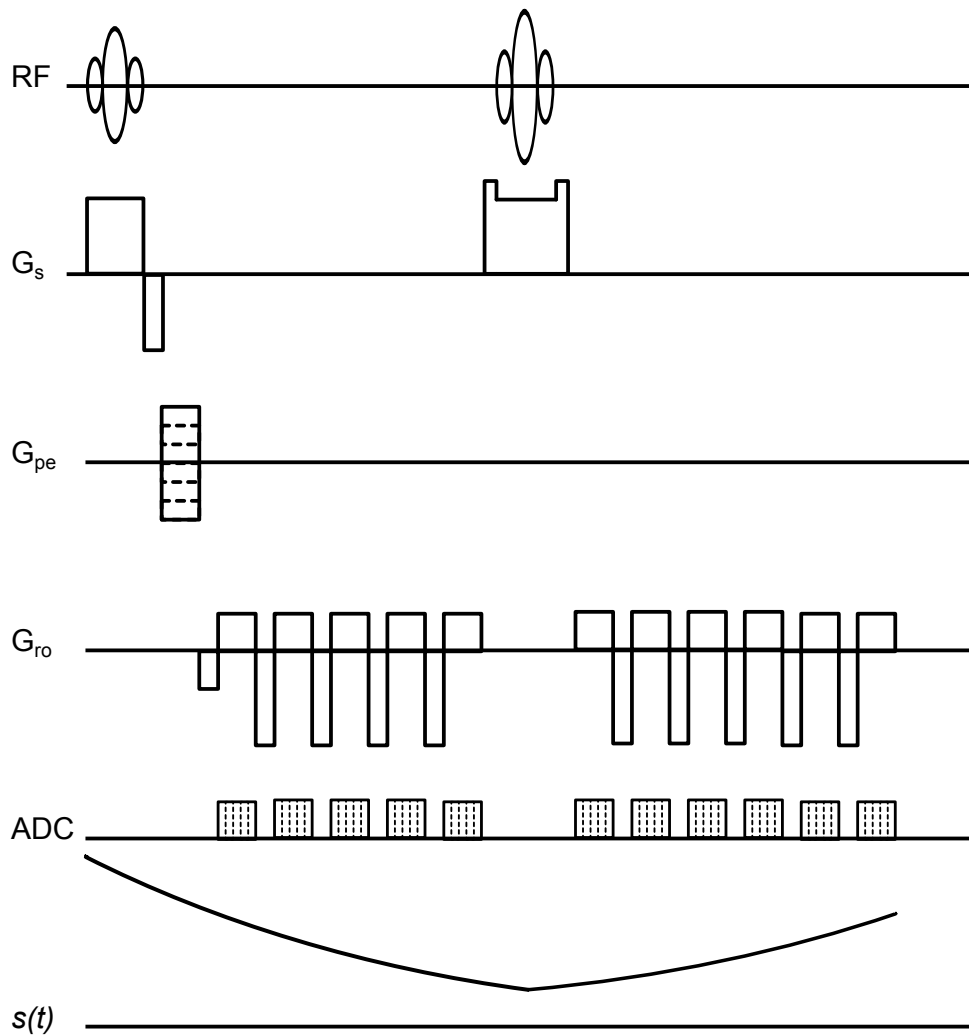


Fig. 2.1: GESFIDE pulse sequence diagram. Gradient echoes sample the signal on both side of the 180 degree RF pulse, before the spin echo, allowing the calculation of  $T_2$ ,  $T_2^*$  and  $T_2'$ .

noise [76] and is described in detail in appendix I.

To allow for inter-subject comparisons, image registration was performed to normalize all R2 maps to a standard stereotactic space, which approximates Talairach space. A T2-weighted template (ICBM-152, Montreal Neurological Institute) was used in conjunction with each subject's T2-weighted image (obtained from the last echo of the GESFIDE acquisition) in the image registration routine offered in SPM2 (Wellcome Trust Centre for Neuroimaging; University College London, London, United Kingdom). A 12-parameter affine transformation was first estimated within a Bayesian framework to account for global differences such as rotation, translation and scaling [77]. This was followed by a non-linear global transformation that accounts for low spatial frequency shape differences, modelled by a linear combination of smooth spatial basis functions [78]. A set of parameters describing these transformation into stereotactic space was then applied to the R2 map in order to register it to standard space. A flowchart representing the steps involved in the image reconstruction and registration is shown in figure 2.2.

#### **2.1.2.4 Mean lobar T2 calculations**

Masks for each ROI (frontal, temporal, parietal and occipital lobes) were created using the PickAtlas toolbox for Matlab (Wake Forest University) [79]. These masks are three-dimensional binary volumes representing the location of each ROI in standard space. White matter probability maps were constructed for each subject using the routine offered in SPM2 and were converted to binary masks using a threshold value of 0.90, as we had done in a previous study [67]. We then obtained mean R2 and R2' measurements for each ROI by first multiplying the R2 maps with the binary, subject-specific, white matter mask and then multiplying the result with the region-specific ROI masks and taking the mean of the remaining non-zero voxels. Lobar

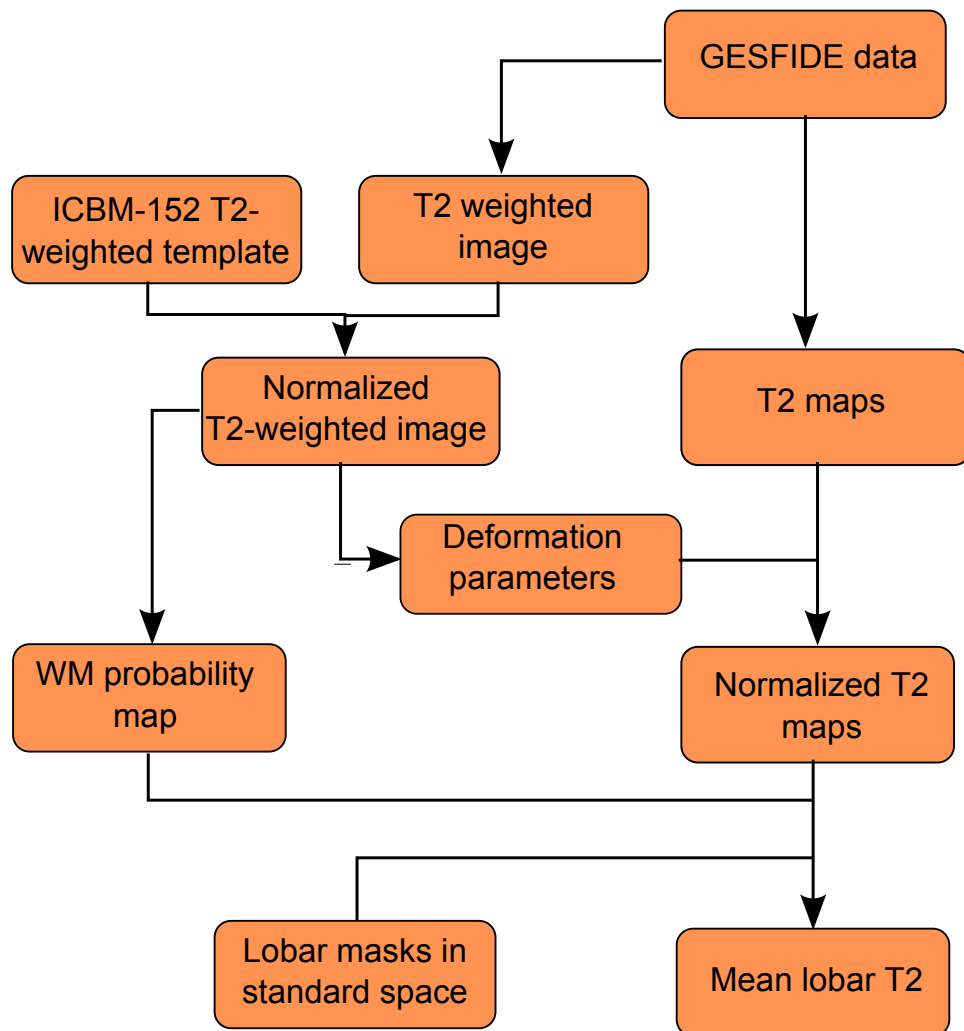


Fig. 2.2: Flowchart outlining the steps involved in the image reconstruction from the GESFIDE data, the spatial normalization into standard space and the calculation of the mean white matter (WM) T2 of each lobar ROI.

ROIs and white matter probability maps in standard space are shown in figure 2.3. T2 relaxation times used for statistical analyses were obtained by taking the reciprocals of the relaxation rate,  $1/R2$ .

#### **2.1.2.5 Mean compartmental T2 calculations**

The study-specific white matter compartment map was created in two steps. Definitions of radiate, sagittal and bridging white matter vary somewhat in the literature but were chosen to mirror those of Herbert et al. [71,80]. The ICBM-DTI-81 [81] was used and white matter structures were assigned into their respective bridging, sagittal and radiate compartments. The ICBM-DTI-81, however, does not include subcortical white matter or any white matter above the corona radiata. To include this superficial white matter into the radiate white matter compartment, a mask of the cerebrum including all lobes was generated using PickAtlas (Wake Forest University) [79] and its complement relative to the sagittal and bridging white matter compartments was added to the radiate compartment. Identically to the previous section, white matter probability masks for each subject were intersected with the compartmental ROI masks to then calculate mean relaxation times (figure 2.4). Bridging, sagittal and radiate ROIs are shown in figure 2.5.

#### **2.1.2.6 Statistical analysis**

Age, race, handedness, height, and IQ were compared using t-tests or chi-square analyses.

Separate analyses were conducted for statistical analysis of group differences with each parcellation scheme, one for the regional assessment of mean T2 by lobe and a second for the mean T2 by white matter compartment. In each case, group differences in regional white matter T2 were investigated in separate Repeated-Measures

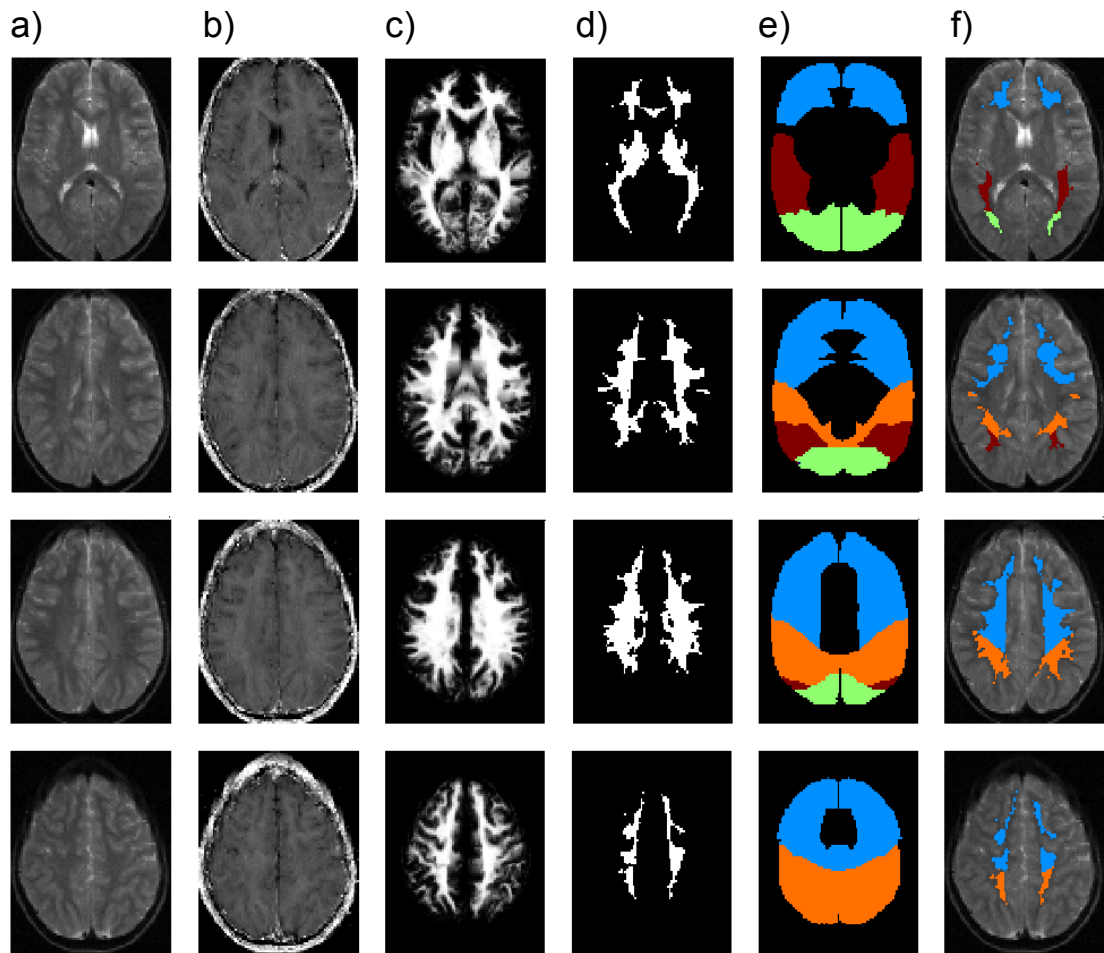


Fig. 2.3: a) T2-weighted images, b) R2 maps, c) white matter probability maps, d) white matter mask, e) Lobar ROIs f) white matter mask intersected with lobar ROIs overlaid onto T2-weighted image.



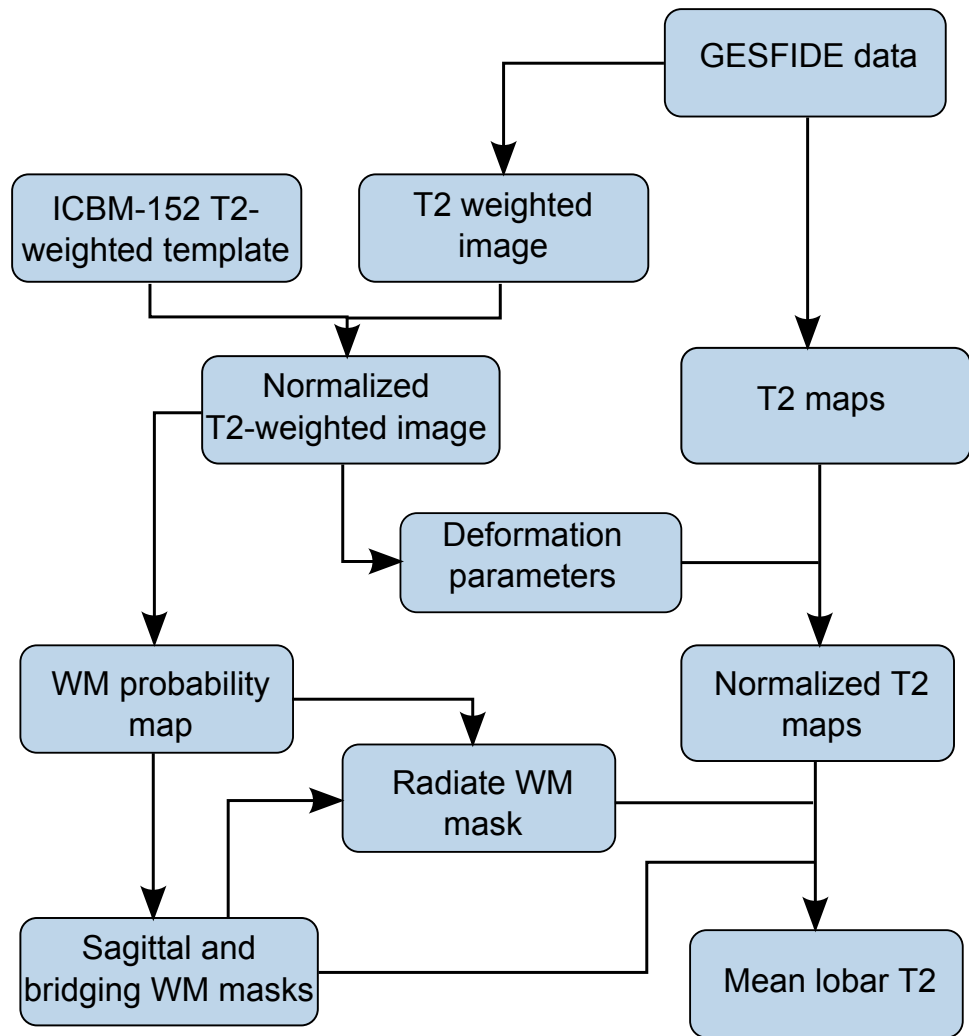


Fig. 2.4: Flowchart outlining the steps involved in the image reconstruction from the GESFIDE data, the spatial normalization into standard space and the calculation of the mean white matter (WM) T2 of each white matter compartment.

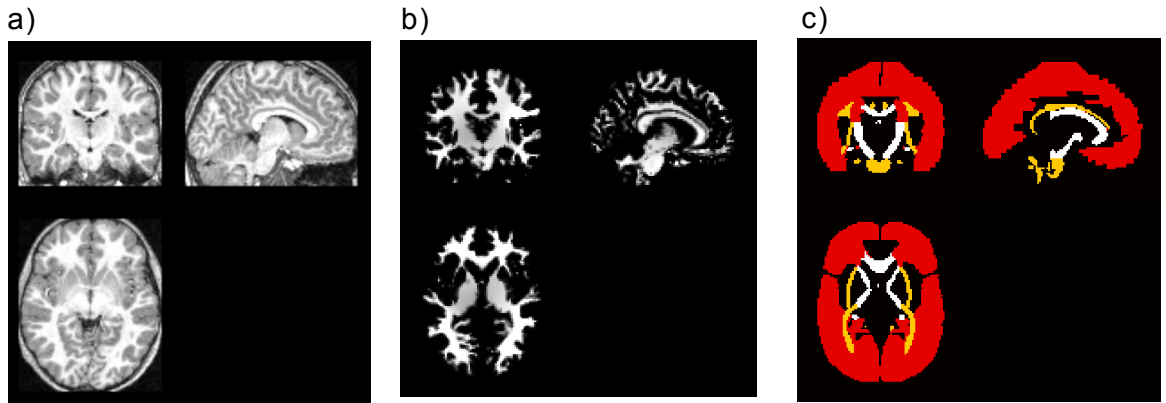


Fig. 2.5: Coronal, sagittal and axial views of a) T1-weighted anatomical image, b) white matter probability map c) compartmental ROIs before intersection with white matter probability mask. Radiate white matter is in red, bridging in white and sagittal in yellow.

Analyses of Covariance (ANCOVA). In each analyses, T2 was the dependent variable, diagnosis (autism or control) was the between-subjects factor, and ROI and side (left and right) were the within-subjects factors. Significant main effects of diagnosis or higher order interactions involving diagnosis ( $p < 0.05$ ), were examined for each region and side individually with exploratory *post-hoc* ANCOVAs to identify the region(s) that contributed to the significant main effect or interaction. Although age did not differ significantly between the groups, the age range in this study was wide. Given the changes in T2 described in childhood [82], we covaried the statistical analysis of T2 for age to reduce error variance and increase statistical power.

### 2.1.3 Results

Data from 6 patients with autism and 5 control subjects were excluded from analyses due to excessive motion. Among the remaining subjects, there were no significant differences between groups in terms of age, race, height, non-verbal IQ, or full-scale IQ. Patients with autism did have a significantly lower verbal IQ (Table 2.1). Con-

sistent with the results of other studies, there was a significantly greater proportion of left-handed subjects in the patient group [83].

|                  | Patients (n=21) | Controls (n=20) | Statistic    | p     |
|------------------|-----------------|-----------------|--------------|-------|
| Age (yr)         | 9.4             | 10.8            | t = 1.6      | 0.1   |
| Height (cm)      | 142.0           | 148.7           | t = 1.1      | 0.3   |
| Weight (kg)      | 39.9            | 39.1            | t = 0.2      | 0.9   |
| Head circ. (cm)  | 54.7            | 54.8            | t = 0.1      | 0.9   |
| Handedness (R/L) | 14/7            | 20/0            | $\chi^2=9.1$ | 0.003 |
| Verbal IQ        | 93.8            | 104.8           | t = 1.6      | 0.02  |
| Non-verbal IQ    | 106.7           | 103.0           | t = 1.6      | 0.4   |
| Full scale IQ    | 99.5            | 104.4           | t = 1.6      | 0.3   |

Table 2.1: Subject demographics

### 2.1.3.1 Lobar

Repeated measures ANCOVA of T2 data revealed a significant main effect of diagnosis ( $F(1,38)=5.9$ ,  $p=0.02$ ) and a significant group-by-side interaction ( $F(1,38)=4.4$ ,  $p=0.04$ ). There were no other significant interactions involving diagnosis. *Post-hoc* analyses revealed that patients had an overall increase in white matter T2 using age as a covariate ( $F(1,38)=5.9$ ,  $p=0.02$ ; Cohen’s  $d=0.79$ ). Patients also had a significant increase in white matter T2 in the right hemisphere ( $F(1,38)=9.2$ ,  $p=0.004$ ) using age as a covariate. Group differences in left hemisphere white matter T2 did not reach significance.

As there were no significant diagnosis by region by side interactions, indicating that there were no other significant asymmetries of T2, left and right hemisphere data were pooled for further analyses. *Post-hoc* analysis revealed that patients had a significant increase in frontal ( $F(1,38)=5.3$ ,  $p=0.03$ ; Cohen’s  $d=0.8$ ) and parietal white matter T2 ( $F(1,38)=5.8$ ,  $p=0.02$ ; Cohen’s  $d=0.9$ ) (see Table 2.2). There were

| Lobe      | Patients (n= 21) |          | Controls (n= 20) |          | ANCOVA |      |
|-----------|------------------|----------|------------------|----------|--------|------|
|           | left             | right    | left             | right    | F      | p    |
| Frontal   | 65.0±2.4         | 67.8±2.2 | 63.5±2.5         | 65.6±2.4 | 5.3    | 0.03 |
| Occipital | 66.9±2.6         | 68.2±2.8 | 65.4±2.4         | 66.9±2.9 | 2.3    | 0.1  |
| Parietal  | 67.1±2.7         | 69.9±3.0 | 66.2±2.5         | 63.4±2.8 | 5.8    | 0.02 |
| Temporal  | 64.6±2.8         | 65.6±3.5 | 63.4±2.8         | 62.9±3.9 | 2.9    | 0.1  |

Table 2.2: T2 given in milliseconds; all continuous data presented as mean  $\pm$  standard deviation. ANCOVA is for total lobar (i.e., combined right and left) measures;  $df=(1,38)$  for all analyses.

no other significant group differences in lobar white matter T2 covaried for age.

### 2.1.3.2 Compartmental

Repeated measures ANCOVA revealed a significant main effect of diagnosis with no significant interactions involving diagnosis. *Post-hoc* analyses revealed that patients had an overall increase in white matter T2 of the bridging and radiate white matter compartments, with age as a covariate. These results are presented in Table 2.3.

| WM compartment | Autism   | Control  | ANCOVA |      |
|----------------|----------|----------|--------|------|
|                | (n=21)   | (n=20)   | F      | p    |
| Radiate        | 66.7±2.0 | 64.9±2.3 | 5.3    | 0.03 |
| Sagittal       | 66.0±2.0 | 64.8±2.2 | 2.2    | 0.15 |
| Bridging       | 63.7±2.5 | 61.5±2.6 | 5.9    | 0.02 |

Table 2.3: T2 given in milliseconds; all continuous data presented as mean  $\pm$  standard deviation. ANCOVA is for total compartmental (i.e., combined right and left) measures;  $df=(1,38)$  for all analyses.

## 2.1.4 Discussion

### 2.1.4.1 Limitations

The results of this study need to be interpreted in light of some limitations. The sample size is small and there may have been insufficient power to detect other effects, potentially of lesser magnitude, associated with regions for which the current statistical tests were nonsignificant. The lack of female subjects prevents any conclusions that can be drawn as to the relevance of the results to females with autism. At the same time, given the known gender differences in the prevalence and severity of autism [84], and in brain development [85], the exclusion of females in this study may have highlighted group differences between controls and patients by removing gender-dependent variables affecting neurodevelopment. A number of patients in the present study were taking psychotropic medication and/or required sedation with midazolam, which could potentially have influenced the results.

Although more robust T2 quantification techniques exist, the GESFIDE sequence used in this study has several advantages, including the ability to measure both T2 and T2', whole brain coverage in an acceptable scan time and insensitivity to RF pulse imperfection [75]. However, possible limitations of this sequence include slice profile differences between R2\* ( $1/T2^*$ ) and R2 ( $1/T2$ ) images, which could lead to errors in the determination of T2 near sharp borders [86]. Further, comparisons to other T2 studies are restricted by the varying T2 quantification methods used since absolute T2 measurements are inherently dependent on the type of sequence and parameters used [87, 88].

Image registration and normalization present many advantages for the analysis of data but the potential for image misregistration exists [89]. Further caution is warranted by the use of an adult template as the target image for the spatial regis-

tration, though given that anatomical variations between adults and children brains are small compared to the scale of the brain regions studied, the use of an adult template is still feasible. Indeed, several authors have reported that the pattern of results in studies using SPM are the same whether a study-specific pediatric template or a standard adult template is used [90]. Even when comparisons are made at a smaller scale between groups of adults and children, statistical comparison between groups in a common space has been shown to still be feasible [91]. Furthermore, the robustness of our analysis benefits from the fact that we are comparing the average voxel T2 values over a large volume instead of comparing individual voxel intensities or deformation parameters on a voxel by voxel basis (e.g. voxel based morphometry).

Measurements of the intrinsic T2 times of water protons in brain tissue are sensitive to several factors, including water content, tissue iron stores [61,62] and cerebral blood flow [92]. The lack of group differences in T2' in the initial study [67], a more specific index of iron content, suggests that the differences seen in T2 between patients with autism and comparison subjects are not due to differences in iron content. T2 can be affected by blood flow or volume. However, as cerebral blood flow is greater in grey matter than white matter, the lack of group differences in global grey matter T2 or T2', also in the initial study, suggests that differences in cerebral blood flow would be insufficient to account for the group differences seen in the present study. As the increased T2 in frontal and parietal white matter seen in patients with autism is unlikely to be fully accounted for by differences in tissue iron content or blood volume, it is most likely a result of pathophysiological abnormalities in the tissue microstructure of white matter.

Multiple components can contribute to the signal measured in an imaging voxel. In the case of T2 imaging, careful sampling of the MRI signal has revealed that T2 measurements in white matter are actually the contribution of three components.

No attempt was made to detect multiple T2 components in the present study, as a reliable separation using the GESFIDE sequence data would have been impossible, especially given the limited number of gradient echoes acquired [93]. Nevertheless, the GESFIDE acquisition with the gradient echo spacing used in this study would have been short enough to be sensitive to all these components, including the shortest component attributed to myelin water. This suggests the possibility that the group differences seen here may be attributable to differences in myelin water. However, the only way to definitively determine this is to use a sequence designed specifically to assess myelin water [94]. Multi-exponential T2 decay in white matter is the focus of the work presented in chapters 3 and 4.

#### **2.1.4.2 Relevance to other imaging studies**

White matter abnormalities in autism have also been reported using DTI, which is sensitive to diffusion properties of brain tissue caused by changes in myelination, axonal number, diameter and orientation [95]. As the information obtained from DTI metrics such as FA are suggested to be complementary to, but not necessarily correlated to, transverse relaxation time measurements [96], the findings of the present study complements and extends previous DTI findings of white matter abnormalities in autism [15].

From a functional perspective, fMRI studies have reported abnormal activation in the parietal region for various tasks such as detection tasks [97] and working memory tasks [98]. Also associated with the parietal region, differences in visuo-spatial tasks [99] are especially interesting since individuals with high functioning autism tend to perform better on these than healthy controls. It has been suggested that aberrant functional integration might underlie these processing abnormalities, which is in keeping with the under-connectivity theory and our findings of abnormal T2 in

parietal white matter [99].

The increased right-sided white matter T2 alongside increased T2 of the bridging compartment, made up mostly of the corpus callosum, is consistent with findings of abnormal brain lateralization in autism. Functional imaging studies have reported abnormal activation patterns, especially in language tasks [100], presenting evidence for atypical lateralization of brain functions. A thorough analysis of morphological asymmetry in a group of children with high functioning autism has also reported abnormalities in regions associated with language function, with abnormalities of the frontal lobe being more severe [101].

Increased radiate white matter T2 was hypothesized based on the assumption of further concordance with volumetric abnormalities [71]. White matter development is dynamic through the early years and links may exist relating the true age of onset and timing of abnormalities. Radiate white matter does not undergo myelination until late in the first year of life with the frontal and prefrontal regions continuing myelination later [102]. This puts forth further evidence linking our increased white matter T2 to potential abnormalities of myelin or myelination.

The present results, in conjunction with evidence from other brain imaging modalities (structural MRI, DTI) suggest abnormalities in white matter in autism. Given its importance in cortical-cortical communication, abnormalities of white matter suggest the potential for abnormal cortical connectivity. Abnormalities of cortical connectivity could lead to disruption of psychological or neurological functions that are dependent on the coordination or integration of different brain regions. It has been proposed that autism is due to aberrant neural connectivity which results in the underdevelopment of the long-distance, integrative connections within and between cortical systems and which results in deficits of complex information processing [30].



Abnormalities of the white matter microstructure in autism as indicated by increased white matter T2 seen in patients may represent a neurobiological basis for aberrant cortical connectivity.

### **2.1.5 Conclusion**

In conclusion, the results of regional T2 abnormalities presented in this study suggest pathophysiological differences of the white matter microstructure which may be localized to specific regions of the cerebrum and are relevant to the concept of aberrant connectivity in autism. In the following chapters, future work will focus on methods that may allow characterizing the T2 distribution to further specify the origin of T2 abnormalities in autism.

## **2.2 T2 abnormalities of the basal ganglia in Tourette syndrome**

### **2.2.1 Introduction**

Neuroimaging studies of TS, as reviewed in chapter 1, have provided support for the implication of the basal ganglia and thalamus in the pathophysiology of the disorder. To our knowledge, only one study to date has reported T2 measurements in TS. Peterson and colleagues [103] reported increased T2 asymmetry of the insular cortex, frontal white matter, putamen and caudate nuclei in a group of 14 adults with TS when compared to healthy controls by comparing differences between matching regions in the right and left hemisphere. Differences of absolute T2 values between groups were also found in the right and left amygdala and the red nucleus, but not

in other CSTC components [103].

As such, no previous study has examined components of the CSTC in children and adolescents with TS using T2 imaging. The objective of this study was to quantitatively evaluate T2 relaxation times of CSTC components in a group of children and adolescents with TS. Based upon the results of structural and functional brain imaging studies in TS, we hypothesized that we would find increased T2 and abnormal asymmetry in the caudate nucleus of the basal ganglia.

## **2.2.2 Methods**

### **2.2.2.1 Subjects**

Twenty-two males with TS between the ages of 6 years and 16 years participated in this study. Patients were recruited through the Centre for Pediatric Neuroscience at Children’s Hospital of Western Ontario and the TS program at the Child and Parent Resource Institute. The diagnosis of TS was made according to DSM-IV-TR criteria using the Schedule for Affective Disorders and Schizophrenia for School-Age Children (K-SADS;) [74]. Ratings of tic severity were made on the day of the MRI scan using the Yale Global Tic Severity Scale (YGTSS) [104]. Secondary tic disorders (i.e. those clearly caused by some other factor such as medication of neurological insult) were exclusionary, as were any DSM-IV axis I disorders other than ADHD, OCD and related conditions. A history of other neurological conditions, such as seizures, was also exclusionary. Fifteen patients had comorbid ADHD while none had OCD. At the time of the scan, six patients were medication naive and three others had been medication-free for over a month. The remaining patients were being treated with stimulants (n=3), dopamine antagonists (n=7), and clonidine (n=4). In order to complete their MRI scans, 15 patients required oral sedation with midazolam (n=4)

or chloral hydrate (n=11).

The group of control subjects overlapped with the control group of the autism study. As such, twenty-three males between the ages of 6 years and 16 years, drawn from the local community through advertisement and word of mouth, participated as control subjects in this study. They were assessed with the K-SADS to ensure that none had a major psychiatric disorder. Additionally, none had a personal history of neurological disorders or a first-degree relative with ADHD, OCD, or a tic disorder. Patients and controls were also assessed with the WISC-III or the Wechsler Abbreviated Scale of Intelligence, and a full-scale IQ of less than 70 was exclusionary.

The Health Sciences Research Ethics Board at The University of Western Ontario approved this study. The parents of all subjects provided written consent for participation in this study, while the subjects provided written assent.

#### **2.2.2.2 MRI acquisition, image reconstruction and image registration**

The MRI acquisition, reconstruction and normalization followed the previously presented methodology of section 2.1.2 exactly.

#### **2.2.2.3 Mean T2 measurements**

ROIs were components of direct and indirect CSTC pathways. We obtained a mean T2 measurement for each ROI by multiplying the T2 maps with specific ROI masks. Binary masks for each ROI (caudate, globus pallidus, substantia nigra, putamen, thalamus, and subthalamic nucleus) were generated in standard space with the Pick-atlas toolbox for Matlab (Wake Forest University) [79] and shown in figure 2.7. Each subject's T2 maps were then multiplied by the binary masks and mean T2 values

calculated for each ROI.

#### **2.2.2.4 Statistical analysis**

Group differences in T2 were investigated using a Repeated-Measures ANCOVA. In the analysis, T2 was the dependent variable, diagnosis (TS or control) was the between-subjects factor, and region (caudate, globus pallidus, substantia nigra, putamen, thalamus, and subthalamic nucleus) and side (left and right) were the within subjects factors. Significant main effects of diagnosis or higher order interactions involving diagnosis ( $p < 0.05$ ), were examined for each region and side individually with ANCOVAs to identify the region(s) that contributed to the significant main effect or interaction. Although age did not differ significantly between the groups, the age range in this study was wide. Once more, given the changes in T2 described in childhood [82], we covaried the statistical analysis of T2 for age to reduce error variance and increase statistical power.

### **2.2.3 Results**

There were no significant differences between groups in terms of age, race, height, non-verbal IQ, or full-scale IQ. Patients with TS did have a significantly lower verbal IQ (table 2.4).

Repeated measures ANCOVA revealed a significant main effect of diagnosis. There were no other significant interactions involving diagnosis. *Post-hoc* analyses revealed that patients had an overall increase in caudate T2 ( $p < 0.001$ ) as well as an increase in both left ( $p < 0.001$ ) and right ( $p = 0.01$ ) caudate T2. There were no other significant differences to report. All results are presented in table 2.5.

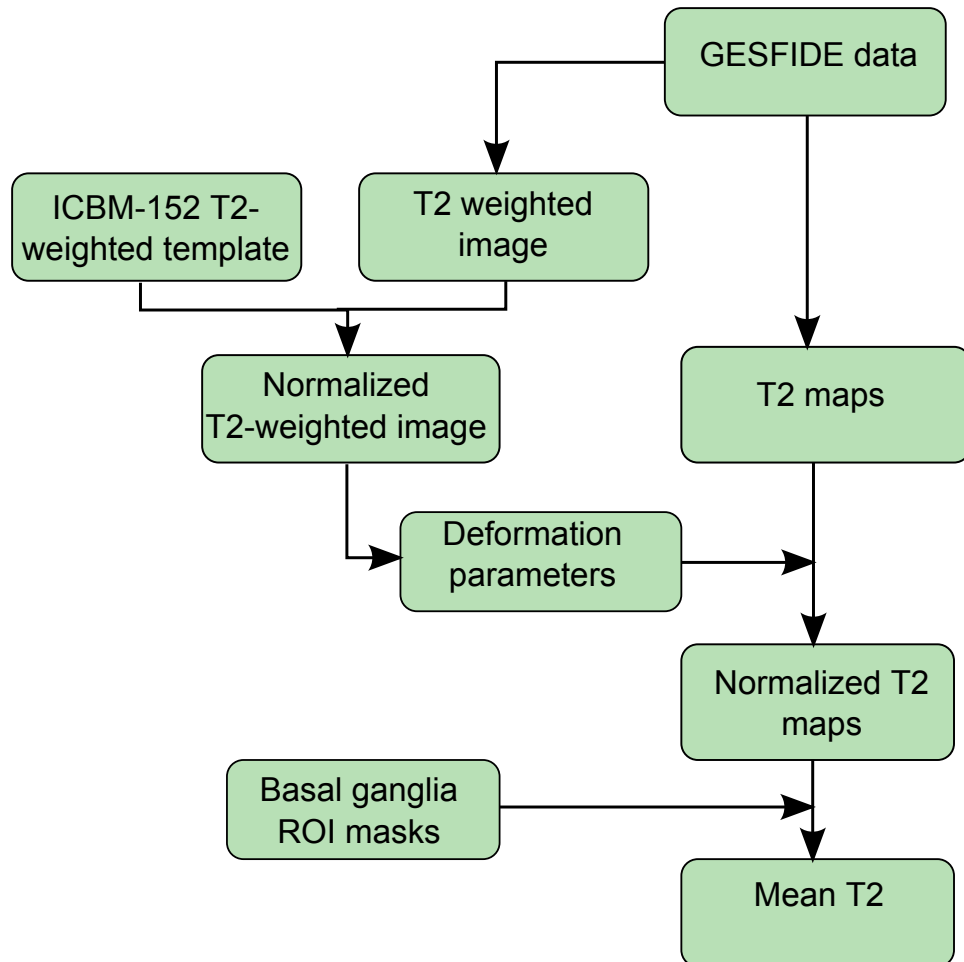


Fig. 2.6: Flowchart outlining the steps involved in the image reconstruction from the GESFIDE data, the spatial normalization into standard space and the calculation of the mean T2 of each ROI

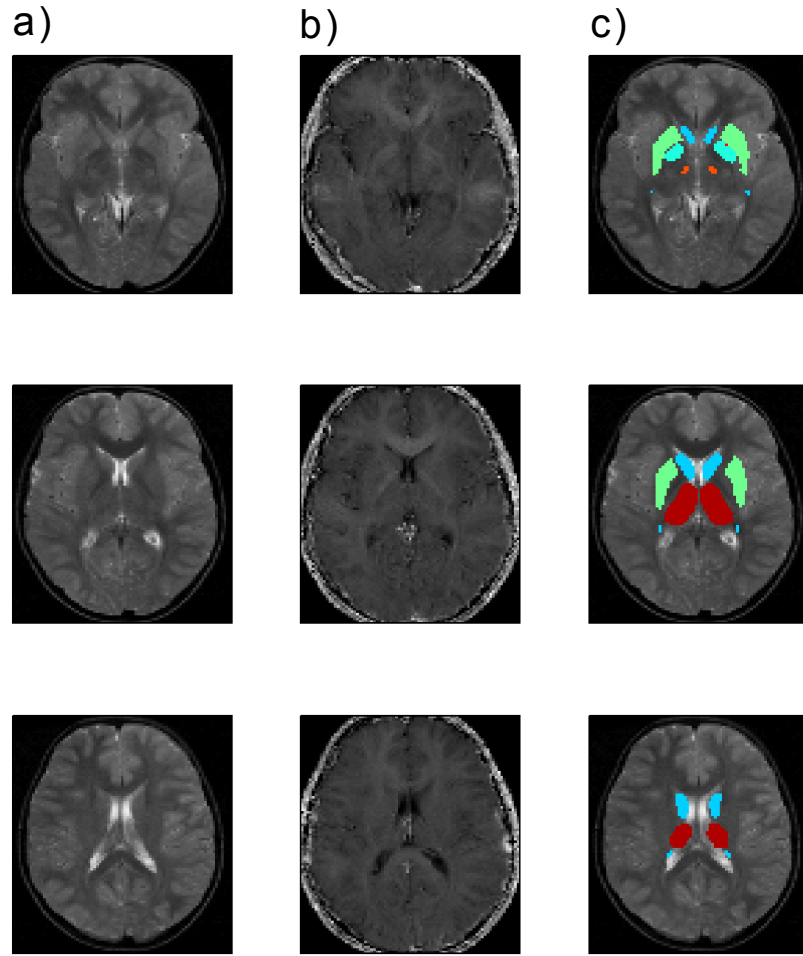


Fig. 2.7: Three axial slices presenting, column-wise, in standard MNI space: a) T2-weighted images, b) R2 maps, and c) ROIs. The caudate is in blue, the globus pallidus in teal, the putamen in green, the substantia nigra in orange and the thalamus in red.

|                  | Patients<br>(n=22) | Controls<br>(n=23) | Statistic    | p    |
|------------------|--------------------|--------------------|--------------|------|
| Age (yr)         | 10.8               | 10.8               | $t = 0.1$    | 0.9  |
| Height (cm)      | 142.0              | 149.0              | $t = 0.3$    | 0.8  |
| Head circ. (cm)  | 54.8               | 54.8               | $t = 0.1$    | 0.9  |
| Handedness (R/L) | 20/2               | 23/0               | $\chi^2=2.2$ | 0.1  |
| Full scale IQ    | 95.4               | 105.2              | $t = 2.4$    | 0.02 |

Table 2.4: Subject demographics

| Region              | Patients (n=22) |          | Controls(n=23) |          | ANCOVA |       |
|---------------------|-----------------|----------|----------------|----------|--------|-------|
|                     | left            | right    | left           | right    | F      | p     |
| Caudate             | 73.5±4.8        | 77.1±5.9 | 70.3±3.9       | 74.8±6.5 | 12.0   | 0.001 |
| Globus Pallidus     | 56.4±2.3        | 56.6±2.7 | 55.8±3.6       | 55.4±3.4 | 1.0    | 0.3   |
| Putamen             | 63.8±2.1        | 61.0±2.5 | 63.1±3.3       | 60.2±3.3 | 0.6    | 0.4   |
| Substantia Nigra    | 65.5±3.3        | 66.3±3.9 | 65.7±3.2       | 66.4±3.5 | 0.2    | 0.7   |
| Subthalamic Nucleus | 61.6±2.2        | 63.7±2.3 | 61.4±2.4       | 62.5±2.8 | 0.6    | 0.4   |
| Thalamus            | 67.1±2.9        | 68.2±2.8 | 66.5±3.0       | 67.2±2.8 | 0.9    | 0.3   |

Table 2.5: T2 given in milliseconds; all continuous data presented as mean  $\pm$  standard deviation. ANCOVA is for total ROI (i.e., combined right and left) measures; df=(1,42) for all analyses.

## 2.2.4 Discussion

Transverse relaxation times were found to be higher in the caudate of patients with TS when compared to healthy controls while no significant differences were detected in other structures of the basal ganglia and the thalamus.

As previously noted, this is only the second study investigating T2 in patients with TS and the first in a pediatric population. Comparisons between the two studies are severely limited by this difference in patient groups as well as significant differences in methodology. Additionally, the majority of TS patients experience notable improvements in their tics as they reach adulthood, while the minority of TS patients who continue to have tics in adulthood typically present with more severe tics. Consequently, we would expect two groups at different stages of the disorder to present different neurophysiological abnormalities. This has been found, for example, in examinations of the caudate in TS, where one study found reductions in the putamen volume of adults with TS, but not in the putamen of children or adolescents [45].

Interpretations of the results of this study have the same limitations posed by our

subject group and data analysis as the autism study. Further, typical of a population of TS patients [105], many patients taking part in this study had comorbid ADHD. A comparison of T2 of patients with only TS and patients with comorbid ADHD showed no difference. However the sample size was small and the possibility that the findings may not be attributed to the pathophysiology of TS alone, but rather reflects T2 abnormalities of the caudate due to comorbid ADHD cannot be ruled out.

In addition to tissue fluid, T2 measurements in brain tissue are also sensitive to cerebral blood flow and volume [92]. Brain perfusion abnormalities in TS have been reported, notably hypo-perfusion of regions associated with fronto-striatal circuits, including the left caudate [106]. A further study showed a decreased metabolism of the left caudate which correlated with tic severity [107]. In contrast, increased blood flow of the right caudate has been reported [46] in adults during a tic suppression task. Although the possibility cannot be ignored, it is unclear if T2 changes caused by different blood flow characteristics between subject groups would be sufficient to account for the group differences in the caudate seen in the present study.

The T2 differences observed in this study may be accounted for by differences in the brain tissue microstructure of the caudate nucleus. According to a compartment model of T2 [108], increased water content, and/or increased compartment size within the grey matter microstructure could account for our observations. Whether these changes are causal or a consequence of some other underlying mechanism remains an important unanswered question.

The present findings are consistent with brain imaging studies of TS using other modalities which have reported abnormalities of the caudate. For example, a volumetric imaging study of a large cohort of both children and adult TS patients showed reduced caudate volume across both groups while differences in other structures were



dependent on comorbid disorders such as OCD and on the use of medication [45]. A study of monozygotic twins with TS also found the caudate volume to be smaller in those co-twins more severely affected by the disorder [48]. Further abnormalities of the caudate in TS have been reported in PET, fMRI, and DTI studies [109,110].

### **2.2.5 Conclusion**

In conclusion, the results of localized T2 abnormalities of the caudate nucleus within the basal ganglia presented in this study provides further evidence suggesting pathophysiological differences of subcortical grey matter tissue relevant to the concept of aberrant CSTC circuit function in TS. Future studies are needed to further examine the role of medication, comorbid diagnoses and gender, as well as the possible relationship between volumetric and T2 abnormalities.

## **2.3 Summary**

Transverse relaxation is the most fundamental contrast mechanism in MRI and quantitative assessments of T2, as presented in these studies, can provide further clues to underlying brain abnormalities in psychiatric disorders. In children with autism and TS, when compared with normal controls, the studies presented in this chapter uncovered increased T2 in regions relevant to prevailing hypothesis in each disorder using automated and replicable analyses. Though our studies have found T2 to be very sensitive to changes in neurobiology that may be related to differences in tissue microstructure, the lack of specificity renders interpretations difficult. We work towards addressing this limitation within the context of white matter research in autism in the following chapters.

# Chapter 3

## Multi-component T2 in white matter and myelin mapping

### 3.1 Introduction

The interpretation of T2 abnormalities, such as those reported in chapter 2, remain difficult despite the sensitivity of quantitative T2 measurements to small changes in the neurobiology of brain tissue. This may, in part, have limited the application of T2 mapping in the study of psychiatric disorders. However, for tissues such as white matter, where water may be compartmentalized into distinct water environments, careful sampling and analysis may lead to the detection of multi-exponential decay. As such, multiple T2 components may be quantified, lending more specificity to the measurements. This chapter begins by describing multi-component T2 (mcT2) research to date, with a summary of published methods in making these measurements (including those which were published after the studies contained in this dissertation were completed). The white matter T2 abnormalities in autism reported in chapter 2, combined with the conceptualization of autism as a distributed disorder, motivates the assessment of the feasibility of two novel methods capable of obtaining whole-brain mcT2 data in a reasonably short scan time.

## 3.2 Multi-component T2 in human white matter

### 3.2.1 Compartment model

The influence of the local cellular structure and environment on the phase coherence of the total magnetization is heterogeneous across the span of the imaging voxel. A useful simplification is to consider a compartment model, where the tissue microstructure is represented by distinct water pools. As seen in figure 3.1, we can immediately relate this concept to the white matter microstructure, where different water environments are bounded by structures such as the myelin sheath and the axonal body. Each pool may have a characteristic T2 time and is responsible for a fraction of the total measurable signal.

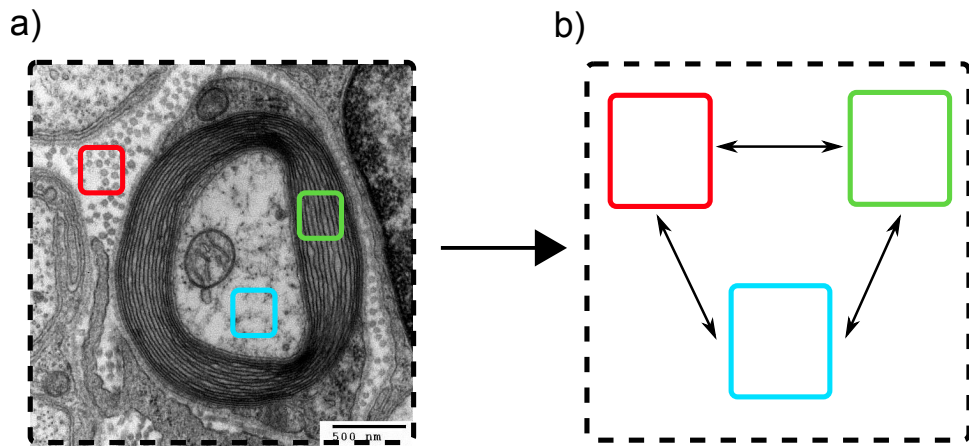


Fig. 3.1: A compartment model representation of human white matter. The squares are representative of water proton populations residing in distinct water environments, namely intra-cellular (blue), extra-cellular (red) and between layers of the myelin sheath (green). Water exchange is represented by the black arrows.

### 3.2.2 Water exchange

Water exchange (or mixing) occurs between each of the water compartments, with each water pool pair possibly described by a unique exchange time (figure 3.1b). This corresponds to the unique dynamics driving water exchange in each water pool with its neighbours, influenced by the permeability of any membranes separating them. Two exchange regimes are typically considered, corresponding to slow exchange and fast exchange, where the time scale is relative to the relaxation times of the T2 species involved. In the case of slow exchange, we expect the magnetization to experience the effects of a single water pool while undergoing relaxation. For the case of fast exchange, the influence of multiple water pools may bias mcT2 measurements or render the distinction of individual components impossible [111]. Thus, the assumption of slow water exchange is central to mcT2 methodologies.

### 3.2.3 T2 relaxation of brain tissue

Early experiments relevant to mcT2 in brain tissue were first conducted using *ex vivo* samples of frog sciatic nerve [112], liquid solutions [113], wood [114], excised brain tissue [115], crayfish [116], and guinea pigs [117]. Taken together, this early body of work provided compelling evidence that the compartmentalization of water in brain tissue would lead to multiple T2 components. Further, effective methodology for separating these components was developed in the context of the feasible data acquisition (i.e. sampling and SNR) and the expected biological distribution of these components [113].

The T2 distribution of the human brain was then investigated *in vivo* in studies [94, 118] which established the markedly different T2 distributions of grey and white matter. Within the context of a compartment model as introduced in section

3.2.1, grey matter exhibits an essentially mono-exponential T2 decay, as would be described by a single water pool. In contrast, the presence of heavily myelinated axons in white matter results in distinct water compartments. These distinct peaks in the distribution are attributable to the compartmentalization caused by the myelin sheath surrounding myelinated axons (figure 3.2). The shortest component has a T2 in the range of 10 to 40 ms and is ascribable to water trapped within the layers of the myelin sheath. The two longer components are assigned to intra and extra cellular water, which may not always be distinctively resolved with peaks in the range of 70 to 100 ms. In voxels which contain signal from cerebral spinal fluid (CSF), a third component can be detected with a T2 greater than 1 s.

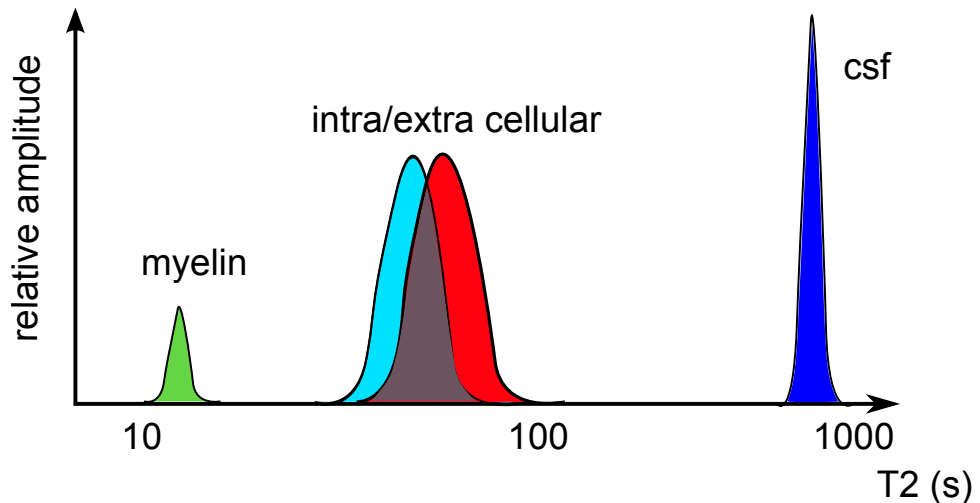


Fig. 3.2: The multi-component T2 distribution of white matter

This early work in characterizing the T2 distribution of white matter in the human brain established the MRI sequence which has since become the gold standard and is described in more details in section 3.3.2.1. Further, Whittall and colleagues introduced the myelin water fraction (MWF), which describes the proportion of the signal originating from myelin water to the total signal. Since then, the MWF has become the principal metric of interest when assessing white matter with mcT2 tech-

niques. Histological studies, as well as studies investigating white matter lesions in multiple sclerosis (MS) patients have shown that MWF is representative of myelin content [119].

### **3.3 Current multi-component T2 and myelin water mapping strategies**

This section reviews current mcT2 and MWF mapping strategies. While some techniques are able to characterize the T2 distribution, others are concerned mainly with quantifying the MWF, sometimes using *a priori* assumptions. The imaging sequences and the data analysis approaches used are described. The advantages and disadvantages are discussed with regards to their potential for imaging research. We omit methods which produce myelin weighted images (e.g. [120]) which are analogous to T2-weighted images in that, while being qualitatively descriptive, do not provide a quantitative measurement of the MWF.

#### **3.3.1 mcT2: an ill-posed mathematical problem**

Decomposing a sum of exponentials into its original components is an ill-posed mathematical problem. That is, in the presence of noise, multiple solutions may exist. To this end, much of the early work preceding the application of mcT2 *in vivo* aimed to develop an approach which worked in the context of the SNR and sampling parameters of the MRI acquisition, as well as the realistic biological composition of the sample. An adaptation of the non-negative least squares algorithm (NNLS) was extended to include a regularization term to reflect the increased residual expected when fitting a noisy signal [114]. The regularized NNLS (rNNLS) thus calculates the

amplitudes of components responsible for a given signal in the presence of noise to obtain a biologically appropriate solution [114].

The major advantage of the rNLS algorithm is that it makes no assumption as to the location or amplitude of components, other than assuming they are positive. However, its main drawback is the requirement for high SNR data, usually requiring multiple averages. With the expected T2 distributions of grey and white matter having already been rigorously described, fitting the data to a two or three component model has been used to lower the SNR requirements. Further, some of the strategies summarized in the following sections do not yield decay curves which lend themselves to decomposition by rNLS, requiring instead that the data be fit to an appropriate model.

### **3.3.2 Spin echo based methods**

At the root of all spin echo based approaches is the repeated refocussing of the transverse magnetization to sample the T2 decay, dubbed multi-echo spin echo (MESE). A brief description of spin echo based mcT2 methods follows.

#### **3.3.2.1 Optimized single slice MESE as the gold standard**

The earliest reports on the T2 distribution of white matter [94, 114, 118] have established what has since become the gold standard against which emerging techniques have been assessed. The approach consists of an optimized single slice implementation of MESE (MESE<sub>ss</sub>), where a series of 32 spin echoes spaced 8 to 10 ms apart are used to sample the T2 decay (figure 3.3). mcT2 decay curve analysis is sensitive to noise, therefore additional pulse sequence elements are used to mitigate sources of

systematic noise. In particular, the application of a large number of refocussing pulses can create stimulated echoes which arise from imperfect excitation and refocussing pulses [87]. A gradient scheme is used to dephase, or spoil, unwanted magnetization and prevent stimulated echoes. This implementation is limited to single slice imaging.

A rNNLS approach is typically used to decompose the T2 decay, from which the MWF is calculated. Since this approach makes no assumption as to the number and location of T2 components, its application has been useful in early descriptions of mcT2 in healthy grey and white matter, in compromised white matter such as MS lesions and in comparing the MWF to histological measures of myelin [121]. Though the MWF has gained the most traction as a metric of interest, the geometric mean T2 and its peak width are descriptive of intra/extra cellular water pools [119].

The use of NNLS or rNNLS requires high SNR data. When considering a well defined T2 distribution, a two- or three-component model may be more appropriate and result in better data fitting. It has been shown that the performance of a 3 pool model was identical to analysis with NNLS with high SNR data, but that the 3 pool model performed better as SNR decreased [122].

### 3.3.2.2 Linear combination of spin echoes

A common theme among spin echo based alternatives to MESE<sub>ss</sub> is the reduction of spin echoes used for data acquisition since they are, generally, responsible for all the effects which impede rapid, whole brain MWF mapping. The first method presented used the linear combination of spin echoes, by judiciously optimizing the SNR efficiency of fewer, non-equally spaced spin echoes [123].

To this end, filter theory, combined with *a priori* knowledge of the expected T2



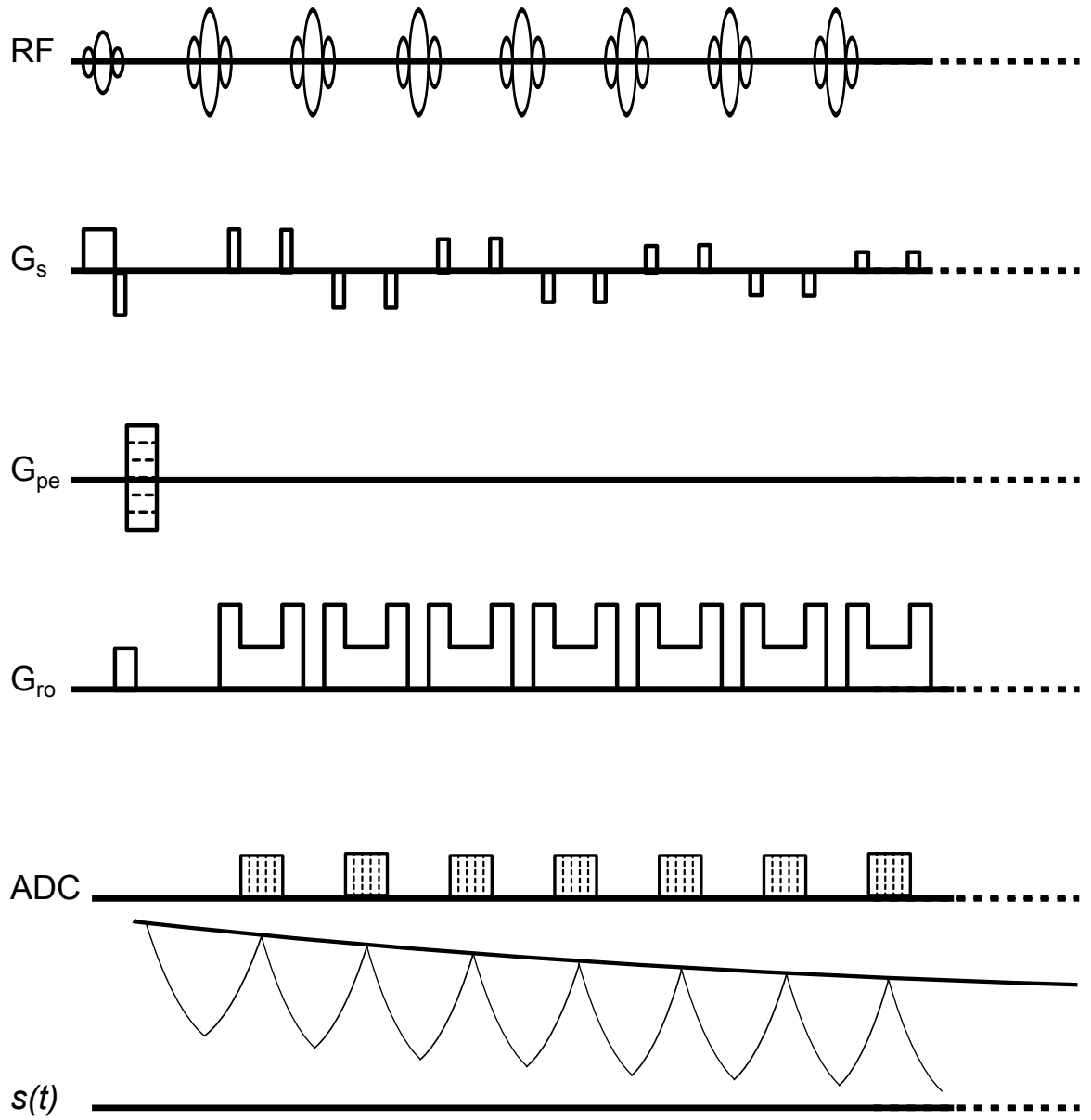


Fig. 3.3: MESE<sub>ss</sub> pulse sequence diagram

components, are used in this optimization. This concept was first implemented as a computationally faster alternative to NNLS in the analysis of single slice MESE acquisitions [123] but was later extended to reduce the actual image acquisition time [124]. The method used by Vidarsson et al. [124] is based on the acquisition of 3 spin echoes in a protocol which acquired 6 slices. Both phantom data and *in vivo* data were presented, the latter including images from a patient with MS. Since the method is predicated on the selective suppression of specific T2 components, variations in these components could have an impact on the MWF calculated.

### 3.3.2.3 MESE with variable TR

We recall that within the k-space formalism introduced in chapter 1, MRI data is frequency encoded, where the k-space data is linked to our final image by a two dimensional Fourier transform. As such, an alternative strategy is to reduce the repetition time during the acquisition of points in the periphery of k-space since their contribution to the T2-weighting of the image is negligible [125], however spatial resolution may suffer. In their paper, Laule et al., present a protocol which provides a modest 20% reduction in scan time. The equivalence to the gold standard MESE<sub>ss</sub> is shown in phantoms and in healthy volunteers.

### 3.3.2.4 T2 prep

T2-prep is a technique [126] which effectively emulates traditional T2-weighted images using magnetization preparation pulses. More commonly used in cardiac imaging, it has been recently implemented in MWF mapping [127, 128]. A series of T2-weighted images is obtained using this method, though only a single image is obtained per TR. Accelerated imaging is used to obtain the entire k-space coverage within each TR which means that points away from the centre of k-space are not truly T2-weighted.

This approach has been adapted for multi-slice imaging with both linear and non linear echo time spacing at 1.5T and 3T to establish a preferred protocol. This protocol was subsequently used in patients with MS [128], where correspondence was established between white matter lesions and reduced MWF using a 16 slice (5 mm thickness) 12-echo protocol. Limitations associated with spiral imaging, such as image blurring, as well as T1-weighting introduced by longitudinal recovery are effects which need to be considered in this implementation.

### **3.3.2.5 MESE with stimulated echo correction**

The occurrence and timing of stimulated echoes can be predicted given the timing of the imaging sequence parameters used. Capitalizing on this knowledge, an approach is presented which takes into account the effect of stimulated echoes on the T2 decay in the fitting algorithm [129]. This allows the use, without modification, of spin echo sequences typically available on most commercial MRI scanners.

### **3.3.2.6 MESE with 3D GRASE**

This recent technique based on a 3D acquisition where additional phase encoding is used instead of the slice selective excitation of a 2D acquisition, accelerates the acquisition of k-space data using combined gradient and a spin echo (GRASE) [130]. The centre of k-space, responsible for the bulk of the image contrast after the Fourier transform, is acquired at the spin echo while the periphery of k-space is T2\*-weighted and acquired with gradient echoes along the spin echo envelope. One concern noted by the authors was the short TR of 1000 ms used to achieve the clinically feasible scan time, which may have introduced T1-weighting in the quantification of T2 components.

### 3.3.3 Gradient echo based methods

Recalling equation 1.20, the signal decay in the absence of RF refocussing pulses which reverse the effects of static field inhomogeneities is described by the effective relaxation rate,  $T2^*$ . Based on this reasoning, we can expect  $T2^*$  decay to also consist of multiple contribution from the same water pools. This leads us to consider multi-component  $T2^*$  ( $mcT2^*$ ) decay analysis based on the acquisition of  $T2^*$  decay curves obtained with only gradient echoes using a multi-echo gradient echo (MEGE) sequence. By eliminating all refocussing pulses,  $mcT2^*$  effectively eliminates the potential for stimulated echoes and affords greater sampling density by way of shorter echo spacing. It is easily implemented as a multi-slice acquisition and significantly reduces the RF energy absorbed in the subject being imaged, called the specific absorption rate (SAR).

The possibility of performing myelin mapping by sampling  $T2^*$  decay was first investigated *ex-vivo* using a post mortem human brain specimens from two healthy individuals and another afflicted with MS [131]. MWF values calculated correspond well with the literature and MS lesions were properly represented on MWF maps. However, the greatest source of static field inhomogeneity, air/tissue interfaces, were not present in these fixed brain specimens as they were scanned in water filled containers.

The feasibility of  $mcT2^*$  decay *in vivo* is investigated in section 3.4. Our results remained unpublished, as they led us to conclude that this approach was not amenable to whole-brain myelin quantification. This conclusion is in contrast to that of Hwang et al. [132] who followed up on their initial post mortem study [131] by presenting *in vivo*  $mcT2^*$  data and calculated MWF maps. Their methods and findings will be compared to ours in more detail in section 3.4.4.

### 3.3.4 Steady state based methods

A final unique approach to quantify the myelin water fraction is based on a short-TR steady state acquisition, where the magnetization is not allowed to return to equilibrium before the next excitation pulse. This technique is based on the combination of two previous techniques, driven equilibrium single pulse observation of T1 (DESPOT1) and T2 (DESPOT2) extended to the multi-component case (mcDESPOT) [133–138]. This strategy is based on a two-pool model where T1 and exchange times must be included. By obtaining a large set of T1-weighted and T1/T2-weighted images over a range of flip angles, enough data is obtained to estimate the model's parameters.

The ability to reliably estimate parameter values based on a mcDESPOT acquisition has come under question given the sensitivity of the model to certain estimated values [139] as well as the precision actually attainable [140]. Further, though the acquisition provides complete brain coverage at great resolution, the MWF values obtained fall well outside the range typically reported in the literature [96].

## 3.4 mcT2\* *in vivo*: feasibility study

### 3.4.1 Introduction

Measuring the MWF by analyzing the T2\* decay was first attempted using a fixed brain specimen submerged in water [131]. Since the air/tissue interfaces found *in-vivo* are not represented in such an experiment, the effects of one of the major contributor of signal dephasing due to static field inhomogeneities (T2') could not be assessed. Field inhomogeneity effects, which would normally be reversed by the inversion pulse of a spin echo sequence, can be thought of as T2\* shortening effects, causing faster

decay of the signal and affecting its viability for sampling and decomposition into multiple components. This is especially the case for imaging at 3T, the field strength of our lab's current and future research protocols and becoming increasingly commonplace among other research centres.

The objective of this study was to investigate the feasibility of a multi-echo gradient echo acquisition to sample the  $T2^*$  decay and the viability of the signal near air/tissue interfaces causing significant  $T2^*$  shortening. We hypothesized that  $mcT2^*$  would be analogous to  $mcT2$  in terms of multi-exponential behaviour in grey and white matter, but that the signal would be greatly compromised in regions of severe field inhomogeneities such as those near the prefrontal sinuses.

## **3.4.2 Methods**

### **3.4.2.1 Study subject and MRI acquisition**

A single healthy male volunteer (age 26) underwent magnetic resonance imaging using a Siemens Verio 3T MRI scanner. The commercially available MESE and MEGE (figure 3.4) sequences were used to obtain sets  $T2$  and  $T2^*$  weighted images, respectively. Each image set were acquired in separate acquisition of the same slice after a localizer scan and shimming. Slice location was chosen to include the genu and splenium of the corpus callosum as well as prefrontal white matter just above the frontal sinuses. Each acquisition used 32 echoes, the limit imposed by the sequence software. The time of the first echo and the inter-echo spacing were set to the minimum values achievable. These and other relevant scan parameters for each acquisition are tabulated in table 3.1.

This feasibility study was conducted under a general MRI sequence and protocol

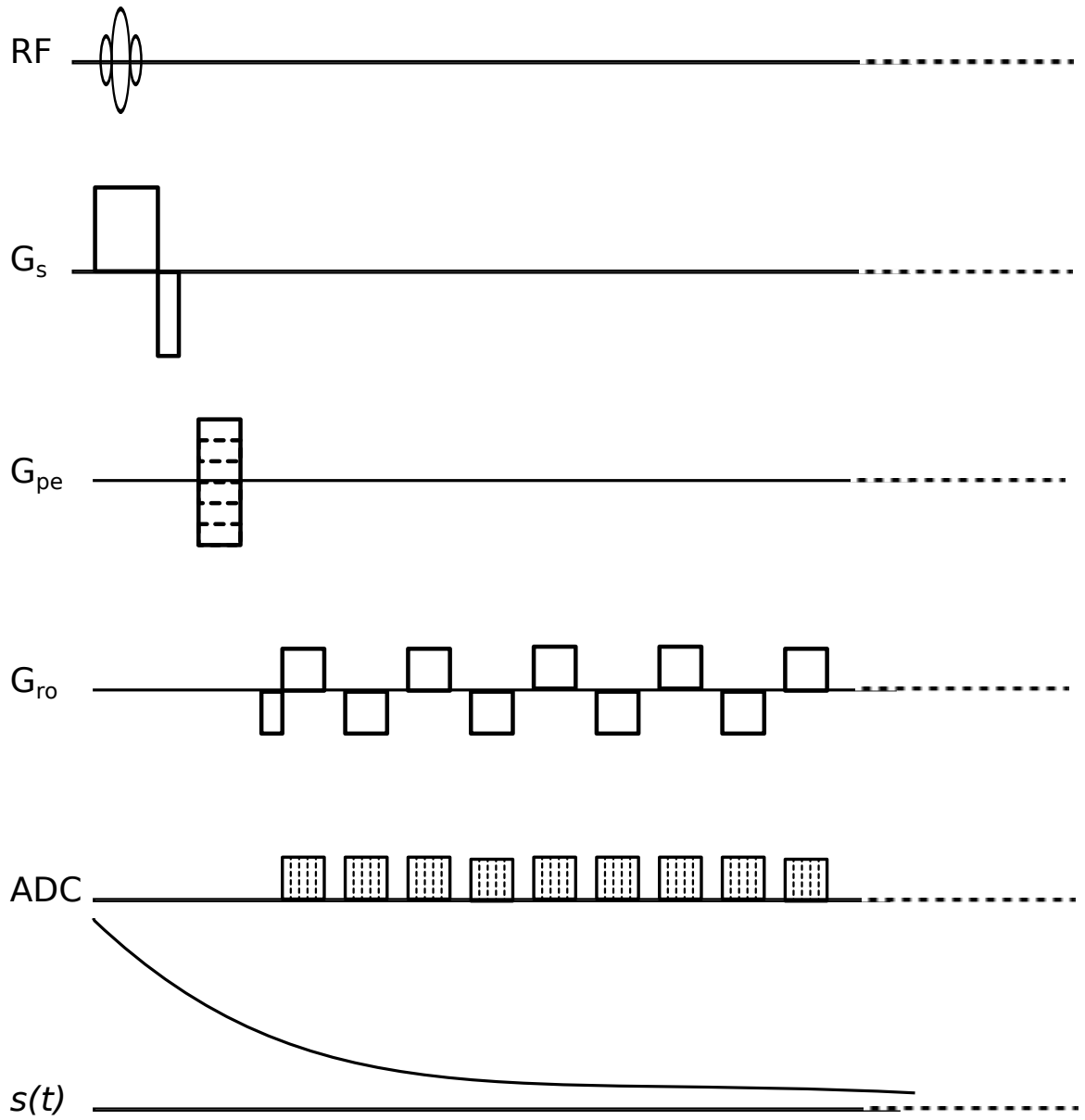


Fig. 3.4: MEGE pulse sequence diagram .

development ethics approval provided by The Health Sciences Research Ethics Board at the University of Western Ontario. The participant provided written consent.

|                            | MESE    | MEGE    |
|----------------------------|---------|---------|
| field of view (mm)         | 240     | 240     |
| matrix size (px)           | 128x128 | 128x128 |
| slice thickness (mm)       | 3.0     | 3.0     |
| TR(ms)                     | 2200    | 1500    |
| TE <sub>1</sub> (ms)       | 10      | 2.34    |
| $\Delta$ TE (ms)           | 10      | 1.52    |
| acquisition time (min:sec) | 4:40    | 3:11    |
| number of echoes           | 32      | 32      |
| bandwidth (Hz/px)          | 765     | 765     |

Table 3.1: MESE and MEGE acquisition parameters

### 3.4.2.2 Data analysis

Images, in DICOM format, were reconstructed online by the scanner software. All subsequent analyses were performed off-line in Matlab using in-house code purposely written for this study. Images were filtered using an anisotropic diffusion filter (ADF) with 5 iterations as described by Jones et al. [141] to increase the SNR of the images and improve the data fitting.

As an exploratory evaluation of regional T2' within the acquired slice, a T2 map was calculated from the spin echo data, a T2\* map was calculated from the gradient echo data, and T2' was calculated from the resulting T2 and T2\* maps.

NNLS was implemented in Matlab as described in other studies [94, 118], but without using a regularization term. This is in keeping with the exploratory nature of this study and because the effects of regularizing the distribution obtained from the T2\* decay is unknown. An array of 120 logarithmically spaced bins in the range of



15 ms to 2 seconds for T2 and 10 ms to 2 seconds for T2\* were used to fit the T2 and T2\* distributions. For spin echo data, T2 components with T2 times less than 40 ms were assigned to the short component of myelin water in the MWF calculation [119]. For the gradient echo data, a histogram was constructed to pick the upper bound the myelin water T2, which was then used for calculation for the MWF.

A bi-exponential model, representing a two-pool model, was also used to fit the data and evaluate the MWF. This model assumes no contamination from long T2 species (e.g. CSF) within the voxel and intra and extra cellular water components are inseparable. Expanding on the form of equation 1.13, the bi-exponential model takes the form:

$$s(t) = A_{my}e^{\frac{-t}{T2_{my}}} + A_{ie}e^{\frac{-t}{T2_{ie}}} + A_{bl} \quad (3.1)$$

where  $A_{my}$  and  $T2_{my}$  are the amplitude and T2 time of the myelin water component and  $A_{ie}$  and  $T2_{ie}$  are the amplitude and T2 time of the intra- and extra-cellular water component.  $A_{bl}$  represents the baseline of the noise floor. The bi-exponential model was also applied to the T2\* data, where the T2 components in equation 3.1 are replaced by their respective T2\* analogue.

### 3.4.3 Results

The location of the axial slice is shown in figure 3.5. The frontal sinuses, typically a significant source of static field inhomogeneity are clearly seen in the sagittal view.

The two series of 32 images acquired with the spin-echo and gradient echo sequences can be seen in figures 3.6 and 3.7 respectively. Signal drop-off due to T2\* shortening is highlighted in figure 3.7.

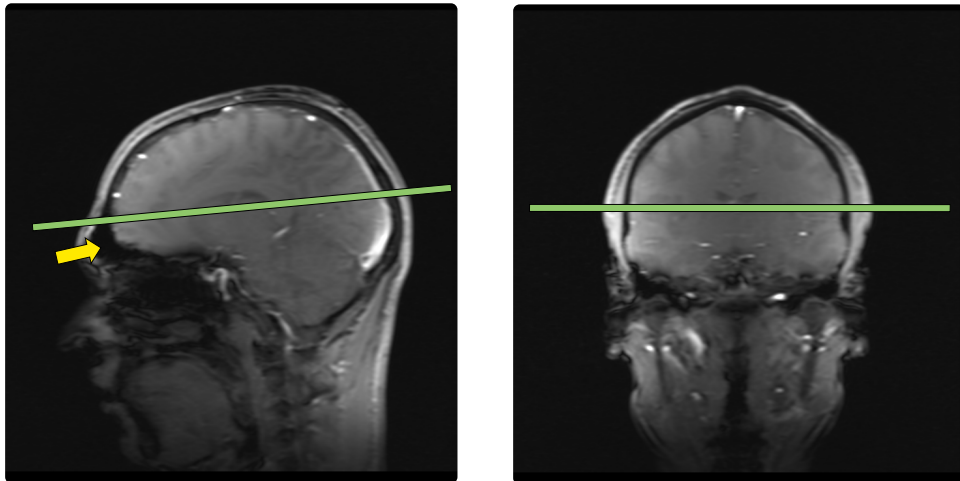


Fig. 3.5: Axial slice location superimposed on the sagittal and coronal localizer images. The frontal sinuses, a significant source of static field inhomogeneity, are highlighted by the yellow arrow.

An estimate of  $T2'$  is obtained by calculating  $T2$  and  $T2^*$  maps with a voxel-wise logarithmic fit to the spin echo and gradient echo data (figure 3.8). Though this calculation neglects the multi-exponential nature of the  $T2$  and  $T2^*$  decay, the calculated  $T2'$  maps is indicative of the magnitude of the static field inhomogeneities that will negatively impact the  $T2^*$  decay.

$T2$  and  $T2^*$  decay data were analyzed with NNLS. A  $T2^*$  histogram was generated and inspected to set the upper bound for the MWF calculation at 30 ms (figure 3.10). MWF maps, as calculated from NNLS and the bi-exponential model, are shown for  $T2$  (figure 3.9) and  $T2^*$  (figure 3.11). Spurious MWF values were set to zero in the MWF maps for clarity.

### 3.4.4 Discussion

The multi-exponential behaviour of  $T2^*$  decay of the brain *in vivo* was investigated at 3T in a single healthy adult volunteer. As expected,  $T2^*$  decay displayed a multi-

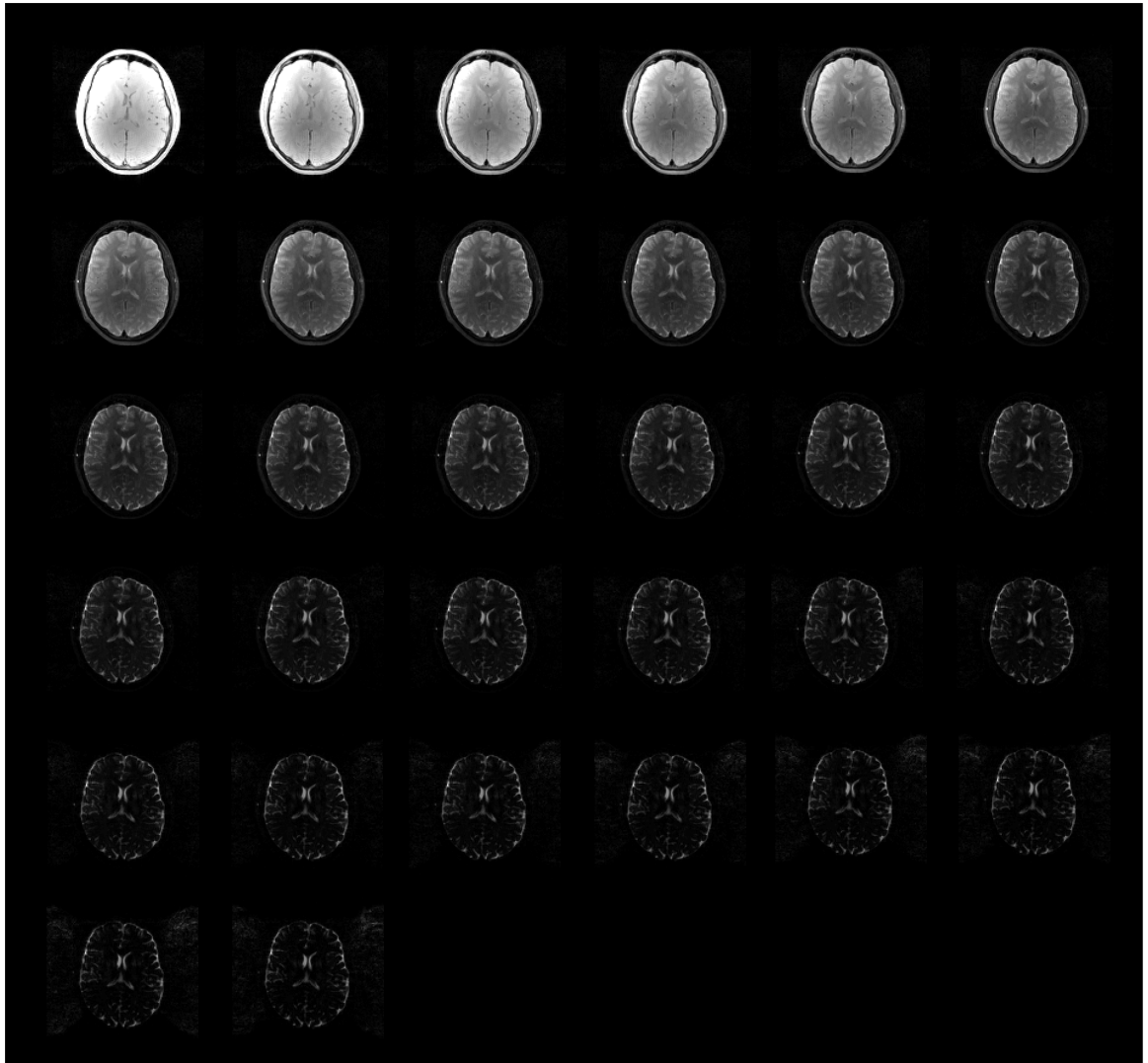


Fig. 3.6: The series of T2-weighted images obtained from the spin-echo acquisition.

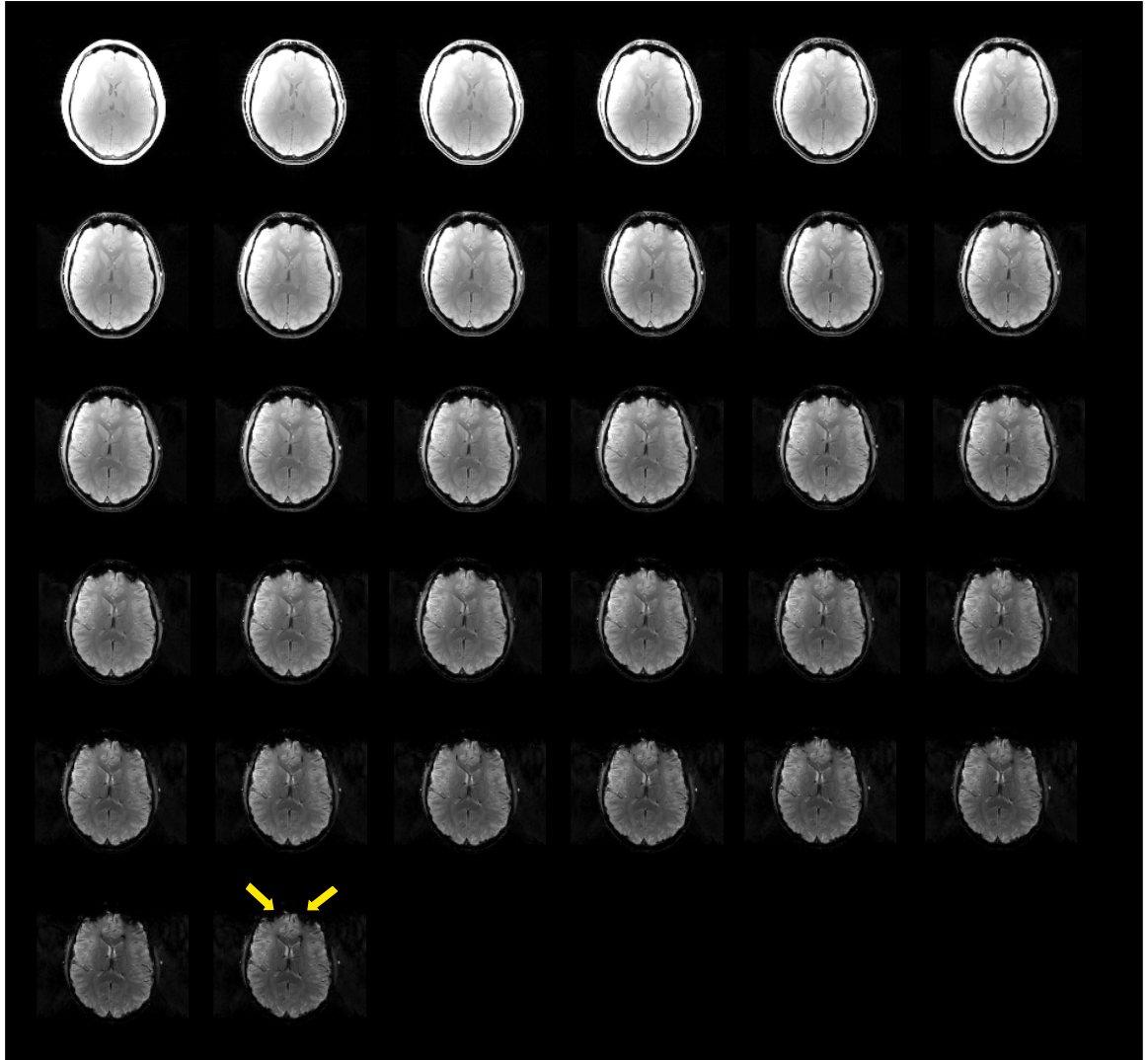


Fig. 3.7: The series of T2\*-weighted images obtained from the gradient-echo acquisition. Regions of rapid signal loss near the frontal sinuses are highlighted by the yellow arrows.

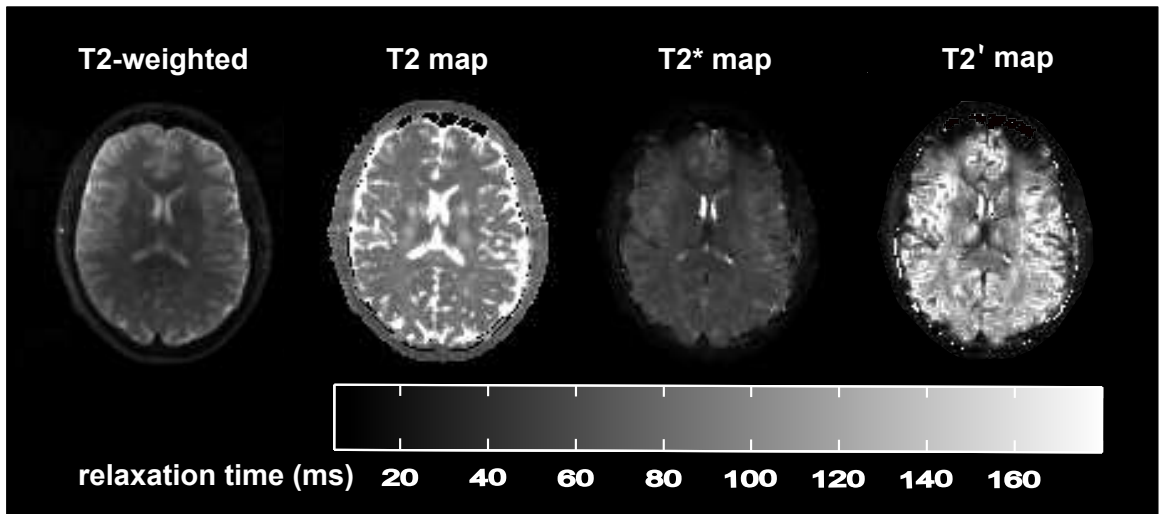


Fig. 3.8: From left: filtered T2-weighted image ( $TE=100ms$ ), T2 map, T2\* map and T2' map. T2 and T2\* maps are calculated via a logarithmic fit to the spin echo and gradient echo data, respectively. The T2' is calculated from the T2 and T2\* maps via equation 1.20.

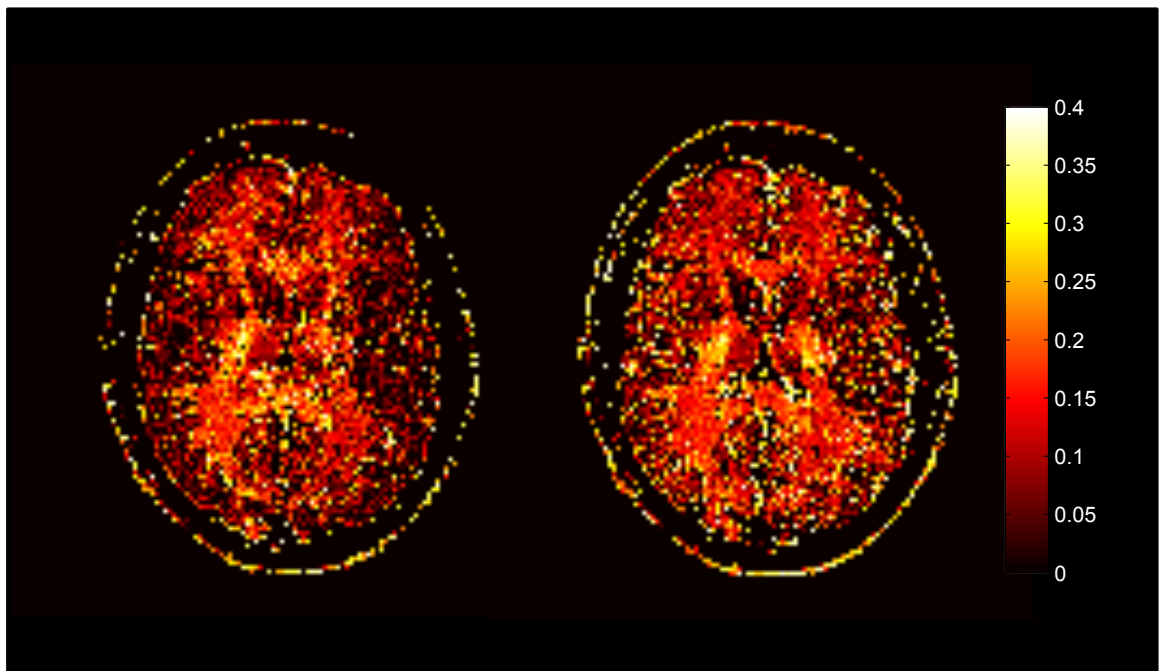


Fig. 3.9: Spin echo MWF map calculated from the T2 decay with NNLS (left) and bi-exponential model (right). Spurious MWF values set to zero for clarity.

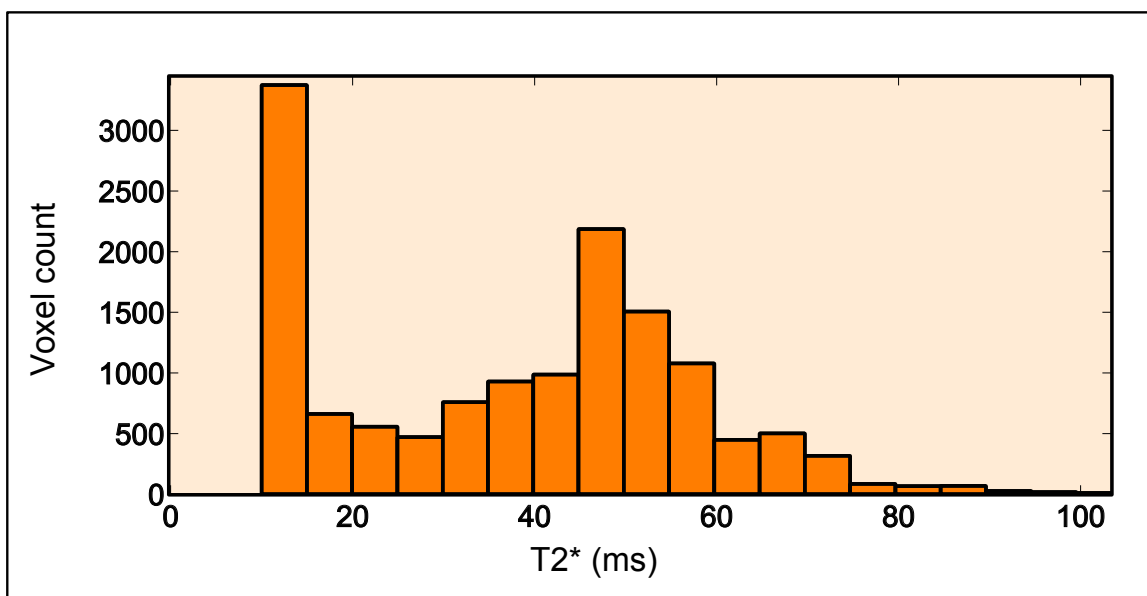


Fig. 3.10: Histogram of  $T2^*$  components as detected with NNLS.

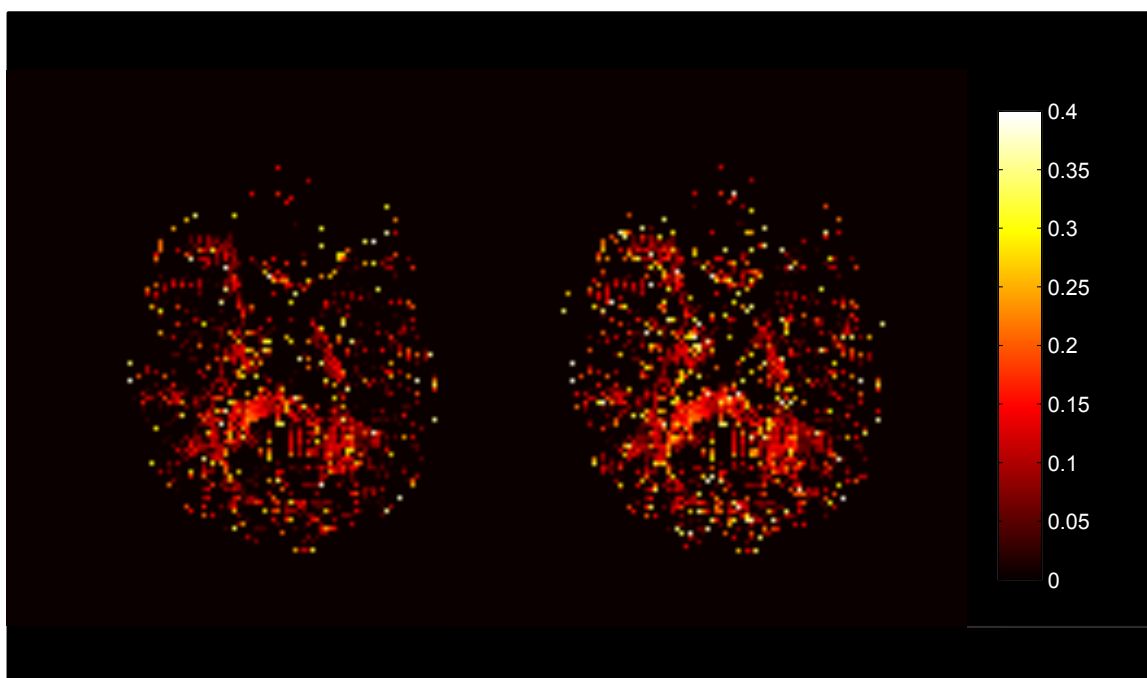


Fig. 3.11: Gradient echo MWF map calculated from the  $T2^*$  decay with NNLS (left) and the bi-exponential model (right). Spurious MWF values set to zero for clarity.

exponential behaviour in white matter analogous to the previously reported mcT2 decay. A short component was detected, predominately in white matter, with no *a priori* assumption using NNLS. Calculations of the MWF using a bi-exponential model showed remarkable correspondence to those calculated using NNLS.

The feasibility of quantifying the MWF at 3T is of particular importance to our research group as current and future protocols are expected to be implemented at this field strength. The bulk of the data presented within the context of mcT2 methodology to date have been acquired at 1.5T. A higher field strength affords higher SNR, but imaging artefacts may vary with field strength. In particular, the severity of magnetic susceptibility effects at air/tissue interfaces increases with field strength [142].

The experimental approach of this feasibility study was kept simple and straightforward to avoid clouding the effects under investigation. In particular, all imaging was limited to a single slice acquisition. This was to prevent any additional effects from inter-leaved slicing, particularly from the spin-echo sequence. Further, the data were analyzed with NNLS instead of rNNLS since the effects of regularizing the T2\* distribution are unknown, especially in the presence of significant field inhomogeneities. At any rate, rNNLS, though certainly offering more robust MWF quantification suitable for population studies, did not lend any additional benefits to the purposes of this feasibility study.

The spin echo acquisition presented here was based on a commercially available clinical sequence and did not feature the advanced spoiling scheme of the MESE<sub>ss</sub> sequence. As such, signal decay often suffered from echo to echo oscillations. The stimulated echo correction described in section 3.3.2.5 had not yet been published at the time this study was completed. Retrospectively re-analyzing the data would be of no further benefit, since the analysis would no longer share a correspondence to

the mcT2\* analysis.

NNLS was used to decompose the T2 and T2\* decay into a distribution of components, from which the MWF was calculated. NNLS, and its regularized version rNNLS, are often touted as robust methods of calculating the T2 distribution which make no *a priori* assumptions. However, in practice, the T2 distribution must be discretized (or ‘binned’) to allow computation, where the time needed for computation increases with the number of T2 bins. The range, number and spacing of these bins ultimately can affect the calculated MWF. Typically, logarithmic spacing is employed, as in this study, which provides more bins for the shorter components and fewer bins for the longer T2 components. While computationally convenient, logarithmic binning results in non-uniform spectral resolution of T2 components, which may distort MWF measurements. The range also needs to be considered. The endpoint of the long T2 component is usually of little concern, especially with logarithmic binning, but the value of the shortest T2 bin may have a large impact on the MWF calculation. Typically, this value is set at 10 ms even though shorter T2 species would still have a contribution (though small) to the total signal measured. Lowering the value of the first T2 bin much beyond 10 ms results in a ‘garbage bin’ effect, which colloquially describes the assignment of noise to these short T2 values.

The upper bound chosen for the mcT2-based MWF calculation has been well established in previous studies, which is not the case for mcT2\*. A histogram of the NNLS decomposition of all brain tissue voxels let us establish the upper bound for calculating the MWF based on mcT2\*. However, in regions of short T2', we expect the MWF upper bound to be further reduced which is why the calculation of MWF near regions of short T2' result in spurious values.

In fact, we can consider the T2\* shortening of two components individually: the



short T2 component with  $T2_{my} = 25$  ms and a longer T2 component with a  $T2_{ie} = 80$  ms, attributed to myelin and intra/extra cellular water respectively. The effective relaxation rate,  $T2^*$ , is the result of additional phase dispersion due to a local magnetic field inhomogeneity. This phase dispersion can therefore be described by the same  $T2'$  value for both components. Thus, the estimate of  $T2'$  as obtained in figure 3.8 can serve to calculate the effective relaxation rate of each component, that is  $T2_{my}^*$  and  $T2_{ie}^*$ . With  $T2'$  value in the range of 25 ms, as measured in the frontal lobes,  $T2_{my}^*$  and  $T2_{ie}^*$  would be shortened to 12 ms and 19 ms respectively.

Effectively,  $T2^*$  shortening in regions of severe field inhomogeneity renders the two components undistinguishable. This is clearly seen in the frontal area of the MWF maps calculated from the  $T2^*$  data (figure 3.11). The calculation of the MWF via both NNLS and the bi-exponential model results in spurious values in these areas since both components, even if separable, fall within the T2 range assigned to myelin water.

Shortly following this feasibility study, the first report of a similar implementation was published by the same research group who initially proposed  $mcT2^*$  by reporting on its application *ex vivo* [132]. Corrections were implemented to try and restore the signal loss due to field inhomogeneities, but only in the slice select direction. This field gradient correction was not sufficient in all brain regions, such as near the frontal sinuses. Whether this correction was applicable when considering multi-exponential decay was not described explicitly.

In this study, a two-component model, which presumes bi-exponential decay, was used alongside NNLS to calculate the MWF. The MWF maps obtained from both approaches show remarkable correspondence for both  $mcT2$  and  $mcT2^*$  analyses. A previously reported comparison of NNLS and a three-component model [122] presented similar findings and noted the relative better performance of the finite pool

model at lower SNR. The additional pool in the three-component model arises from the separation of the intra/extra cellular water pool used in the two-component model into an axonal water pool and a ‘mixed’ water pool representing all other measurable T2 species. However, the conditions under which this differentiation is possible are unknown and the bulk of published mcT2 studies do not report achieving it. In fact, some evidence from MS research may indicate that additional ‘middle’ components may not be detected unless the white matter structure is severely compromised, such as the white matter lesions encountered in MS [96]. As such a two-component model, as used here, appears suitable to calculate the MWF in normal appearing white matter, though caution is warranted due to partial volume effects from other T2 species such as CSF not included in the model.

### **3.4.5 Conclusion**

The ability to measure the MWF at 3T by analyzing the T2\* decay obtained from gradient echo imaging is predicated on the ability to separate the components despite the lower SNR afforded by gradient echo imaging and the T2\* shortening in regions affected by field inhomogeneities. However, the short T2' near severe sources of field inhomogeneity, such as the frontal sinuses, renders this impossible. As such, mcT2\* should not be considered suitable as a feasible technique for whole brain MWF quantification.

## 3.5 Feasibility of MWF quantification using gradient echo sampling of spin echoes

### 3.5.1 Introduction

The characterization of the  $T_2^*$  decay established in the mc $T_2^*$  feasibility study of section 3.4 inspired a novel acquisition strategy for the quantification of the MWF, which we introduce in this section, followed by simulations to establish its feasibility with realistic temporal SNR profiles. The approach is named multi-component gradient echo sampling of spin echoes (mcGESSE). Effectively, this method is a hybrid approach, incorporating both spin echo and gradient echo based approaches by combining the sampling density possible with gradient echoes with the greater signal viability made possible with spin echoes. The purpose of this study was to evaluate the theoretical ability of this method to calculate the MWF in a two-component model using simulated data and realistic (i.e.  $T_2'$  dependent) temporal SNR profiles.

### 3.5.2 Theory

The approach is an extension of the work presented by Yablonskiy and Haacke [86] to a bi-exponential model. Beginning from equation 3.1 with the addition of a function  $f(t)$  representing the additional dephasing due to static field inhomogeneities:

$$s(t) = (A_{my}e^{\frac{-t}{T_{2my}}} + A_{ie}e^{\frac{-t}{T_{2ie}}})f(t) \quad (3.2)$$

We consider an ideal noiseless signal at this point, thus the absence of  $A_{bl}$ , the baseline contribution to the signal representing the noise floor. The function  $f(t)$  represents the static field inhomogeneity effects characterized by the reversible transverse relax-

ation time  $T2'$ . In many instances, this function is also suitably represented as an exponential decay, as it was in analyses presented in chapter 2 using the GESFIDE technique. However, this is not always the case, so we let  $f(t)$  take on any functional form.

If we introduce a refocussing pulse that will create a spin echo at time  $TE$ , the symmetric nature of the rephasing caused by the spin echo is reflected by  $f(t)$  such that:

$$s(TE/2 < t < TE) = (A_{my}e^{-t/T2_{my}} + A_{ie}e^{-t/T2_{ie}})f(t - TE) \quad (3.3)$$

$$s(t > TE) = (A_{my}e^{-t/T2_{my}} + A_{ie}e^{-t/T2_{ie}})f(TE - t) \quad (3.4)$$

where  $f(t - TE) = f(TE - t)$ .

We can define a new quantity,  $s_{ratio}$ , based on the signal ratio taken at the same time interval  $n\Delta t$  before and after the spin echo (figure 3.12):

$$s_{ratio} = \frac{s(TE - n\Delta t)}{s(TE + n\Delta t)} \quad (3.5)$$

$$= \frac{A_{my}e^{\frac{n\Delta t - TE}{T2_{my}}} + A_{ie}e^{\frac{n\Delta t - TE}{T2_{ie}}}}{A_{my}e^{\frac{-n\Delta t - TE}{T2_{my}}} + A_{ie}e^{\frac{-n\Delta t - TE}{T2_{ie}}}} \quad (3.6)$$

For a normalized signal,  $A_{my} + A_{ie} = 1$  such that  $A_{my}$ ,  $T2_{my}$ , and  $T2_{ie}$  in equation 3.6 are the only three unknown quantities;

$$s_{ratio} = \frac{A_{my}e^{\frac{n\Delta t - TE}{T2_{my}}} + (1 - A_{my})e^{\frac{n\Delta t - TE}{T2_{ie}}}}{A_{my}e^{\frac{-n\Delta t - TE}{T2_{my}}} + (1 - A_{my})e^{\frac{-n\Delta t - TE}{T2_{ie}}}} \quad (3.7)$$

The quantities  $TE$ ,  $n$  and  $\Delta t$  are all determined by the acquisition parameters of the sequence.

The quantity  $s_{ratio}$  becomes our new objective function for curve fitting instead of the T2 decay (figure 3.13) and takes full advantage of the refocussing nature of the 180 degree RF pulse used to create the spin echo. More specifically, it is shown that since T2' is symmetric in time, by taking the ratio of the signal at equal time intervals before and after the spin echo, the contribution of T2' to this ratio is nullified, no matter its functional form. The absence of any terms involving T2' in the signal ratio affords a simple model. In practice, the effect of T2' underlying the original signal is still influenced by the T2\* dependent SNR of the acquisition. An additional consequence of this sampling strategy is the lack of any terms involving the baseline, such that sampling to the noise floor becomes irrelevant.

The purpose of this study was to evaluate the theoretical ability of this proposed acquisition scheme to calculate the MWF in a two-component model using simulated data and realistic temporal (SNR) profiles.

### 3.5.3 Methods

Two sets of parameters are prescribed for this simulation study: those describing the two-component model and those describing the data acquisition using the mcGESSE sequence.

#### 3.5.3.1 Simulated model parameters

The simulation of noisy data representing a native bi-exponential decay signal, subject to noise and T2', is represented by the following parameters:

1.  $A_{my}$ , the MWF as a fractional number from 0 to 1.

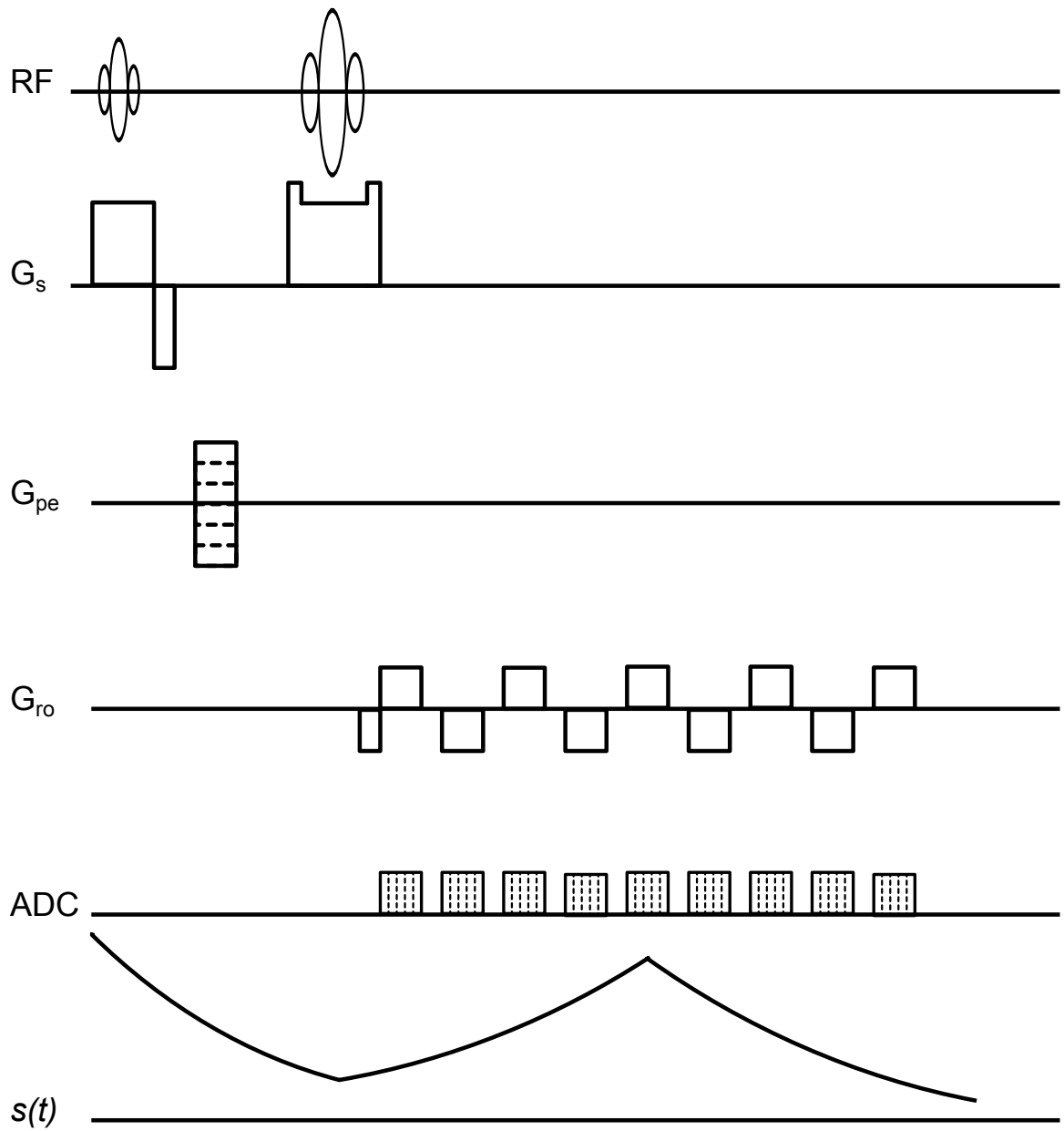


Fig. 3.12: Symmetric gradient echo sampling of the spin echo

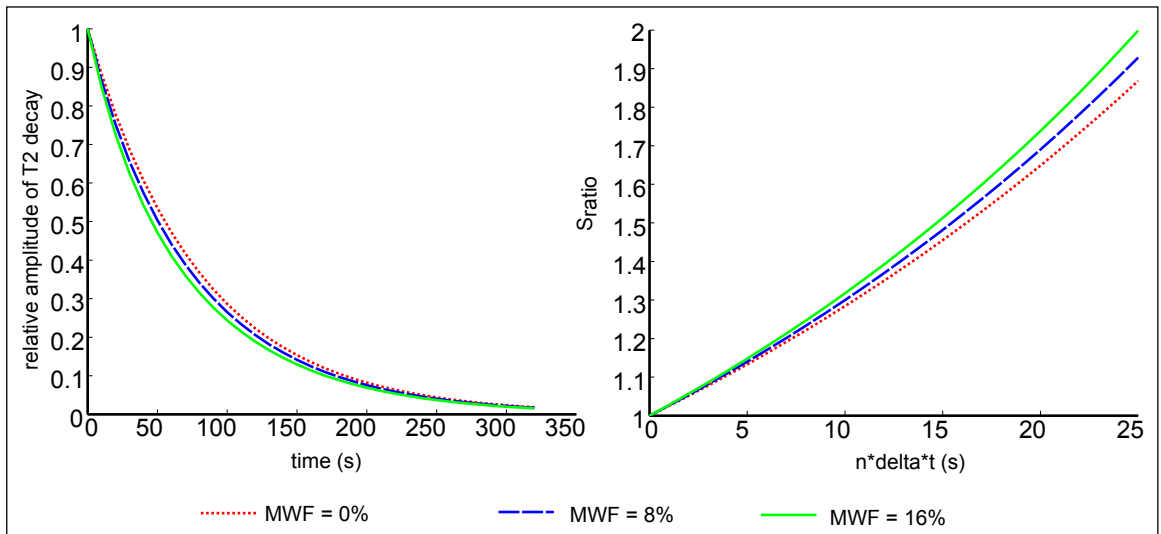


Fig. 3.13:  $s_{ratio}$  as an objective function compared to the T2 decay, for a spin echo time of 50 ms.

2.  $T2_{my}$  and  $T2_{ie}$ , the T2 times of the myelin water and the intra/extra cellular water peaks
3.  $T2_{my}^*$  and  $T2_{ie}^*$ , the effective relaxation times in the presence of field inhomogeneities described by T2'

As described by equation 3.7,  $A_{my}$  represents the MWF and is inherently normalized. Literature values for the MWF range from 0 to about 20%. The T2 times representing the peaks of the myelin and intra/extra cellular water have been reported to be  $\approx 20$  ms and  $\approx 80$  ms respectively using MESE<sub>ss</sub> [94,118] though many studies using alternative MWF mapping strategies do not report on these values explicitly. As seen in figure 3.8, T2' values throughout the cerebrum vary widely and are seen to be markedly lower near sources of field inhomogeneities. In white matter, T2' ranges from 30 ms in prefrontal regions, as seen in figure 3.8 to 150 ms in regions of mild static dephasing.

### 3.5.3.2 Simulated mcGESSE acquisition parameters

Based on the symmetric sampling of a spin echo, several acquisition parameters can be adjusted for the data collection. The mcGESSE pulse sequence acquisition parameters relevant to the simulations are:

1. Number of spin echoes used
2. Spin echo times,  $TE_1, TE_2...$  etc
3. Number of gradient echo *pairs* used,  $n$
4. Gradient echo interval,  $\Delta t$

The selection of these acquisition parameters were based on preliminary simulations and expected pulse sequence limits. Preliminary simulations showed that there was little benefit to more than two spin echo times. This is due to the weighted least squares approach, since data from later spin echoes have a lower SNR and carry a smaller weight towards the least squares minimization. Two spin echo times chosen to cover the expected span of  $T2_{my}$  and  $T2_{ie}$  with  $TE_1 = 20$  ms and  $TE_2 = 60$  ms.

Gradient echo spacing and number are mediated by the receiver bandwidth used in the acquisition, which will also affect the effective SNR of the acquired data (equation 1.18). In practice, timing parameters are primarily constrained by the limits imposed by the first spin echo time  $TE_1$ . Therefore, the gradient echo spacing values chosen were those possible at the  $TE_1 = 20$  ms.

### 3.5.3.3 SNR

The SNR of the acquired data is both spatially and temporally dependent. The spatial dependence arises from the sensitivity profile of the receiving coil as well as



the brain anatomy. The temporal dependence is principally due to the  $T2^*$  decay of the sample, which is of course a result of the intrinsic  $T2$  of the tissue and the  $T2'$  value associated with local sources of inhomogeneity. In addition to this spatial and temporal profile is the underlying background noise of the system hardware. Of particular relevance to mcGESSE is the receiver bandwidth, which, as mentioned in chapter 1 (equation 1.18), has a direct impact on SNR. A higher bandwidth will allow a shorter frequency readout time and smaller gradient echo spacing resulting in a greater number of data points at a lower SNR.

### 3.5.3.4 Iteratively re-weighted robust least squares

With  $s_{ratio}$  as an objective function, the curve being fit consists of the ratio of gradient echoes at times  $n\Delta t$  before and after each spin echo (equation 3.7). The  $s_{ratio}$  curves of each spin echo are concatenated together before solving for  $A_{my}$ ,  $T2_{my}$  and  $T2_{ie}$  in the least squares sense. These model parameter values are bound. The MWF is bound between 10 and 40%,  $T2_{my}$  between 0 and 40 ms and  $T2_{ie}$  between 40 and 120 ms.

The iteratively re-weighted robust least squares (IRRLS) curve fitting routine is described in more detail in appendix II and is outlined by the following steps:

1. An initial weighting of each data point was established based on temporal SNR
2. A preliminary least squares fit was performed using Matlab's trust-region-reflective algorithm, based on the interior-reflective Newton method.
3. To further decrease the sensitivity to noisy data points, the least squares fit was iteratively re-weighted and recalculated based on adjusted residuals until convergence.

### 3.5.3.5 Simulations

Simulations were conducted by generating sets of noisy data and fitting them to the model using IRRLS. The ability to investigate the MWF near sources of major magnetic susceptibility was investigated by establishing a worst case scenario with  $T2' = 30$  ms, a value obtained from the 3T dataset of the previous mcT2\* study.

The following parameter values were varied in the simulations:

1. T2 and T2\*, based on the case of no static dephasing, mild static dephasing and severe static dephasing
2. MWF values of 0, 8 and 16%, based on the range reported in the literature.
3. SNR, based on expected values at 3T, from a previous dataset
4. Number and spacing of gradient echoes, based on the timing achievable on our lab's MRI scanner.

The parameters were varied with these four goals in mind:

1. Investigate the effect of SNR on the performance of the data fitting
2. Investigate the trade-off between the number of gradient echoes acquired and the SNR decrease due to the higher bandwidth that would be required
3. Investigate the estimates of the MWF obtained across a range of MWF values
4. Compare the performance of the data fitting between regions of zero static dephasing to those with mild or severe static dephasing

The generation of noisy datasets and curve fitting were implemented in Matlab (Mathworks, Wisconsin) on a personal computer equipped with an intel i5 processor and 4 gigabytes of RAM. 10 000 iterations were performed for each simulation for

MWF values of 0, 8 and 16%.

### **3.5.4 Results**

#### **3.5.4.1 Inspection of previous 3T gradient echo image**

Inspection of the first image of the gradient echo dataset obtained in the mcT2\* study (TE=2.34ms), acquired with a receiver bandwidth of 765Hz/pixel, yielded an SNR range of 165 to 335 in white matter. T2' values, calculated from the combined T2 and T2\* maps (figure 3.8), were seen to range from 30 ms to >200 ms. As such, three values were used for the simulations corresponded to severe (T2' = 30 ms), mild (T2' = 150 ms) and zero (T2' =  $\infty$  ms) static dephasing.

#### **3.5.4.2 Starting estimates**

In the presence of noise, the starting estimates for the IRRLS may cause a significant bias of the estimated parameters. Four sets of starting estimates (listed in table 3.2) were assessed to determine a suitable set for all following simulations. The fourth set, though having the largest bias at a MWF of zero, provided the most accurate estimates at MWF values of 8 and 16%.

#### **3.5.4.3 Sampling density and receiver bandwidth**

Three simulations were devised to investigate the effect of sampling density and receiver bandwidth on MWF estimates. Parameters were chosen based on constraints expected to be imposed by the timing possible at a first spin echo time of  $TE_1 = 20$  ms, whereas the effect of receiver bandwidth is simulated by adjusting the SNR of the simulation, according to equation 1.18. All the simulations parameters are listed

|                      | Simulation 1 | Simulation 2 | Simulation 3 | Simulation 4 |
|----------------------|--------------|--------------|--------------|--------------|
| $A_{0,MWF}$          | 0            | 0            | 0.10         | 0.10         |
| $T2_{0,my}$          | 22           | 11           | 22           | 11           |
| $T2_{0,ie}$          | 77           | 120          | 77           | 120          |
| SNR                  | 250          | 250          | 250          | 250          |
| $\Delta t$ (ms)      | 1.5          | 1.5          | 1.5          | 1.5          |
| $n_1$                | 4            | 4            | 4            | 4            |
| $n_2$                | 14           | 14           | 14           | 14           |
| TE <sub>1</sub> (ms) | 20           | 20           | 20           | 20           |
| TE <sub>2</sub> (ms) | 60           | 60           | 60           | 60           |
| T2'                  | 150          | 150          | 150          | 150          |

Table 3.2: Simulation parameters used to assess starting estimates

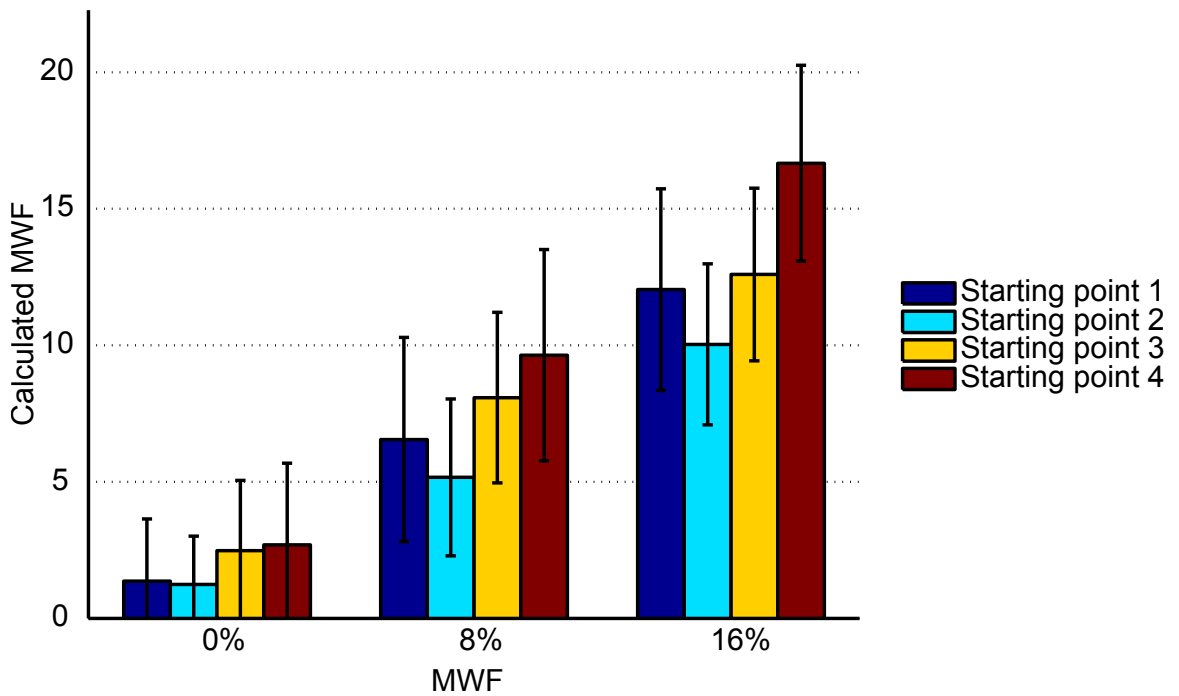


Fig. 3.14: Results of simulations with various starting points.

in table 3.3.

Each simulation yielded very similar results (figure 3.15), with nearly identical standard deviations. A lower number of sampling points yielded a greater overesti-

mate of the MWF at higher values of 8 and 16%.

|                   | Simulation 1 | Simulation 2 | Simulation 3 |
|-------------------|--------------|--------------|--------------|
| bandwidth (Hz/px) | 382          | 765          | 1148         |
| SNR               | 350          | 250          | 200          |
| $\Delta t$ (ms)   | 3            | 1.5          | 1            |
| $n_1$             | 2            | 4            | 6            |
| $n_2$             | 8            | 14           | 20           |
| $TE_1$ (ms)       | 20           | 20           | 20           |
| $TE_2$ (ms)       | 60           | 60           | 60           |
| $T_2'$            | 150          | 150          | 150          |

Table 3.3: Sampling density/receiver bandwidth simulation parameters

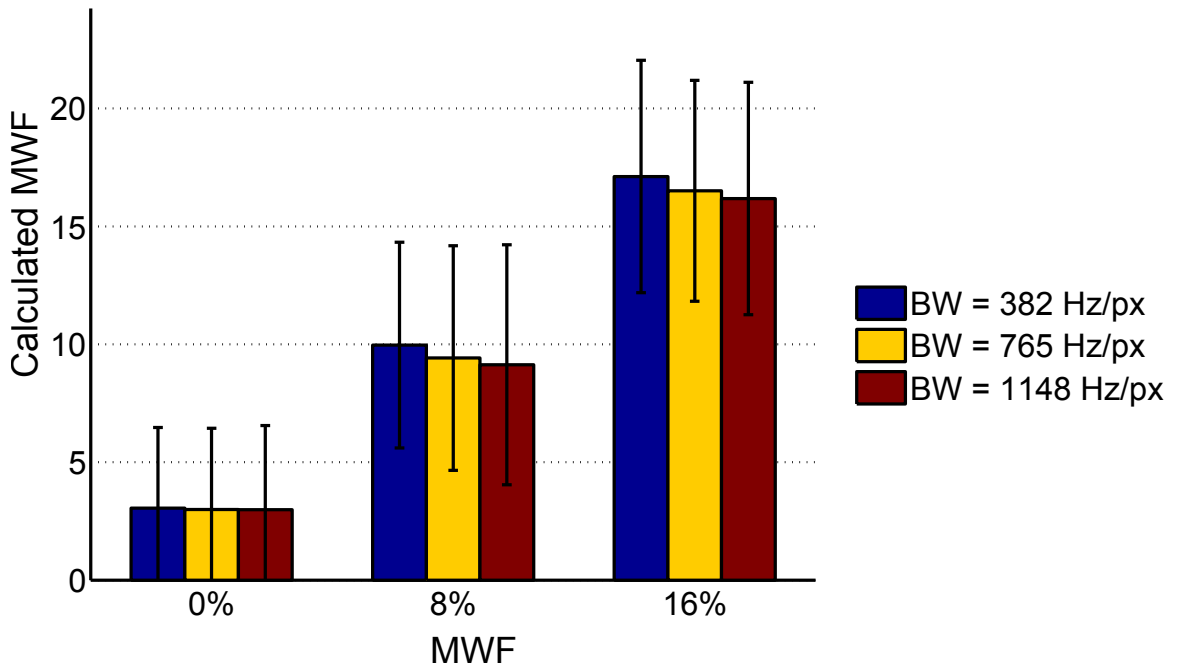


Fig. 3.15: Results of simulations with various sampling and bandwidths.

#### 3.5.4.4 SNR

The following simulations assessed the performance of IRRLS at SNR values of 165, 250 and 335 (table 3.4). As seen in figure 3.16, greater SNR resulted in decreased overestimate of the MWF for the case of MWF = 0%. At MWF values of 8 and 16%, there was no appreciable difference in the estimates, but the resulting standard deviations decreased appreciably, as would be expected.

|                      | Simulation 1 | Simulation 2 | Simulation 3 |
|----------------------|--------------|--------------|--------------|
| SNR                  | 165          | 250          | 335          |
| TE <sub>1</sub> (ms) | 20           | 20           | 20           |
| TE <sub>2</sub> (ms) | 60           | 60           | 60           |
| $\Delta t$ (ms)      | 1.5          | 1.5          | 1.5          |
| n <sub>1</sub>       | 4            | 4            | 4            |
| n <sub>2</sub>       | 14           | 14           | 14           |
| T2'                  | 150          | 150          | 150          |

Table 3.4: SNR simulation parameters

#### 3.5.4.5 Static dephasing (T2')

The last set of simulations investigated the effect of the level of static dephasing on the sampling of the spin echo envelope. Surprisingly, increased static dephasing introduced little bias to the MWF estimates for all three simulated values. Standard deviations of the estimates increased as the level of static dephasing increased (T2' decreased), similarly to the previous simulations with varying SNR values.

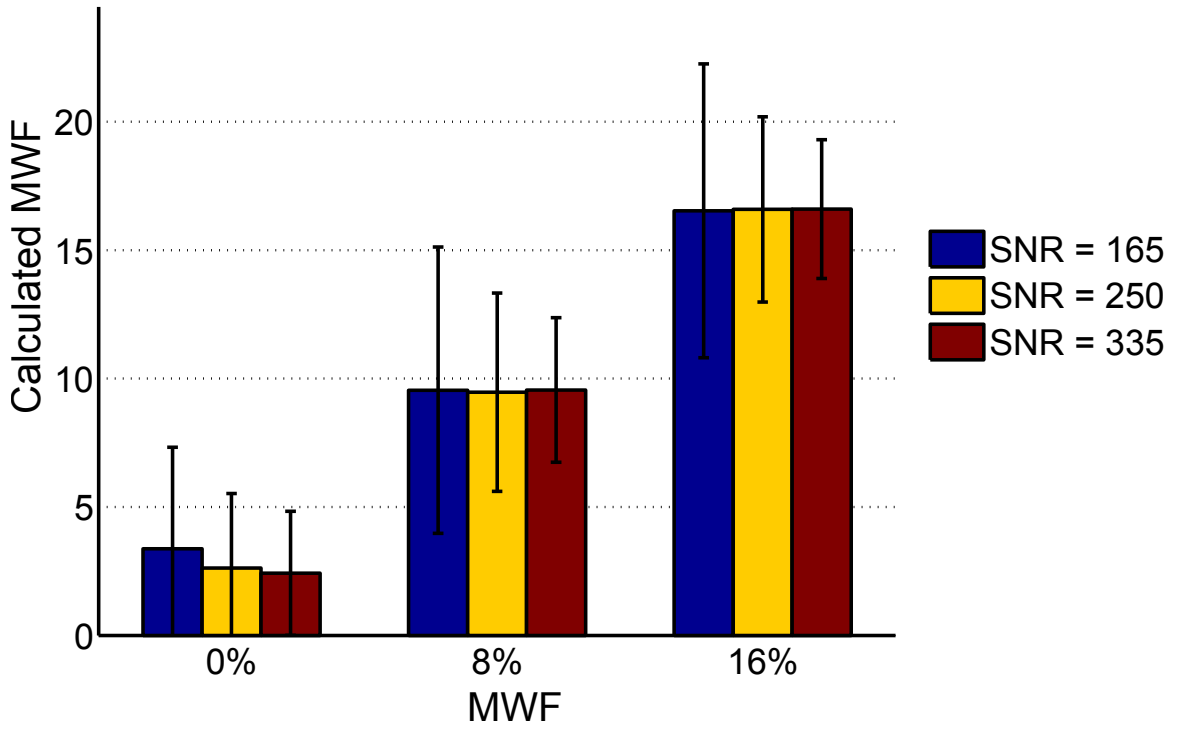


Fig. 3.16: Results of simulations with various SNR.

|                 | Simulation 1 | Simulation 2 | Simulation 3 |
|-----------------|--------------|--------------|--------------|
| $T2'$           | $\infty$     | 140          | 30           |
| SNR             | 250          | 250          | 250          |
| $TE_1$ (ms)     | 20           | 20           | 20           |
| $TE_2$ (ms)     | 60           | 60           | 60           |
| $\Delta t$ (ms) | 1.5          | 1.5          | 1.5          |
| $n_1$           | 4            | 4            | 4            |
| $n_2$           | 14           | 14           | 14           |

Table 3.5: Degree of static dephasing

### 3.5.5 Discussion

#### 3.5.5.1 Summary of results

The presented simulations demonstrate the ability of this acquisition scheme and simple model to evaluate the contribution of a short  $T2$  component and calculate

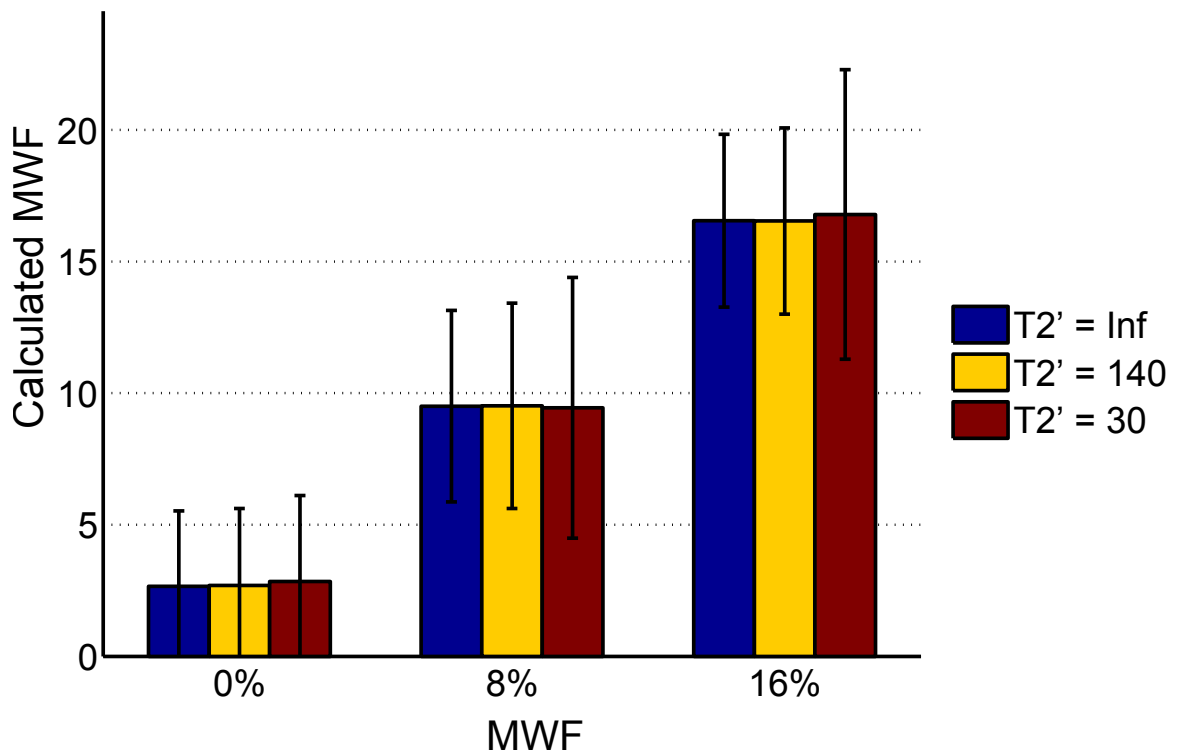


Fig. 3.17: Results of simulations with various static dephasing.

the MWF. The simulation parameters were chosen to emulate an implementation at 3T with realistic temporal SNR and data sampling based on gradient performance achievable on modern MRI scanners. The distribution of the calculated parameters were well behaved, increased in standard deviation in cases of lower SNR and/or greater static dephasing as expected but were subject to some bias to the starting estimates of the IRRLS.

### 3.5.5.2 Two-pool model

The presented model assumed bi-exponential T2 decay, consistent with a two-pool model of white matter. The first component is associated with myelin trapped within layers of the myelin sheath which exhibit a short T2, set at 30 ms in these simulations.



The second component consists of the intra- and extra- cellular water contributions which are inseparable *in-vivo* and set as 80 ms in these simulations. This model is appropriate in voxels where it can be assumed that there are no contributions from other T2 species, such as CSF. The signal contribution of each peak is modelled as a delta function, though a continuous distribution would have been more biologically appropriate. This is also the case with our objective function,  $s_{ratio}$ . It is unclear if assigning additional parameters to describe the form and width of a continuous distribution would aid in the evaluation of the MWF.

### 3.5.5.3 Influence of starting estimates

Decomposing a multi-exponential signal is an ill-posed problem, where small deviations of the decay curve due to noise can have a large impact on the fitted parameters. The objective function,  $s_{ratio}$ , is also subject to this effect. The choice of starting estimates affect the fitting algorithm's propensity to settle into a local minimum instead of reaching the globally optimal solution. This was seen in simulations with varying starting estimates, where this was reflected as a bias in the MWF estimates. However, the bias reported here appears less severe than that of the mcT2\* fitting reported by Hwang et al. ([132]) using their three component model.

### 3.5.5.4 *In-vivo* implementation and SNR

Though the simulations aimed to replicate the expected SNR and static dephasing, other sources of noise and imaging artefacts are not represented. These include artefacts caused by motion, eddy currents, truncation of k-space, the point-spread-function, and local frequency shifts [143]. Most other quantitative MRI methodologies are subject to these effects and their impact on the mcGESSE acquisition and analysis will have to be evaluated once implemented *in vivo*.

Establishing a preferred protocol given the number of acquisition parameters is not trivial. In large part, the bandwidth is constrained by the timing made possible at the first echo time ( $TE_1 = 20$  ms in these simulations). Bandwidth for  $TE_2$  were kept the same as  $TE_1$ . This means that a higher bandwidth, while allowing greater sampling at  $TE_1$ , would result in lower SNR of the  $TE_2$  data points which already suffer an SNR loss due to transverse relaxation. However, it was found through simulations that this trade-off resulted in very similar values for all three acquisition scenarios. The intermediate scenario, with 4 and 14 pairs of gradient echoes at  $TE_1$  and  $TE_2$  respectively, had a slightly lower standard deviation.

The pixel-wise analysis of an *in vivo* mcGESSE dataset will be subject to a wide SNR range due in large part to the sensitivity profile of the receiving head coil. The SNR values of the simulations were chosen to reflect this range. As expected, a lower SNR results in a wider distribution of the calculated MWF. In a typical MRI head coil, SNR is lower farther away from the coil elements (i.e. near the centre of the brain). This is a phenomenon which plagues all quantitative brain mapping techniques, though not always acknowledged explicitly.

Another significant factor in our SNR considerations is signal loss due to static dephasing ( $T2'$ ). As reported in the mcT2\* study,  $T2'$  effects result in shortening of the effective relaxation times,  $T2^*_{my}$  and  $T2^*_{ie}$ . This was blamed for the failure of MWF calculations using mcT2\* near sources of severe field inhomogeneities. The simulations of the present study show that, with the recovery of the signal caused by the spin echo, the calculation of the MWF remains possible in the case of both mild and severe  $T2^*$  shortening. Much like the results investigating intrinsic SNR, the negative effect of  $T2^*$  shortening resulted in a greater standard deviation of the MWF calculation.

A pulse sequence which could obtain a mcGESSE dataset on our lab's MRI hardware did not yet exist and needed to be programmed. These simulations have served as motivation for the implementation of mcGESSE which will however need to be assessed with regards to the imaging artefacts and other sources of noise which were not part of these simulations. This work follows in chapter 4, with the modification of a clinical spin echo sequence and the investigation of multiple protocols.

### 3.5.6 Conclusion

The feasibility of a new technique for whole-brain mapping of the MWF was demonstrated on theoretical grounds based on the gradient echo sampling of two spin echoes and a simple two-compartment model of white matter. The ability of this approach to estimate the MWF within a realistic SNR range and despite significant static dephasing motivates the future implementation of this technique *in vivo*.

## 3.6 Summary

Multiple T2 species are known to contribute to the T2 signal measured in white matter. Though water exchange occurs between these compartments, the rate of this exchange is considered to be slow relative to the relaxation times, such that they may be treated as distinct components to the total measured multi-exponential decay. Estimation of these components is not trivial when measurements are performed *in vivo* due to SNR considerations and the ill-posed nature of the data fitting.

Of particular interest is the shortest T2 component, attributed to water trapped within the sheath of the myelinated axon. The contribution of this component to the

total acquired signal is termed the MWF and has become the metric of interest of a group of MRI techniques aimed at myelin mapping. The earliest of these techniques, consisting of an optimized, single-slice, multi spin-echo acquisition, has been used to characterize both healthy and pathological white matter but may have seen limited clinical use due to limited coverage and long scan times. Alternative techniques are varied with some making modest improvements on the gold standard approach, utilizing alternative strategies to obtain T2 contrast or taking non spin-echo based approaches entirely.

One of these non-spin echo based approaches, mcT2\*, was investigated as a proof of concept study. The acquisition of a multi-gradient echo data allowed the decomposition of the signal and the detection of a short T2\* component, associated with white matter, using both NNLS and a two-compartment model. However, it was found that this approach was not suitable as a whole brain technique, as signal drop off due to sources of severe field inhomogeneities rendered MWF quantification impossible in those areas.

We proposed a novel approach, called mcGESSE, based on the symmetric gradient echo sampling of spin echoes and a two-compartment model of white matter. This approach takes advantage of symmetry inherent to the spin echo, such that the objective function becomes a ratio of the signal at equal time intervals before and after the spin echo instead of the native decay curve. This has the effect of simplifying noise considerations and ignoring the functional form of T2'. The feasibility of estimating the MWF based on a mcGESSE dataset was assessed using simulations based on realistic temporal SNR profiles. The effect of starting estimates, static dephasing, SNR and the sampling and bandwidth trade-off were assessed. The importance of the starting estimates was noted, based on the bias that it may introduce. The sampling/bandwidth trade-off had surprisingly little effect, while SNR and static de-

phasing affected the estimation of the MWF in an expected manner.

These simulations lay the foundations for the *in vivo* implementation of mcGESSE, presented in the next chapter, where additional factors will have to be considered, such as imaging artefacts not represented in these simulations.

# Chapter 4

## Myelin mapping of the human brain using mcGESSE

In chapter 3, mcGESSE was presented as a novel acquisition strategy, describing an MRI sequence based on the gradient echo sampling of two spin echoes combined with a two-component model to calculate the MWF. The feasibility of this approach was demonstrated using simulations with realistic temporal SNR expected at 3T. The current chapter reports on the implementation of mcGESSE for *in vivo* imaging based on the parameters gleaned from the simulations of chapter 3. Healthy participants underwent imaging to evaluate the clinical feasibility of mcGESSE, as well as the reproducibility of MWF measurements.

### 4.1 Introduction

*In vivo* MWF measurements are sensitive to changes in myelination and correlate with measures obtained using histology [121,144]. In addition to the qualitative correspondence between MWF maps and white matter lesions typically reported by mcT2 studies investigating MS [121,128,144–148], the MWF is expected to be sensitive to

subtle changes in myelin not detectable through typical radiological imaging [149]. Given previous findings of white matter abnormalities in autism combined with our own findings of increased white matter T2, MWF mapping offers the opportunity to investigate abnormalities of white matter microstructure with more specificity.

Magnetization transfer imaging and DTI are two other quantitative MRI techniques which can be used to assess the microstructure of white matter. However, the measures obtained with these techniques are not specific to myelin water content, though they may be influenced by it [96]. The magnetization transfer ratio (MTR), derived through magnetization transfer imaging, quantifies exchange between aqueous and non-aqueous protons, rendering it sensitive to inflammation and axonal loss. DTI is influenced by the macroscopic packing properties of white matter fibre bundles through the preferential direction of water diffusion, which is not specific to myelin water. While associations linking fractional anisotropy, the most commonly reported metric in DTI, to myelin content are common in the literature, such an interpretation may be ill-founded and exclude other factors [33]. The information obtained from MTR and DTI can thus be viewed as complementary to MWF measurements using mcT2 methods.

Limited coverage and long scan times are drawbacks that have limited the clinical application of mcT2 techniques and MWF mapping. These limitations are a result of the large number of spin echoes utilized to robustly characterize the multi-exponential decay curve. In chapter 3, it was shown that in the absence of spin echoes, the resulting T2\* decay was also multi-exponential and a short T2\* component associated with myelin water was detected with no *a priori* assumptions. However, in the presence of field inhomogeneities, such as those caused by air/tissue interfaces, signal decomposition no longer remains viable.

An alternative hybrid strategy, mcGESSE, was proposed, based on the symmetric gradient echo sampling of multiple spin echoes. This approach effectively combines the sampling density of gradient echoes with the signal viability afforded by spin echoes. A simulation study, presented in chapter 3, was conducted to show the feasibility of this technique with an eye to the *in vivo* implementation of mcGESSE at 3T within a clinically feasible scan time.

MRI scanners operating at a field strength of 3T are becoming more common in both clinical and research settings. We expect our future research protocols to be implemented at this field strength, reflected by our choice of parameters in the simulation study of chapter 3. The bulk of mcT2 studies to date have been conducted at 1.5T, though more recent studies have also moved to 3T, including implementation of the gold standard MESE<sub>ss</sub> [119]. 3T poses additional challenges, including increased B<sub>1</sub> inhomogeneity and susceptibility effects.

Experiments using imaging phantoms are often used where possible to evaluate the performance of new imaging techniques. For MWF mapping, a convenient substance exhibiting bi-exponential decay with T2 times in the range of what would be expected in white matter is dairy cream [150]. Dairy cream is relatively cheap and readily available. The short T2 component in dairy cream originates from fat such that the range of fat percentages available are a convenient and reliable way of simulating a range of MWF values. However, the protons bound to fat molecules have a different resonance frequency than water. While it would be possible to sample the fat and water in phase, it would severely limit the gradient sampling scheme possible with mcGESSE. For this reason, healthy volunteers were preferred and imaging phantoms saw limited use in preliminary pulse sequence development.

The purpose of this study was to implement mcGESSE *in vivo* on our lab's



Siemens Verio 3T scanner and establish a protocol with optimal brain coverage within a clinically relevant scan time. Further, MWF mapping and reproducibility of MWF measurements in healthy volunteers were evaluated, as well as the potential of accelerated protocols.

## 4.2 Methods

### 4.2.1 Pulse sequence development and MR data acquisition

Implementation of the mcGESSE sequence on our lab’s scanner was accomplished by modifying a clinical multi-contrast spin echo sequence. Gradient readout elements were added, symmetrically placed about the spin echo time. Bipolar gradient readouts were used, with pairs of readouts limited to even numbers such that corresponding pairs used for the calculation of  $s_{ratio}$  were of the same polarity. Gradient readout also occurred at the spin echo time. Each spin echo was sampled within its own acquisition (one spin echo per repetition) to allow for straightforward slice interleaving.

The slew-rate values of imaging gradients were not set to the maximum values possible with the scanner’s gradient hardware, but were instead left at default values ( $<100$  mT/m/ms). This was to avoid the possibility of slew-rate induced eddy currents, which were held responsible for some stimulated echo artifacts in the implementation of MESE<sub>ss</sub>. This constraint influenced the decision to use alternating gradient readout polarities as well as the intermediate inter-echo spacing of  $1500 \mu\text{s}$  of the simulation study.

The two spin echo times were chosen to be slightly shorter than those used for the simulations. The first spin echo was set at 19 ms (vs. 20 ms in the simulations)

as this was the shortest value possible for 4 gradient echo pairs with the default slew rate and a bandwidth of 965 Hz/pixel. The second spin echo time was shortened to 52 ms (from 60 ms in the simulations) which benefited the image quality of the last few gradient echoes. Table 4.1 lists the parameters of the mcGESSE acquisition.

|                               |             |
|-------------------------------|-------------|
| in-plane resolution (mm x mm) | 1.15 x 1.15 |
| slice thickness (mm)          | 2.5         |
| TR(ms)                        | 2500        |
| TE <sub>1</sub> (ms)          | 19          |
| TE <sub>2</sub> (ms)          | 52          |
| $\Delta t$ (ms)               | 1.5         |
| n <sub>1</sub>                | 4           |
| n <sub>2</sub>                | 14          |
| acquisition time (min:sec)    | 16:30       |
| bandwidth (Hz/px)             | 965         |

Table 4.1: mcGESSE acquisition parameters

A 32-element phased-array receive-only conformal head coil was used for all imaging without enabling the available pre-scan normalization. The effects of normalization, used to correct for signal heterogeneity across the imaging volume, are likely to depend on many factors, such as the imaging sequence being used, the manufacturer’s implementation, and the ensuing data post-processing [151]. The head coil used is noted to have a significant SNR advantage, particularly near the periphery of the cerebrum [152]. Further, the phased-array head coil enabled the use of an accelerated protocol using parallel imaging. To evaluate the feasibility of an accelerated protocol, 3 participants underwent a third scan, acquired immediately after the second full mcGESSE dataset without repositioning of the subject or slice locations, using an acceleration factor of 2.

In-plane resolution and slice thickness were maintained for each scan while the number of slices and phase encoding steps were set to the minimum number required

for maximal brain coverage according to each participant’s anatomy and ranged from 38 to 44 slices and 160 to 186 phase encoding steps (table 4.1). The FOV in the phase encode direction was adjusted so that the in-plane resolution was the same for all scans.

### 4.2.2 Subjects

Healthy volunteers were recruited under our research institution’s sequence development ethics approval. Seven participants (6 males and 1 female) aged 23 to 56 underwent imaging, with 6 being imaged twice within an hour after exiting the scanner room for a brief interval. Three volunteers underwent imaging a third time with an accelerated protocol using parallel imaging. All subjects provided written consent.

### 4.2.3 mcGESSE data analysis

Reconstructed images in DICOM format were exported for off-line processing in Matlab (Mathworks, Wisconsin). Images were first filtered using a gaussian kernel spanning 5 pixels with a standard deviation of 0.8 pixel, chosen to filter out some of the signal misregistration of images acquired with opposite gradient polarities while still preserving acceptable contrast at edge boundaries. The use of an anisotropic diffusion filter (ADF) as used in chapter 3 has been shown to improve MWF measurements using the  $MESE_{ss}$  [141] and MEGE [132]. While it did improve the quality of MWF maps using mcGESSE, it did not outperform the gaussian filtering described above.

Images were automatically masked, based on a signal intensity threshold of 250 applied to the  $TE_2 = 52$  ms spin echo image such that no computations were performed on voxels which did not meet this threshold. On the remaining voxels,  $s_{ratio}$ ,

was calculated from the series of images and the data was fit using IRRLS as used in the simulation study of chapter 3 and further described in Appendix II. Due to the wide range in SNR expected with the 32-element phased-array head coil, the fitting tolerance of the IRRLS algorithm was dynamically adjusted to the voxel's SNR according to basic error propagation theory. Additionally, to remove bias due to the starting estimates, starting points were randomly seeded 10 times and the trimmed mean was taken of all 10 resulting IRRLS fits. Residuals of each fit were also mapped, whereas points with residuals greater than 0.5 were abandoned early for computational efficiency on the basis of that they clearly did not fit the model.

In this way, MWF and residual maps were calculated for each dataset. Computations were done using the Shared Hierarchical Academic Research Computing Network (SHARCNET). Using 8 AMD Opteron 2.2 GHz cpus, computation of a complete mcGESSE dataset took between 6 to 9 hours.

#### **4.2.4 Image normalization and segmentation**

Image registration was used to normalize all MWF maps to a standard stereotactic space, which approximates Talairach space. A T2-weighted template (ICBM-152, Montreal Neurological Institute) was used in conjunction with each subject's T2-weighted image (obtained from the spin echo image at  $TE_2$ ) in the image registration routine offered in SPM8 (Wellcome Trust Centre for Neuroimaging; University College London, London, United Kingdom) [153]. A set of parameters describing these transformation into stereotactic space was then applied to the MWF map in order to register it to standard space.

Also using SPM8, white matter and grey matter probability maps were constructed for each subject in standard space and were converted to binary masks using

a threshold value of 0.90, as we had done in previous studies (chapter 2).

### 4.2.5 Creation of ROI

Masks for each ROI were created using either the PickAtlas toolbox for Matlab (Wake Forest University) [79] or the LONI white matter parcellation map (WMPM; Laboratory of Neuroimaging, University of California, Los Angeles) based on the DTI-81 brain atlas [81]. These masks are three-dimensional binary volumes representing the location of each ROI in standard space. These ROIs are then combined with the subject specific white and/or grey matter masks. The resulting subject specific mask was additionally masked with the respective residual map, where, based on inspection, values above 0.03 were considered poor fits and not included in the calculations. Table 4.2 provides a summary of ROI creation.

| ROI                         | source atlas | tissue mask         |
|-----------------------------|--------------|---------------------|
| cingulate gyrus             | LONI WMPM    | GM + WM             |
| putamen                     | PickAtlas    | GM + WM             |
| caudate                     | PickAtlas    | GM + WM             |
| thalamus                    | PickAtlas    | GM + WM             |
| cerebral grey matter        | Pick Atlas   | GM - corona radiata |
| cerebral white matter       | Pick Atlas   | WM - corona radiata |
| corona radiata              | LONI WMPM    | WM                  |
| genu of corpus callosum     | LONI WMPM    | WM                  |
| splenium of corpus callosum | LONI WMPM    | WM                  |
| body of corpus callosum     | LONI WMPM    | WM                  |
| internal capsule            | LONI WMPM    | WM                  |

Table 4.2: Details of ROIs used.

### 4.2.6 Statistical analysis

Group mean MWF values for each ROI were obtained by averaging the means obtained for each subject. To visualize within-subject inter-scan reproducibility, scatter plots were produced of the mean MWF values obtained from both scans across relevant ROIs. The parameters of a linear regression were calculated, as well as the coefficient of determination. To test for significant differences, the MWF distributions for each ROI were compared using a two-sample Kolmogorov-Smirnov (KS) test. The accelerated protocol was similarly compared to the non accelerated acquisition with scatter plots, linear regression and two-sample KS tests. The Bonferroni corrected p-value for significance for all KS-tests was set at  $p < 0.00625$ .

## 4.3 Results

MWF maps, in native space are shown in figure 4.1, along with the corresponding residual maps and T2-weighted images. Regions where the two-pool model is inappropriate are highlighted by the high residual values, particularly in voxels containing CSF and non-brain tissue within the perimeter of the skull. Partial volume effects involving these tissues are responsible for some of the spurious MWF values seen at the periphery of brain tissue. Regions of extreme magnetic field inhomogeneity, particularly near the lateral temporal lobe, are also subject to spuriously elevated MWF values.

Group mean MWF values were calculated from each subject's first scan, except for one subject, where the second scan was used as the first scan was discarded due to excessive motion (and was thus not included in the comparisons of within subject inter-scan reproducibility). Deep grey matter structures were also found to have

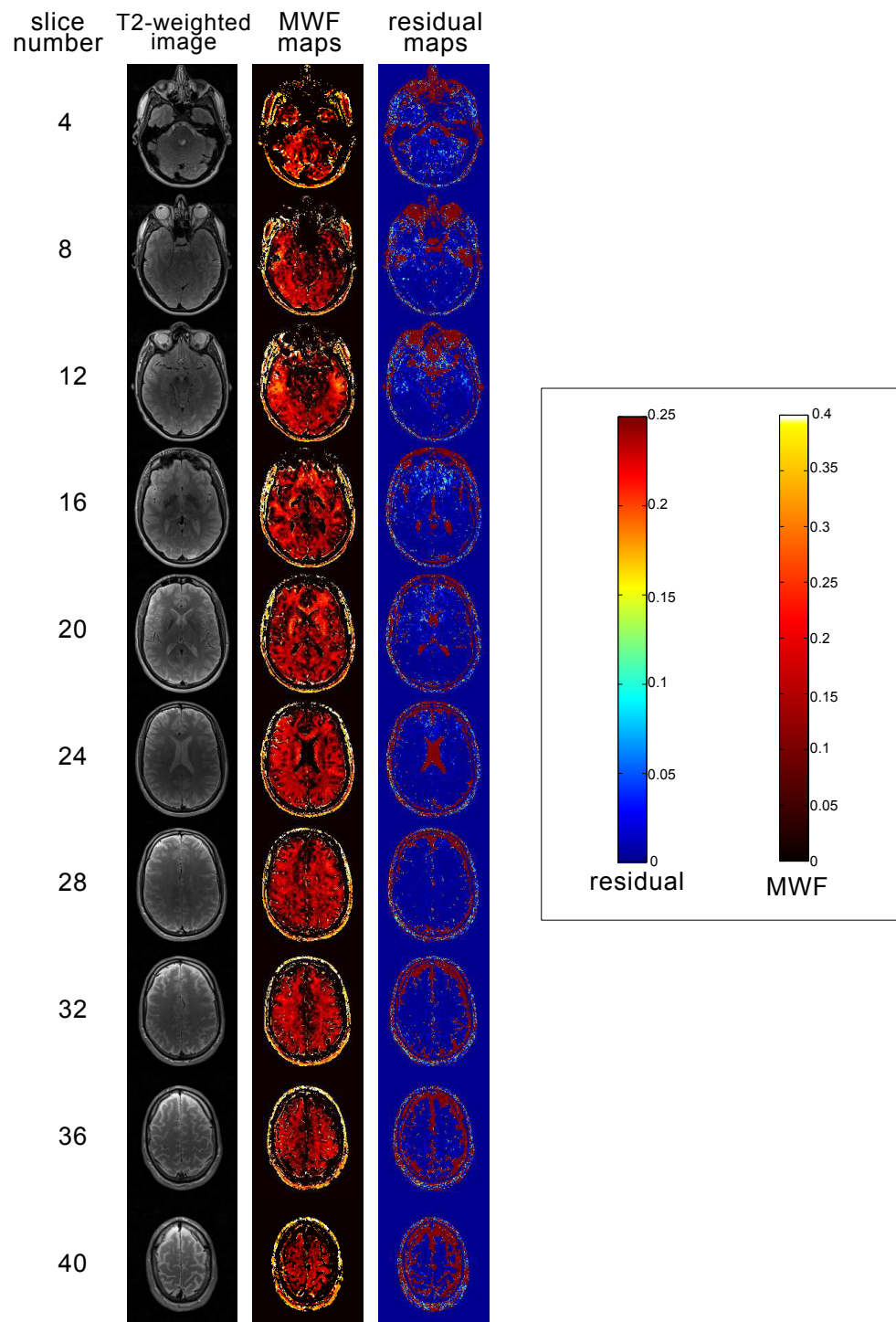


Fig. 4.1: T2-weighted images, MWF maps and residual maps of every fourth slice of a subject's whole-brain dataset obtained with mcGESSE

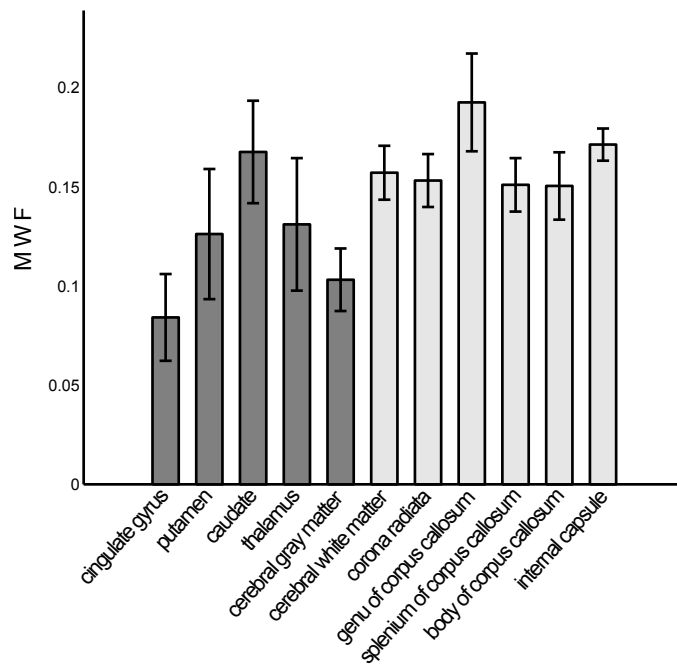


Fig. 4.2: Mean MWF values and standard deviations for grey and white matter ROIs. Deep grey matter structures (i.e. putamen, caudate and thalamus) were excluded from further analyses.

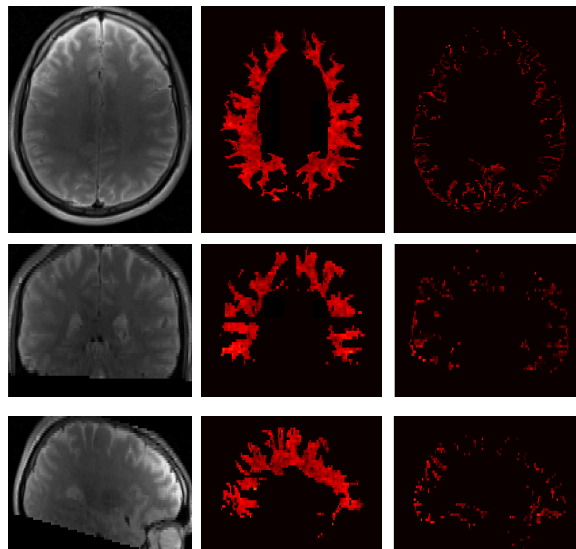


Fig. 4.3: Normalized T2-weighted images, shown in all three orientations, with corresponding masked MWF maps of white (middle) and grey (right) matter.



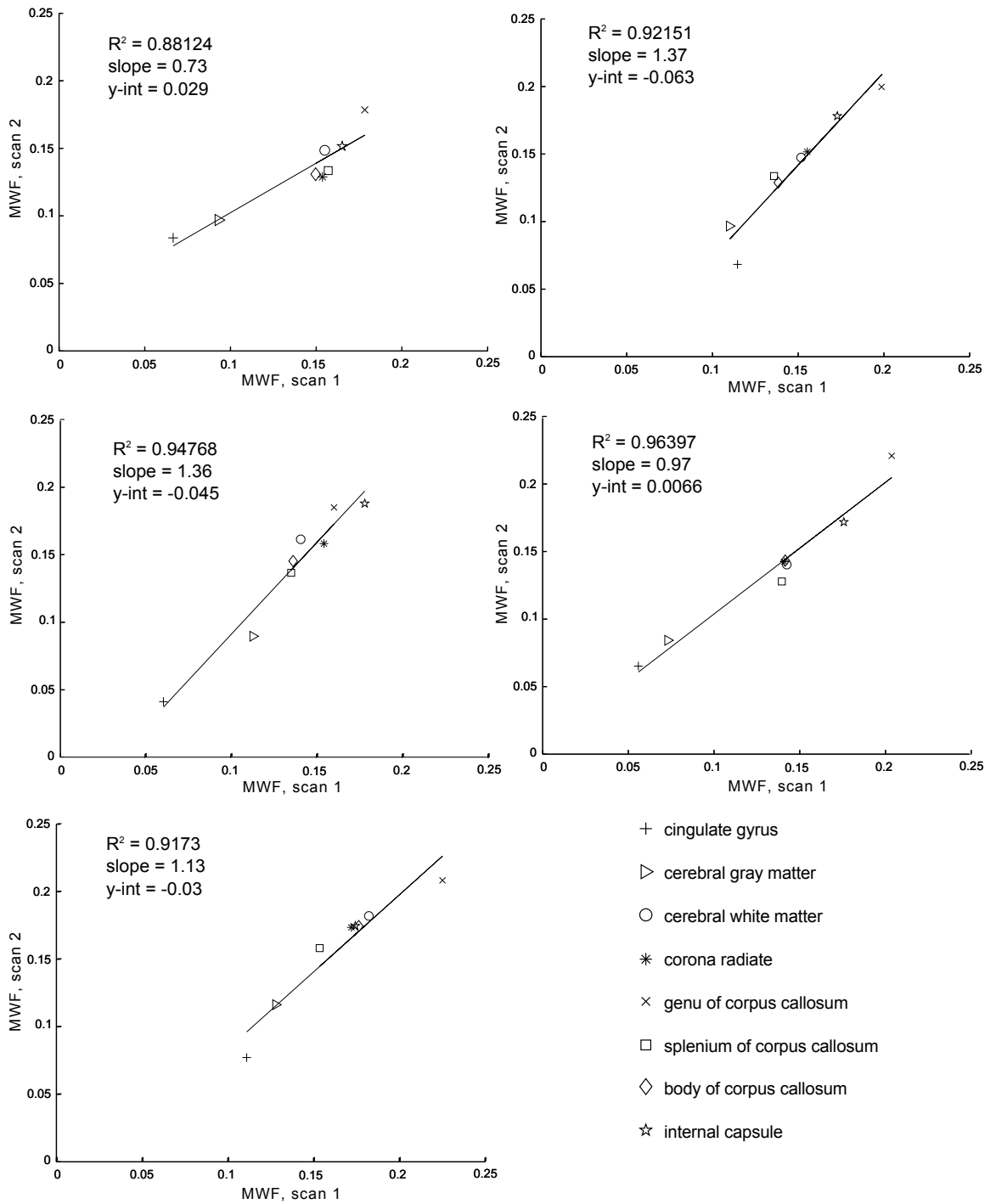


Fig. 4.4: Scatterplots and linear regression parameters of within subject inter-scan reproducibility. Each scatterplot represents data from a single subject.

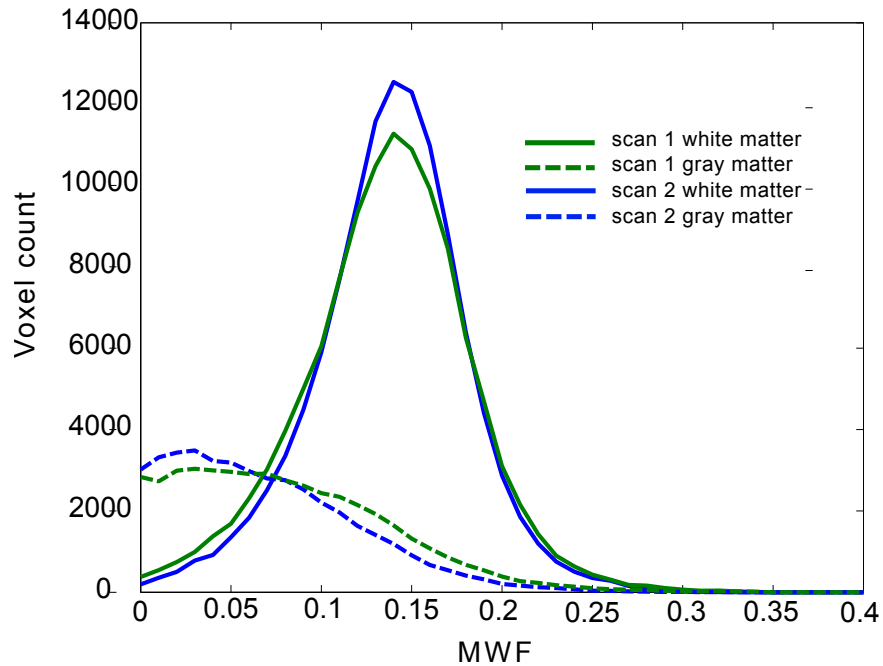


Fig. 4.5: Histograms depicting the MWF distributions in grey and white matter calculated from two scans from the same subject.

unexpectedly high MWF values, with high variability within the group. As such, the putamen, thalamus and caudate ROIs were not included in further comparisons beyond the report of group means shown in figure 4.2.

Masked grey matter and white matter MWF maps are shown, in standard space in figure 4.3. The MWF distributions corresponding to these two ROIs are shown in figure 4.5 for both scans. Scatterplots for each subject include the slope, y-intercept and coefficient of determination calculated from the linear regression. However, statistical tests were done on the distribution of MWF values (such as those shown in figure 4.5). No ROIs within any of the participants had significantly different MWF distributions between the two scans (see table 4.3).

Similarly, scatterplots in figure 4.6 show the mean MWF values and associated regressions comparing the accelerated acquisition to the full acquisition within the

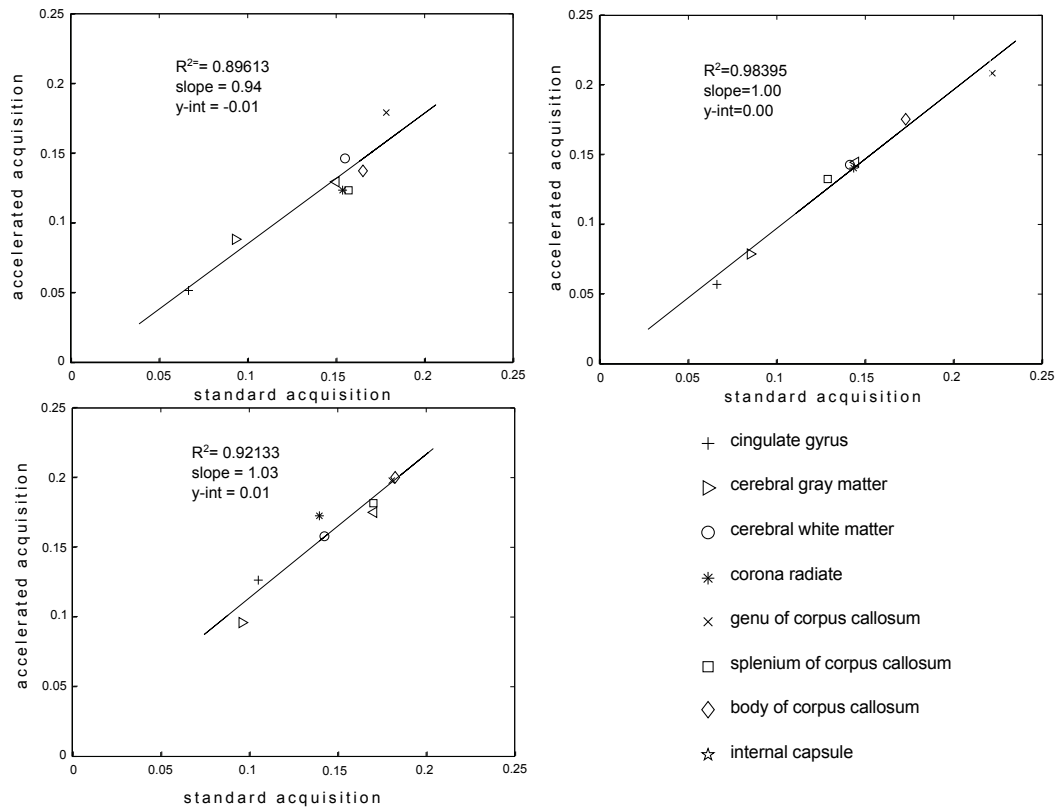


Fig. 4.6: Scatterplots and linear regression parameters comparing the accelerated protocol using parallel imaging against the unaccelerated protocol.

| ROI | subject 1 | subject 2 | subject 3 | subject 4 | subject 5 |
|-----|-----------|-----------|-----------|-----------|-----------|
| CG  | 0.9016    | 0.9855    | 0.2436    | 0.9016    | 0.0864    |
| CGM | 0.0864    | 0.2436    | 0.9855*   | 0.7382    | 0.9855*   |
| CWM | 0.9855    | 0.9016    | 0.9998    | 0.9855    | 0.9998    |
| CR  | 0.9016    | 0.9998    | 0.9855    | 0.9855    | 0.9998    |
| GCC | 0.9016    | 0.9855    | 0.2436    | 0.9016    | 0.7382    |
| SCC | 0.7382    | 0.9855    | 0.9998    | 1         | 0.548     |
| BCC | 0.548     | 0.9855    | 1         | 0.548     | 0.3769    |
| IC  | 0.9855    | 0.9016    | 0.9016    | 0.7382    | 0.9855    |

Table 4.3: P-values as calculated by two tailed KS-test for scan-rescan data. \* indicates the p-value of the normalized distributions after the unnormalized distribution met significance. CG; cingulate gyrus. CGM; cerebral white matter. CWM; cerebral white matter. CR; corona radiata. GCC; corpus of callus callosum. SCC; splenium of corpus callosum. BCC; body of corpus callosum. IC; internal capsule.

same scan. No significant differences were found between any of ROIs within any of these subjects (see table 4.4).

## 4.4 Discussion

The work presented in this chapter follows up on the simulation study of chapter 3 by implementing mcGESSE as a new MWF mapping approach on our lab's 3T MRI scanner. Healthy volunteers participated in this study, with the majority undergoing imaging twice and some a third time with an accelerated protocol using parallel imaging. The resulting data showed MWF values consistent with most other reports, particularly at 3T, in the majority of brain regions investigated. Additionally, good within-subject inter-scan reproducibility was shown, for scans acquired in two separate imaging sessions as well as the accelerated protocol acquired in the same imaging session as the standard scan.

| ROI | subject 1 | subject 2 | subject 3 |
|-----|-----------|-----------|-----------|
| CG  | 0.9016    | 0.9855    | 0.2436    |
| CGM | 0.9855    | 0.7382    | 0.2436    |
| CWM | 0.9855    | 0.9998    | 0.9998    |
| CR  | 0.9016    | 1         | 0.9855    |
| GCC | 0.3769    | 0.9855    | 0.3769    |
| SCC | 0.9016    | 0.9855    | 0.3769    |
| BCC | 0.7382    | 0.548     | 0.3769    |
| IC  | 0.548     | 0.9016    | 0.9016    |

Table 4.4: P-values as calculated by two tailed KS-test for standard acquisition compared to the accelerated acquisition. CG; cingulate gyrus. CGM; cerebral white matter. CWM; cerebral white matter. CR; corona radiata. GCC; corpus of callus callosum. SCC; splenium of corpus callosum. BCC; body of corpus callosum. IC; internal capsule.

#### 4.4.1 Relevance of previous simulations study

The simulations of chapter 3 allowed us to evaluate the effects of intrinsic SNR, acquisition bandwidth, T2\* dephasing and starting estimates of the IRRLS on the MWF calculations in a straightforward manner. A first important consideration borne out by the results of these simulations is the relative insensitivity of the trade-off made between receiver bandwidth and the number of sampling points. From the simulations, it appears that the SNR gain of an acquisition with lower bandwidth would compensate for the reduced number of sampling points. In practice, this trade-off would lower the potential for eddy currents with less sampled points, as gradient switching speeds would not have to be maximized. However, a lower bandwidth also necessitates a longer readout, which introduces additional weighting due to T2\* decay during the readout, known as the point-spread-function, which would result in some degree of blurring. While an exhaustive quantitative evaluation of these parameters fell outside the scope of this study, a middle of the road approach was taken by setting gradient switching speeds to their default values and lowering the bandwidth to near its minimum for the given number of data points, as constrained by the first spin echo time, TE<sub>1</sub>. While the gradient echoes along the second spin echo envelope could have

been acquired with a different bandwidth, it was kept consistent to avoid introducing any additional effects due to differences in the point-spread-function. Whether any gains in data quality could be obtained by further optimizing the sampling bandwidth trade-off could be the focus of future work.

A second important factor highlighted by the results of the simulations is the effect of the starting estimates of the IRRLS. This reflects the ill-posed nature of the signal decomposition. Even though  $s_{ratio}$  qualitatively appears to more easily resolve the contribution of  $T2_{short}$ , a least squares based minimization is still susceptible to settle on a local minimum. This is further exacerbated by the wide range of SNR encountered across the brain, where a mismatch of the fitting tolerances of the IRRLS and the SNR at a specific voxel can increase the likelihood of settling at a local minimum. Thus, the analysis of the *in vivo* data benefited from two additional steps: first, the fitting tolerance of the IRRLS was dynamically adjusted, on voxel by voxel basis, via its SNR and error propagation. Secondly, the starting estimates were randomly seeded 10 times and the trimmed mean (where the lower and upper 10% of values are truncated) of all IRRLS fits taken as the result. Preliminary analyses showed that no improvements were obtained beyond this number of randomly seeded fits.

#### 4.4.2 Filtering

In regions of significant field inhomogeneity, the alternating polarity of the readout gradient causes slight signal misregistration in its direction. This is seen in the images as a slight geometric warping, alternating from gradient echo to gradient echo. A gaussian filter was applied to all images, with a standard deviation of 0.8 voxels, which was enough to average this misregistration while retaining the image detail relevant to MWF mapping. The quality of MWF maps were improved in these regions. In contrast, the edge preserving ADF was also evaluated and, while showing

improvements when compared to no filtering, did not increase the quality of the MWF maps to the same degree as gaussian filtering. This does not necessarily contradict the findings of Jones et al. [141], as the analysis methods used are vastly different.

### 4.4.3 Field inhomogeneities

The symmetry inherent to mcGESSE has greatly simplified our treatment of macroscopic field inhomogeneities on the signal decay. We recall that the sources of signal loss, classically described by the time constant  $T2'$ , are reversed and recovered by the spin echo. While the extent of the presence of field inhomogeneities was reflected through the temporal SNR of the signal in the simulations, the situation can become more complicated *in vivo*. In particular, distortions in the magnetic field will result in off-resonance of the nuclei and unintended phase variations, leading to both sub-optimal excitation and signal misregistration.

In whole-brain MRI acquisitions using gradient echo based techniques, the temporal lobes are cited as one of the most severely affected regions, due to the presence of both air/tissue and bone/tissue interfaces [154, 155]. This is also the case for mcGESSE images, where this region is subject to both signal loss, geometric distortions and off-resonance effects. These artifacts, spread across the entire time-series of images making up the mcGESSE dataset, result in the calculation of spurious MWF values.

There are many methods proposed to correct signal loss due to the large field inhomogeneities typically encountered in these regions. The problem has been approached from both the acquisition side, with the optimization of acquisition parameters, such as quadratic RF pulses [156–163], or by correction of the data prospectively, with or without the collection of additional images [164–172]. Since mcGESSE consists of

a large set of closely spaced images weighted by  $T2^*$  and  $T2'$ , it would be straightforward to estimate the magnitude of the magnetic field disturbances. Additionally, most scanners allow the simultaneous acquisition of phase images, which may allow corrections based on phase gradient mapping [173,174]. However, to date, no methods have been proposed which explicitly account for multi-exponential relaxation. This work sets a framework in which such corrections could be developed.

The putamen, thalamus and caudate are deep grey matter structures for which the calculated mean MWF were higher than expected when compared to the other brain regions assessed as well as the literature. While MWF values obtained at 3T have generally been reported to be higher than those obtained at 1.5T [119,127], we suspect the values in the range we observed to be erroneous or at least the result of a significant bias. Possible reasons include the lower SNR experienced in these brain regions, and/or the presence of significant iron stores. While mesoscopic and macroscopic field inhomogeneities are reversed by the spin echo, and described by  $T2'$ , microscopic field inhomogeneities (smaller than the diffusion length and orders of magnitudes smaller than the voxel) would be reflected in the  $T2$  time(s) of the voxel [166,175,176]. Referred to as intra-voxel dephasing, this mechanism could appreciably shorten  $T2_{long}$  which would not only lower its temporal SNR, but may interfere with the boundary conditions of the fit using IRRLS. While this is an issue worthy of further consideration, MWF measurement in deep grey matter structures is not a necessity to test the implication of myelin in the context of the under-connectivity hypothesis in autism.

#### **4.4.4 Image segmentation and normalization**

Partial volume effects refer to the presence of multiple tissue types within an imaging voxel. In the context of this work, we are concerned with voxels which are not uniquely comprised of white matter only, or grey matter only. The concern is to



maintain the applicability of the two-pool model used in the calculation of the MWF. The segmentation of images using white matter and grey matter probability maps combined with a high threshold allows us to easily and automatically exclude regions where partial volume effects may be a concern. In this way, we avoid contaminating MWF measurements with erroneous values. The result of this segmentation is seen in cerebral grey matter and white matter in figure 4.3. The reproducibility of the MWF distributions are shown in figure 4.5 for the same patient, but in two separate scans, which effectively also demonstrates the reproducibility of the segmentation routine.

Image normalization and the creation of ROIs in standard space is another aspect of the methods used in this study for which reproducibility is inherently evaluated. In this respect, it is interesting to compare the scatterplots of the inter-session scans of figure 4.4, to the scans of figure obtained without subject repositioning (figure 4.6). While the sample size is small it remains readily apparent that subject repositioning is a considerable source of inter-scan variability. However, the source of variability is not uniquely due to the small differences in orientation and slice position which must be handled during normalization. A second important source is the quality of the  $B_0$  shim, which may vary if subtle changes in position are more favourable to a good shim, or if the automated shimming routine converges to a different solution.

#### **4.4.5 MWF distributions**

The MWF values obtained within an ROI, or the entire brain are expected to belong to a distribution that is not only due to measurement error, but also a reflection of the microstructural heterogeneity of myelin which may span the ROI. As seen in figure 4.5, white and grey matter exhibit markedly different distributions. The KS tests comparing ROIs were performed on the distributions make no assumption as to the form of this distribution, requiring only that they be continuous, an appro-

appropriate assumption given the large number of voxels included in each ROI. In two subjects, the MWF of cerebral grey matter would have been found to be significantly different using a non-Bonferroni corrected p-value of 0.05. Inspection of the subject data revealed that the total number of voxels assigned to grey matter, as per the segmentation, was vastly different between each subject's two scans. As such, the distributions were normalized and KS-tests repeated, at which point all significant differences (at  $p < 0.05$ ) vanished. We suspect that differences in segmentation of cortical grey matter are responsible.

MWF values obtained using the gold standard  $\text{MESE}_{ss}$  at 1.5T and methods closely derived from it have generally been consistent. However, more recent comparisons of the same methods at 1.5T and 3T (including  $\text{MESE}_{ss}$ ) [119] [127] have found MWF values to be generally increased at a higher field strength. In the case of  $\text{MESE}_{ss}$ , significant differences were found at 3T depending on whether a transmit/receive or receive-only head coil was used. MWF values obtained are likely further influenced by differences in the fitting of data, ROI definition and the implementation of automated normalization and segmentation techniques. Therefore, it is difficult to draw direct comparisons between the mcGESSE data presented in this chapter and data from previous mcT2 studies. However the MWF values we report here are well within the range found in the literature in white matter, though seem elevated for grey matter. If we exclude deep grey matter on the basis of high iron concentrations as discussed previously, elevated MWF values in grey matter may be explained by the bias of IRRLS reported in the simulation studies for small values. Once more studies using the gold standard and alternative techniques are conducted at 3T, or by conducting our own comparison study, a clearer picture of this systematic over estimation in grey matter should be obtained.

#### **4.4.6 High-field imaging of white matter**

Relaxation signal properties of white matter have been investigated at field strengths beyond 3T. MWF mapping in fixed brain specimens at 7T showed further correspondence with histological staining [177]. However, field inhomogeneity effects are generally further increased at this field strength. The signal dependence on the white matter fibre orientation relative to  $B_0$  has been of particular interest, implicating myelin as the principal source of this effect. This has been modelled [178], and exploited in terms of  $T2^*$  mapping [179, 180] and frequency shifts [181]. This is an ongoing area of study, which may benefit the interpretation of measurements at lower field strengths, including mcGESSE.

#### **4.4.7 Accelerated protocol using parallel imaging**

The potential of an accelerated protocol using parallel imaging was evaluated. Using an acceleration factor of 2, the acquisition time is nearly halved. For clinical studies, shorter acquisitions may significantly increase the odds of a successful scan in uncooperative subjects. The scatterplots and regressions of figure 4.6 indicate good reproducibility of mean MWF measurements of the ROIs assessed. More subjects should be scanned with both protocols to establish the suitability for clinical studies, though these preliminary results look promising.

#### **4.4.8 Future work**

Though mcGESSE was proposed as a whole-brain MWF mapping technique, the current work highlights limitations in some brain regions. Future work, before using mcGESSE for clinical studies, should investigate how some of these limitations can be addressed. For example, in deep grey matter, where intra-voxel dephasing may be re-

sponsible for biased MWF calculations, changes in resolution or boundary conditions of the two-pool model may help. The overestimation seen in cerebral grey matter, though expected, could be alleviated using modifications to the fitting routine, such as fitting to a one-pool model and using an F-test to see if the additional parameters of the two-pool model are warranted. Extreme field inhomogeneities, typically seen near the temporal lobes are another factor influencing data quality. This issue is certainly not specific to mcGESSE and suitable methods, which could take advantage of the large amount of multi-echo magnitude and phase data collected while not clouding the multi-exponential signal decay, should be evaluated.

## 4.5 Conclusion

This chapter demonstrated the feasibility of MWF mapping using mcGESSE *in vivo* at 3T. Though data quality in certain brain regions should be the subject of further evaluation, the reproducibility of cerebral MWF measurements was demonstrated in healthy volunteers. Obtaining whole-cerebrum white matter MWF measurements would be invaluable in specifying our previously reported T2 abnormalities and ultimately testing the under-connectivity hypothesis. Additionally, the potential of an accelerated protocol using parallel imaging was shown, and is especially relevant to the implementation of this protocol in studies including pediatric populations.

# Chapter 5

## Conclusions and summary

This final chapter provides a concise summary of all five studies presented in this thesis. Exploiting the sensitivity of quantitative T2 to changes in brain tissue microstructure, prevailing hypotheses are tested in pediatric populations of patients with autism and TS. The unfavourable lack of specificity of quantitative T2 imaging limits the conclusions that can be drawn from those studies. However, the compartmentalization of water in white matter has motivated techniques which exploit multi-exponential T2 decay, with many focussing on quantifying the MWF as a marker of myelin content. Currently available techniques were reviewed, and a technique based on multi-exponential T2\* decay (mcT2\*), which at the time had not yet been implemented *in-vivo*, was evaluated as proof of concept study. The analyses presented raise some concerns with regards to the suitability of mcT2\* as a whole-brain technique and is not pursued further. McGESSE was proposed as a novel acquisition strategy, which effectively combines the SNR advantage afforded by a spin echo with the sampling density of gradient echoes. We presented data obtained from a simulation study, showing the feasibility of this technique at 3T. The *in-vivo* implementation of mcGESSE followed, and healthy participants were recruited for imaging to assess its ability for whole-brain MWF mapping and the reproducibility of MWF measurements within ROIs.

## 5.1 T2 abnormalities in autism

Evidence of brain abnormalities in autism have been reported in many imaging studies. An altered brain development trajectory has been proposed and reconciles some of the conflicting differences in these findings. White matter, principally distinguished from grey matter by the presence of myelin, has been implicated by reports of volume abnormalities, among other imaging findings. Taken together with the profile of affected and spared functions in autism, imaging findings provide support for the under-connectivity hypothesis.

T2 imaging capitalizes on the sensitivity of the acquired signal to the microstructural environment of the hydrogen nuclei giving rise to a detectable MRI signal. A previous study from our lab was the first to report on whole cerebrum T2 in autism [67], finding increased T2 in white matter but no significant differences in grey matter. Following up on these findings, with an eye to some notable volumetric WM findings, chapter 2 presented a novel automated approach to the localization of these T2 abnormalities. A first scheme parcellated WM into their anatomically lobar compartments, finding increased T2 in the frontal and parietal WM. A second scheme, chosen for its relevance to the developmental course of WM maturation, compared bridging, sagittal and radiate white matter compartments. In this case, T2 was seen to be increased in bridging and radiate white matter.

These findings are in agreement with many previous findings of volumetric abnormalities, as well as many emerging findings using metrics obtained through DTI. Despite some limitations imposed by the study sample and data acquisition and analysis, the results lend further evidence to pathophysiological differences in white matter

microstructure relevant to the concept of aberrant neural connectivity in autism.

## 5.2 T2 abnormalities in Tourette syndrome

Implication of the CSTC network in TS has provided a common framework to reconcile symptomatology and imaging findings. Volumetric abnormalities are part of the evidence implicating components of the CSTC circuitry, along with a single T2 study in adults.

As such, we presented the first study quantitatively evaluating T2 relaxation times of CSTC components in a group of children and adolescents with TS. Utilizing similar ROI-based methodology, we reported localized increased T2 of the caudate nucleus within the basal ganglia. This suggests microstructural differences of subcortical grey matter tissue, consistent with other brain imaging studies of TS and relevant to aberrant CSTC circuit function.

## 5.3 Feasibility of mcT2\* *in vivo* for myelin mapping

Motivated by the WM T2 abnormalities presented in chapter 2, we reviewed a group of specialized techniques which seek to better characterize the T2 distribution with the aim of calculating the contribution of a short T2 component attributed to water trapped between layers of the myelin sheath, the MWF. One of these techniques, mcT2\*, is based on the decomposition of the T2\* decay, obtained with a gradient echo sequence and foregoes most of the limitations of the spin echo approach with regards to brain coverage and scan time. At the time, this method had only been

implemented *ex-vivo*, in a fixed brain not subject to the signal loss associated with magnetic field inhomogeneities caused by air-tissue interfaces such as the frontal sinuses.

mcT2\* was implemented *in-vivo* at 3T using a gradient echo sequence and compared to a rudimentary implementation of mcT2 using a clinical spin echo sequence. Imaging data from a single volunteer were analyzed using both the NNLS algorithm and a two-component model representing the bi-exponential decay of voxels containing myelin water and intra/extra cellular water. It was found that while the MWF maps obtained from mcT2\* analysis allowed for the detection of a short T2\* component in most white matter regions, the separation of components was not possible in regions of severe field inhomogeneities due to T2\* shortening. However, there was the remarkable correspondence of the MWF maps calculated using a two-component model compared to those using NNLS.

We concluded that mcT2\* could not be a suitable whole brain MWF mapping strategy at 3T, but that the use of a two-component model was appropriate for MWF calculations and may perform better at lower SNR.

## **5.4 Feasibility of mcGESSE for myelin mapping: simulations**

A novel acquisition strategy for MWF mapping was presented based on the symmetric gradient echo sampling of the spin echo envelope combined with a two-component model. Named mcGESSE, this approach capitalizes on the sampling density afforded by gradient echoes while maintaining better signal viability near sources of field inhomogeneities by a limited number of spin echoes. Furthermore, this strategy exploits



symmetry inherent of the spin echo signal, which allows us to ignore the functional form of  $T_2'$ . A new objective function is created from this symmetry, based on the signal intensity at equal time intervals before and after the spin echo. This function has only three unknown variables: the MWF ( $A_{MWF}$ ), the T2 of myelin water ( $T_{2_{my}}$ ) and the T2 of the intra/extra-cellular water peak ( $T_{2_{ie}}$ ).

A set of simulations were devised to evaluate the theoretical ability of this strategy to evaluate the MWF. Care was taken to appropriate realistic simulation parameters by inspecting the existing gradient echo dataset from the mcT2\* study. To this end, realistic temporal SNR profiles were created for the cases of severe, mild and no static dephasing at various SNR levels and MWF values. The data fitting approach used was an iteratively re-weighted robust least squares approach (IRRLS). The influence of starting estimates of the data fitting routine on the results was noted. However, the results demonstrated the feasibility of this acquisition strategy to calculate the MWF, with a small bias at small MWF values and decreasing precision at lower SNR or increased static dephasing.

## 5.5 Myelin mapping *in vivo* using mcGESSE

Utilizing the information gleaned from the simulations, mcGESSE was implemented *in-vivo* on our lab's Siemens Verio 3T scanner. Biases due to starting estimates and the spatial dependence of SNR were circumvented using randomly seeded starting estimates and dynamically adjusting the function tolerance of the fitting algorithm to match the SNR of the voxel being analyzed. MWF calculations also benefitted from slight filtering, which reduced the effect of slight signal misregistration caused by the acquisition of images with readout gradients of opposite polarities.

Seven healthy participants were recruited, with six subjects undergoing imaging twice to assess within-subject inter-scan reproducibility. Three of these subjects underwent imaging a third time, within the same session, using an accelerated protocol using parallel imaging. The results of this first implementation of mcGESSE *in-vivo* reflect the potential of this approach for whole brain MWF mapping. Nevertheless, specific areas of concern were discussed in detail and include signal loss in the temporal region and erroneous MWF values in deep grey matter. Also of concern, but predicted by the simulations studies, is a systematic overestimation for lower MWF values, as expected in grey matter. The details of the discussion should provide a good starting point for future development work on mcGESSE.

## 5.6 Significance of this work

Imaging studies in autism continue to support a neurobiological basis. In fact, reported white matter abnormalities, taken alongside the neuropsychological profile of affected and spared functions, support the under-connectivity hypothesis. However, the majority of studies implicated the involvement of white matter with evidence of volumetric, structural and functional abnormalities. Our quantitative assessment of T2 abnormalities has provided evidence of pathophysiological abnormalities of the white matter microstructure. The regional assessment of these abnormalities has highlighted important aspects of aberrant connectivity in autism by implicating radiate and bridging white matter. While studies using DTI also report abnormalities of white matter, the obtained metrics cannot be interpreted as a direct assessment of myelin content. The utility of mcGESSE in obtaining whole-cerebrum MWF measurements will be invaluable in specifying our previously reported T2 abnormalities and ultimately testing the under-connectivity hypothesis.

## 5.7 Future work

Whole brain MWF mapping would be of incredible utility in the study of autism. Beyond providing further specificity to our own findings of increased T2 in white matter, it could provide further clues in regards to questions relating to connectivity, brain overgrowth and microstructural abnormalities detected with other imaging modalities. However, before mcGESSE and the associated analyses can be used in a population study, more work should be done to assess and improve data quality. This work would involve the further optimization of scan parameters used for the acquisition, capitalizing on the multi-echo nature of the acquisition to retrospectively correct for signal losses, and adapting the fitting model to provide more accurate estimates of small MWF values.

## References

- [1] L. Kanner, “Autistic disturbances of affective contact,” *Nervous Child*, vol. 2, no. 2, pp. 217–250, 1943.
- [2] American Psychiatric Association, *Diagnostic and Statistical Manual of Mental Disorders DSM-IV-TR Fourth Edition (Text Revision)*. Washington, DC: American Psychiatric Publishing, 4th ed., July 2000.
- [3] E. Fombonne, R. Zakarian, A. Bennett, L. Meng, and D. McLean-Heywood, “Pervasive developmental disorders in Montreal, Quebec, Canada: prevalence and links with immunizations.,” *Pediatrics*, vol. 118, pp. e139–50, July 2006.
- [4] E. Fombonne, S. Quirke, and A. Hagen, “Prevalence and interpretation of recent trends in rates of pervasive developmental disorders.,” *McGill journal of medicine*, vol. 12, p. 73, Jan. 2009.
- [5] A. Bailey, W. Phillips, and M. Rutter, “Autism: towards an integration of clinical, genetic, neuropsychological, and neurobiological perspectives.,” *Journal of child psychology and psychiatry, and allied disciplines*, vol. 37, pp. 89–126, Jan. 1996.
- [6] S. S. Jeste, “The neurology of autism spectrum disorders.,” *Current opinion in neurology*, vol. 24, pp. 132–9, Apr. 2011.
- [7] S. E. Levy, D. S. Mandell, and R. T. Schultz, “Autism.,” *Lancet*, vol. 374, pp. 1627–38, Nov. 2009.
- [8] M. L. Ganz, “The lifetime distribution of the incremental societal costs of autism.,” *Archives of pediatrics & adolescent medicine*, vol. 161, pp. 343–9, Apr. 2007.

- [9] G. Montes and J. S. Halterman, "Association of childhood autism spectrum disorders and loss of family income.," *Pediatrics*, vol. 121, pp. e821–6, Apr. 2008.
- [10] J. S. Karst and A. V. Van Hecke, "Parent and family impact of autism spectrum disorders: a review and proposed model for intervention evaluation.," *Clinical child and family psychology review*, vol. 15, pp. 247–77, Sept. 2012.
- [11] C. Lord, S. Risi, P. S. DiLavore, C. Shulman, A. Thurm, and A. Pickles, "Autism from 2 to 9 years of age.," *Archives of general psychiatry*, vol. 63, pp. 694–701, July 2006.
- [12] R. Nicolson and P. Szatmari, "Genetic and Neurodevelopmental Influences in Autistic Disorder," *Canadian journal of psychiatry*, vol. 48, no. 8, pp. 526–536, 2003.
- [13] E. DiCicco-Bloom, C. Lord, L. Zwaigenbaum, E. Courchesne, S. R. Dager, C. Schmitz, R. T. Schultz, J. Crawley, and L. J. Young, "The developmental neurobiology of autism spectrum disorder.," *The Journal of neuroscience*, vol. 26, pp. 6897–906, June 2006.
- [14] J. E. Lainhart, "Advances in autism neuroimaging research for the clinician and geneticist.," *American journal of medical genetics*, vol. 142C, pp. 33–9, Feb. 2006.
- [15] K. A. Stigler, B. C. McDonald, A. Anand, A. J. Saykin, and C. J. McDougle, "Structural and functional magnetic resonance imaging of autism spectrum disorders.," *Brain research*, vol. 1380, pp. 146–61, Mar. 2011.
- [16] D. L. Williams and N. J. Minshew, "Understanding autism and related disorders: what has imaging taught us?," *Neuroimaging clinics of North America*, vol. 17, pp. 495–509, ix, Nov. 2007.

- [17] R. A. Carper, P. Moses, Z. D. Tigue, and E. Courchesne, "Cerebral lobes in autism: early hyperplasia and abnormal age effects," *Neuroimage*, vol. 16, pp. 1038–1051, Aug. 2002.
- [18] H. C. Hazlett, M. Poe, G. Gerig, R. G. Smith, J. Provenzale, A. Ross, J. Gilmore, and J. Piven, "Magnetic resonance imaging and head circumference study of brain size in autism: birth through age 2 years.," *Archives of general psychiatry*, vol. 62, pp. 1366–76, Dec. 2005.
- [19] T. Nickl-Jockschat, U. Habel, T. Maria Michel, J. Manning, A. R. Laird, P. T. Fox, F. Schneider, and S. B. Eickhoff, "Brain structure anomalies in autism spectrum disorder-a meta-analysis of VBM studies using anatomic likelihood estimation.," *Human brain mapping*, vol. 33, June 2011.
- [20] S. Dager, N. Oskin, T. Richards, and S. Posse, "Research Applications of Magnetic Resonance Spectroscopy (MRS) to Investigate Psychiatry Disorders," *Topics in magnetic resonance imaging: TMRI*, vol. 19, no. 2, p. 81, 2008.
- [21] T. J. DeVito, D. J. Drost, R. W. Neufeld, N. Rajakumar, W. Pavlosky, P. Williamson, and R. Nicolson, "Evidence for cortical dysfunction in autism: a proton magnetic resonance spectroscopic imaging study," *Biological Psychiatry*, vol. 61, no. 4, pp. 465–473, 2007.
- [22] R. Chen, Y. Jiao, and E. H. Herskovits, "Structural MRI in autism spectrum disorder.," *Pediatric research*, vol. 69, pp. 63R–8R, May 2011.
- [23] D. K. Jones and M. Cercignani, "Twenty-five pitfalls in the analysis of diffusion MRI data.," *NMR in biomedicine*, vol. 23, pp. 803–20, Aug. 2010.
- [24] S. B. Vos, D. K. Jones, B. Jeurissen, M. a. Viergever, and A. Leemans, "The influence of complex white matter architecture on the mean diffusivity in diffu-

- sion tensor MRI of the human brain.,” *NeuroImage*, vol. 59, pp. 2208–16, Feb. 2012.
- [25] N. N. J. Minshew and D. D. L. Williams, “The new neurobiology of autism: cortex, connectivity, and neuronal organization.,” *Archives of neurology*, vol. 64, p. 945, July 2007.
- [26] M. A. Just, V. L. Cherkassky, T. a. Keller, and N. J. Minshew, “Cortical activation and synchronization during sentence comprehension in high-functioning autism: evidence of underconnectivity.,” *Brain*, vol. 127, pp. 1811–21, Aug. 2004.
- [27] M. A. Just, V. L. Cherkassky, T. a. Keller, R. K. Kana, and N. J. Minshew, “Functional and anatomical cortical underconnectivity in autism: evidence from an fMRI study of an executive function task and corpus callosum morphometry.,” *Cerebral cortex*, vol. 17, pp. 951–61, Apr. 2007.
- [28] M. K. Belmonte, G. Allen, A. Beckel-Mitchener, L. M. Boulanger, R. a. Carper, and S. J. Webb, “Autism and abnormal development of brain connectivity.,” *The Journal of neuroscience*, vol. 24, pp. 9228–31, Oct. 2004.
- [29] S. Wass, “Distortions and disconnections: disrupted brain connectivity in autism.,” *Brain and cognition*, vol. 75, pp. 18–28, Feb. 2011.
- [30] N. J. Minshew and J. A. Hobson, “Sensory sensitivities and performance on sensory perceptual tasks in high-functioning individuals with autism,” *Journal of autism and developmental disorders*, vol. 38, no. 8, pp. 1485–1498, 2008.
- [31] C. Laule, I. M. Vavasour, S. H. Kolind, D. K. B. Li, T. L. Traboulsee, G. R. W. Moore, and A. L. MacKay, “Magnetic resonance imaging of myelin.,” *Neurotherapeutics*, vol. 4, pp. 460–84, July 2007.

- [32] H. C. Kinney, B. A. Brody, A. S. Kloman, and F. H. Gilles, "Sequence of central nervous system myelination in human infancy. II. Patterns of myelination in autopsied infants.," *Journal of neuropathology and experimental neurology*, vol. 47, pp. 217–34, May 1988.
- [33] T. Paus, "Growth of white matter in the adolescent brain: myelin or axon?," *Brain and cognition*, vol. 72, pp. 26–35, Feb. 2010.
- [34] B. J. Jellison, A. S. Field, J. Medow, M. Lazar, M. S. Salamat, and A. L. Alexander, "Diffusion tensor imaging of cerebral white matter: a pictorial review of physics, fiber tract anatomy, and tumor imaging patterns.," *American journal of neuroradiology*, vol. 25, pp. 356–69, Mar. 2004.
- [35] J. Pickett, "Current investigations in autism brain tissue research.," *Journal of autism and developmental disorders*, vol. 31, pp. 521–7, Dec. 2001.
- [36] S. H. Ameis and P. Szatmari, "Imaging-genetics in autism spectrum disorder: advances, translational impact, and future directions.," *Frontiers in psychiatry / Frontiers Research Foundation*, vol. 3, p. 46, Jan. 2012.
- [37] G. D. E. L. A. Tourette, E. Albert, and B. Etude, "Etude sur une affection nerveuse caractérisée par de l'incoordination motrice accompagnée d'écholalie et de coprolalie," *Archives de neurologie*, vol. 9, no. c, pp. 19–42, 1885.
- [38] J. Jankovic and R. Kurlan, "Tourette syndrome: evolving concepts.," *Movement disorders*, vol. 26, pp. 1149–56, May 2011.
- [39] J. F. Leckman, "Tourettes syndrome," *The Lancet*, vol. 360, pp. 1577–1586, 2002.
- [40] J. Jankovic, "Tourette's syndrome.," *The New England journal of medicine*, vol. 345, pp. 1184–92, Oct. 2001.



- [41] M. M. Robertson, V. Eapen, and A. E. Cavanna, “The international prevalence, epidemiology, and clinical phenomenology of Tourette syndrome: a cross-cultural perspective.,” *Journal of psychosomatic research*, vol. 67, pp. 475–83, Dec. 2009.
- [42] H. Rickards, “Functional neuroimaging in Tourette syndrome.,” *Journal of psychosomatic research*, vol. 67, pp. 575–84, Dec. 2009.
- [43] M. M. Robertson, “Diagnosing Tourette syndrome: Is it a common disorder?,” *Journal of Psychosomatic Research*, vol. 55, pp. 3–6, July 2003.
- [44] J. F. Leckman, M. H. Bloch, M. E. Smith, D. Larabi, and M. Hampson, “Neurobiological substrates of Tourette’s disorder.,” *Journal of child and adolescent psychopharmacology*, vol. 20, pp. 237–47, Aug. 2010.
- [45] B. S. Peterson, P. Thomas, M. J. Kane, L. Scahill, H. Zhang, R. Bronen, R. a. King, J. F. Leckman, and L. Staib, “Basal Ganglia volumes in patients with Gilles de la Tourette syndrome.,” *Archives of general psychiatry*, vol. 60, pp. 415–24, Apr. 2003.
- [46] B. S. Peterson, P. Skudlarski, a. W. Anderson, H. Zhang, J. C. Gatenby, C. M. Lacadie, J. F. Leckman, and J. C. Gore, “A functional magnetic resonance imaging study of tic suppression in Tourette syndrome.,” *Archives of general psychiatry*, vol. 55, pp. 326–33, Apr. 1998.
- [47] E. Stern, D. a. Silbersweig, K. Y. Chee, a. Holmes, M. M. Robertson, M. Trimble, C. D. Frith, R. S. Frackowiak, and R. J. Dolan, “A functional neuroanatomy of tics in Tourette syndrome.,” *Archives of general psychiatry*, vol. 57, pp. 741–8, Aug. 2000.
- [48] T. M. Hyde, M. E. Stacey, R. Coppola, S. F. Handel, K. C. Rickler, and D. R. Weinberger, “Cerebral morphometric abnormalities in Tourette’s syndrome: a

- quantitative MRI study of monozygotic twins.,” *Neurology*, vol. 45, pp. 1176–82, June 1995.
- [49] B. S. Peterson, L. Staib, L. Scahill, H. Zhang, C. Anderson, J. F. Leckman, D. J. Cohen, J. C. Gore, J. Albert, and R. Webster, “Regional brain and ventricular volumes in Tourette syndrome.,” *Archives of general psychiatry*, vol. 58, pp. 427–40, May 2001.
- [50] K. a. Fredericksen, L. E. Cutting, W. R. Kates, S. H. Mostofsky, H. S. Singer, K. L. Cooper, D. C. Lanham, M. B. Denckla, and W. E. Kaufmann, “Disproportionate increases of white matter in right frontal lobe in Tourette syndrome.,” *Neurology*, vol. 58, pp. 85–9, Jan. 2002.
- [51] K.-E. Hong, S.-M. Ock, M.-H. Kang, C.-E. Kim, J.-N. Bae, M.-K. Lim, C.-H. Suh, S.-J. Chung, S.-C. Cho, and J.-S. Lee, “The segmented regional volumes of the cerebrum and cerebellum in boys with Tourette syndrome.,” *Journal of Korean medical science*, vol. 17, pp. 530–6, Aug. 2002.
- [52] E. R. Sowell, E. Kan, J. Yoshii, P. M. Thompson, R. Bansal, D. Xu, A. W. Toga, and B. S. Peterson, “Thinning of sensorimotor cortices in children with Tourette syndrome.,” *Nature neuroscience*, vol. 11, pp. 637–9, June 2008.
- [53] T. J. DeVito, D. J. Drost, W. Pavlosky, R. W. J. Neufeld, N. Rajakumar, B. D. McKinlay, P. C. Williamson, and R. Nicolson, “Brain magnetic resonance spectroscopy in Tourette’s disorder.,” *Journal of the American Academy of Child and Adolescent Psychiatry*, vol. 44, pp. 1301–8, Dec. 2005.
- [54] J. F. Leckman, C. B. Yeh, and D. J. Cohen, “Tic disorders: when habit forming neural systems form habits of their own?,” *Zhonghua yi xue za zhi = Chinese medical journal; Free China ed*, vol. 64, pp. 669–92, Dec. 2001.

- [55] J. W. Mink, “Neurobiology of basal ganglia circuits in Tourette syndrome: faulty inhibition of unwanted motor patterns?,” *Advances in neurology*, vol. 85, pp. 113–22, Jan. 2001.
- [56] M. W. State, “The genetics of Tourette disorder.,” *Current opinion in genetics & development*, vol. 21, pp. 302–9, June 2011.
- [57] R. J. Felling and H. S. Singer, “Neurobiology of tourette syndrome: current status and need for further investigation.,” *The Journal of neuroscience*, vol. 31, pp. 12387–95, Aug. 2011.
- [58] F. Bloch, “Nuclear Induction,” *Physical Review*, vol. 70, pp. 460–474, Oct. 1946.
- [59] D. I. Hoult, C. N. Chen, and V. J. Sank, “Quadrature detection in the laboratory frame.,” *Magnetic resonance in medicine*, vol. 1, pp. 339–53, Sept. 1984.
- [60] N. Bloembergen, E. Purcell, and R. Pound, “Relaxation Effects in Nuclear Magnetic Resonance Absorption,” *Physical Review*, vol. 73, pp. 679–712, Apr. 1948.
- [61] N. Gelman, J. M. Gorell, P. B. Barker, R. M. Savage, E. M. Spickler, J. P. Windham, and R. A. Knight, “MR imaging of human brain at 3.0 T: preliminary report on transverse relaxation rates and relation to estimated iron content,” *Radiology*, vol. 210, no. 3, pp. 759–767, 1999.
- [62] J. Vymazal, R. A. Brooks, N. Patronas, M. Hajek, J. W. Bulte, and G. Di Chiro, “Magnetic resonance imaging of brain iron in health and disease.,” *Journal of the neurological sciences*, vol. 134 Suppl, pp. 19–26, Dec. 1995.
- [63] D. H. Miller, R. I. Grossman, S. C. Reingold, and H. F. McFarland, “The role of magnetic resonance techniques in understanding and managing multiple sclerosis,” *Brain*, vol. 121 ( Pt 1, pp. 3–24, 1998.

- [64] A. Bernasconi, N. Bernasconi, Z. Caramanos, D. C. Reutens, F. Andermann, F. Dubeau, D. Tampieri, B. G. Pike, and D. L. Arnold, “T2 relaxometry can lateralize mesial temporal lobe epilepsy in patients with normal MRI,” *Neuroimage*, vol. 12, no. 6, pp. 739–746, 2000.
- [65] P. Williamson, D. Pelz, H. Merskey, S. Morrison, S. Karlik, D. Drost, T. Carr, and P. Conlon, “Frontal, temporal, and striatal proton relaxation times in schizophrenic patients and normal comparison subjects.,” *The American journal of psychiatry*, vol. 149, pp. 549–51, Apr. 1992.
- [66] C. H. Salmond, M. de Haan, K. J. Friston, D. G. Gadian, and F. Vargha-Khadem, “Investigating individual differences in brain abnormalities in autism.,” *Philosophical transactions of the Royal Society of London. Series B, Biological sciences*, vol. 358, pp. 405–13, Feb. 2003.
- [67] J. Hendry, T. DeVito, N. Gelman, M. Densmore, N. Rajakumar, W. Pavlosky, P. C. Williamson, P. M. Thompson, D. J. Drost, and R. Nicolson, “White matter abnormalities in autism detected through transverse relaxation time imaging.,” *NeuroImage*, vol. 29, pp. 1049–57, Feb. 2006.
- [68] H. Petropoulos, S. D. Friedman, D. W. W. Shaw, A. A. Artru, G. Dawson, and S. R. Dager, “Gray matter abnormalities in autism spectrum disorder revealed by T2 relaxation,” *Neurology*, vol. 67, pp. 632–636, Aug. 2006.
- [69] E. H. J. E. Voormolen, C. Wei, E. W. C. E. Chow, A. S. A. Bassett, D. J. D. Mikulis, and A. P. A. Crawley, “Voxel-based morphometry and automated lobar volumetry: the trade-off between spatial scale and statistical correction.,” *NeuroImage*, vol. 49, pp. 587–96, Jan. 2010.
- [70] N. R. Giuliani, V. D. Calhoun, G. D. Pearlson, A. Francis, and R. W. Buchanan, “Voxel-based morphometry versus region of interest: a comparison of two meth-

- ods for analyzing gray matter differences in schizophrenia.,” *Schizophrenia research*, vol. 74, pp. 135–47, May 2005.
- [71] M. R. Herbert, D. a. Ziegler, N. Makris, P. A. Filipek, T. L. Kemper, J. J. Normandin, H. A. Sanders, D. N. Kennedy, V. S. Caviness, and V. S. Caviness Jr., “Localization of white matter volume increase in autism and developmental language disorder.,” *Annals of neurology*, vol. 55, pp. 530–40, Apr. 2004.
- [72] C. Lord, M. Rutter, and A. Le Couteur, “Autism Diagnostic Interview-Revised: a revised version of a diagnostic interview for caregivers of individuals with possible pervasive developmental disorders,” *Journal of autism and developmental disorders*, vol. 24, no. 5, pp. 659–685, 1994.
- [73] C. Lord, S. Risi, L. Lambrecht, E. H. Cook Jr., B. L. Leventhal, P. C. DiLavore, A. Pickles, and M. Rutter, “The autism diagnostic observation schedule-generic: a standard measure of social and communication deficits associated with the spectrum of autism,” *Journal of autism and developmental disorders*, vol. 30, no. 3, pp. 205–223, 2000.
- [74] J. Kaufman, B. Birmaher, D. Brent, U. Rao, C. Flynn, P. Moreci, D. Williamson, and N. Ryan, “Schedule for Affective Disorders and Schizophrenia for School-Age Children-Present and Lifetime Version (K-SADS-PL): initial reliability and validity data,” *Journal of the American Academy of Child and Adolescent Psychiatry*, vol. 36, no. 7, pp. 980–988, 1997.
- [75] J. Ma and F. W. Wehrli, “Method for image-based measurement of the reversible and irreversible contribution to the transverse-relaxation rate.,” *Journal of magnetic resonance. Series B*, vol. 111, pp. 61–9, Apr. 1996.
- [76] A. J. Miller and P. M. Joseph, “The use of power images to perform quantitative analysis on low SNR MR images.,” *Magnetic resonance imaging*, vol. 11, pp. 1051–6, Jan. 1993.

- [77] J. Ashburner, P. Neelin, D. L. Collins, A. Evans, and K. Friston, “Incorporating prior knowledge into image registration,” *Neuroimage*, vol. 6, no. 4, pp. 344–352, 1997.
- [78] J. Ashburner and K. J. Friston, “Nonlinear spatial normalization using basis functions.,” *Human brain mapping*, vol. 7, pp. 254–66, Jan. 1999.
- [79] J. A. Maldjian, P. J. Laurienti, R. A. Kraft, and J. H. Burdette, “An automated method for neuroanatomic and cytoarchitectonic atlas-based interrogation of fMRI data sets,” *Neuroimage*, vol. 19, no. 3, pp. 1233–1239, 2003.
- [80] N. Makris, J. W. Meyer, J. F. Bates, E. H. Yeterian, D. N. Kennedy, and V. S. Caviness, “MRI-Based Topographic Parcellation of Human Cerebral White Matter and Nuclei of Cerebral Connectivity,” *NeuroImage*, vol. 45, pp. 18–45, 1999.
- [81] K. Oishi, A. Faria, H. Jiang, X. Li, K. Akhter, J. Zhang, J. T. Hsu, M. I. Miller, P. C. M. van Zijl, M. Albert, C. G. Lyketsos, R. Woods, A. W. Toga, G. B. Pike, P. Rosa-Neto, A. Evans, J. Mazziotta, and S. Mori, “Atlas-based whole brain white matter analysis using large deformation diffeomorphic metric mapping: application to normal elderly and Alzheimer’s disease participants.,” *NeuroImage*, vol. 46, pp. 486–99, June 2009.
- [82] R. I. Hassink, B. Hiltbrunner, S. Muller, and J. Lutschg, “Assessment of brain maturation by T2-weighted MRI,” *Neuropediatrics*, vol. 23, no. 2, pp. 72–74, 1992.
- [83] P. R. Escalante-Mead, N. J. Minshew, and J. A. Sweeney, “Abnormal brain lateralization in high-functioning autism.,” *Journal of autism and developmental disorders*, vol. 33, pp. 539–43, Oct. 2003.

- [84] E. Fombonne, “Epidemiological surveys of autism and other pervasive developmental disorders: an update.,” *Journal of autism and developmental disorders*, vol. 33, pp. 365–82, Aug. 2003.
- [85] J. N. Giedd, L. S. Clasen, R. Lenroot, D. Greenstein, G. L. Wallace, S. Ordaz, E. a. Molloy, J. D. Blumenthal, J. W. Tossell, C. Stayer, C. a. Samango-Sprouse, D. Shen, C. Davatzikos, D. Merke, and G. P. Chrousos, “Puberty-related influences on brain development.,” *Molecular and cellular endocrinology*, vol. 254-255, pp. 154–62, July 2006.
- [86] D. a. Yablonskiy and E. M. Haacke, “An MRI method for measuring T2 in the presence of static and RF magnetic field inhomogeneities.,” *Magnetic resonance in medicine*, vol. 37, pp. 872–6, June 1997.
- [87] S. Majumdar, S. C. Orphanoudakis, A. Gmitro, M. O’Donnell, and J. C. Gore, “Errors in the measurements of T2 using multiple-echo MRI techniques. I. Effects of radiofrequency pulse imperfections,” *Magnetic resonance in medicine*, vol. 3, no. 3, pp. 397–417, 1986.
- [88] S. Majumdar, S. C. Orphanoudakis, A. Gmitro, M. O’Donnell, and J. C. Gore, “Errors in the measurements of T2 using multiple-echo MRI techniques. II. Effects of static field inhomogeneity,” *Magnetic resonance in medicine*, vol. 3, no. 4, pp. 562–574, 1986.
- [89] M. Wilke, V. J. Schmithorst, and S. K. Holland, “Assessment of spatial normalization of whole-brain magnetic resonance images in children.,” *Human brain mapping*, vol. 17, pp. 48–60, Sept. 2002.
- [90] M. P. Milham, A. C. Nugent, W. C. Drevets, D. P. Dickstein, E. Leibenluft, M. Ernst, D. Charney, and D. S. Pine, “Selective reduction in amygdala volume in pediatric anxiety disorders: a voxel-based morphometry investigation.,” *Biological psychiatry*, vol. 57, pp. 961–6, May 2005.

- [91] E. D. Burgund, H. C. Kang, J. E. Kelly, R. L. Buckner, A. Z. Snyder, S. E. Petersen, and B. L. Schlaggar, “The feasibility of a common stereotactic space for children and adults in fMRI studies of development,” *Neuroimage*, vol. 17, no. 1, pp. 184–200, 2002.
- [92] C. M. Anderson, M. J. Kaufman, S. B. Lowen, M. Rohan, P. F. Renshaw, and M. H. Teicher, “Brain T2 relaxation times correlate with regional cerebral blood volume.,” *Magnetic Resonance Materials in Physics, Biology and Medicine*, vol. 18, pp. 3–6, Mar. 2005.
- [93] S. J. Graham, P. L. Stanchev, and M. J. Bronskill, “Criteria for analysis of multicomponent tissue T2 relaxation data.,” *Magnetic resonance in medicine*, vol. 35, pp. 370–8, Mar. 1996.
- [94] A. MacKay, K. Whittall, J. Adler, D. Li, D. Paty, and D. Graeb, “In vivo visualization of myelin water in brain by magnetic resonance.,” *Magnetic Resonance in Medicine*, vol. 31, pp. 673–7, June 1994.
- [95] C. Beaulieu, “The basis of anisotropic water diffusion in the nervous system - a technical review.,” *NMR in biomedicine*, vol. 15, no. 7-8, pp. 435–55, 2002.
- [96] A. MacKay, C. Laule, I. Vavasour, T. Bjarnason, S. Kolind, B. Madler, and B. Mädler, “Insights into brain microstructure from the T2 distribution.,” *Magnetic resonance imaging*, vol. 24, pp. 515–25, May 2006.
- [97] M. Gomot, F. A. Bernard, M. H. Davis, M. K. Belmonte, C. Ashwin, E. T. Bullmore, and S. Baron-Cohen, “Change detection in children with autism: an auditory event-related fMRI study,” *Neuroimage*, vol. 29, no. 2, pp. 475–484, 2006.
- [98] H. Koshino, P. A. Carpenter, N. J. Minshew, V. L. Cherkassky, T. A. Keller,



- and M. A. Just, “Functional connectivity in an fMRI working memory task in high-functioning autism,” *Neuroimage*, vol. 24, no. 3, pp. 810–821, 2005.
- [99] F. Haist, M. Adamo, M. Westerfield, E. Courchesne, and J. Townsend, “The functional neuroanatomy of spatial attention in autism spectrum disorder.,” *Developmental neuropsychology*, vol. 27, pp. 425–58, Jan. 2005.
- [100] E. D. Bigler, S. Mortensen, E. S. Neeley, S. Ozonoff, L. Krasny, M. Johnson, J. Lu, S. L. Provencal, W. McMahon, and J. E. Lainhart, “Superior temporal gyrus, language function, and autism.,” *Developmental neuropsychology*, vol. 31, pp. 217–38, Jan. 2007.
- [101] M. R. Herbert, D. A. Ziegler, C. K. Deutsch, L. M. O’Brien, D. N. Kennedy, P. a. Filipek, A. I. Bakardjiev, J. Hodgson, M. Takeoka, N. Makris, and V. S. Caviness, “Brain asymmetries in autism and developmental language disorder: a nested whole-brain analysis.,” *Brain*, vol. 128, pp. 213–26, Jan. 2005.
- [102] F. M. Benes, “Myelination of cortical-hippocampal relays during late adolescence.,” *Schizophrenia bulletin*, vol. 15, pp. 585–93, Jan. 1989.
- [103] B. S. Peterson, J. C. Gore, M. A. Riddle, D. J. Cohen, and J. F. Leckman, “Abnormal magnetic resonance imaging T2 relaxation time asymmetries in Tourette’s syndrome.,” *Psychiatry research*, vol. 55, pp. 205–21, Dec. 1994.
- [104] J. F. Leckman, M. A. Riddle, M. T. Hardin, S. I. Ort, K. L. Swartz, J. Stevenson, and D. J. Cohen, “The Yale Global Tic Severity Scale: initial testing of a clinician-rated scale of tic severity.,” *Journal of the American Academy of Child and Adolescent Psychiatry*, vol. 28, pp. 566–73, July 1989.
- [105] R. D. Freeman, D. K. Fast, L. Burd, J. Kerbeshian, M. M. Robertson, and P. Sandor, “An international perspective on Tourette syndrome: selected find-

- ings from 3,500 individuals in 22 countries.,” *Developmental medicine and child neurology*, vol. 42, pp. 436–47, July 2000.
- [106] J. Moriarty, D. C. Costa, B. Schmitz, M. R. Trimble, P. J. Ell, and M. M. Robertson, “Brain perfusion abnormalities in Gilles de la Tourette’s syndrome.,” *The British journal of psychiatry*, vol. 167, pp. 249–54, Aug. 1995.
- [107] J. Moriarty, V. Eapen, D. C. Costa, S. Gacinovic, M. Trimble, P. J. Ell, and M. M. Robertson, “HMPAO SPET does not distinguish obsessive-compulsive and tic syndromes in families multiply affected with Gilles de la Tourette’s syndrome.,” *Psychological medicine*, vol. 27, pp. 737–40, May 1997.
- [108] G. D. Fullerton, J. L. Potter, and N. C. Dornbluth, “NMR relaxation of protons in tissues and other macromolecular water solutions,” *Magnetic resonance imaging*, vol. 1, no. 4, pp. 209–226, 1982.
- [109] E. Gerard and B. S. Peterson, “Developmental processes and brain imaging studies in Tourette syndrome.,” *Journal of psychosomatic research*, vol. 55, pp. 13–22, July 2003.
- [110] X.-l. Li, J.-h. Sun, F. Li, M.-j. Huang, Q.-q. Li, Q.-z. Wu, T.-j. Zhang, L.-t. Guo, Q.-y. Gong, and X.-q. Huang, “Microstructural abnormalities of basal ganglia and thalamus in children with first-episode Tourette’s syndrome: a diffusion tensor imaging study.,” *Sichuan da xue xue bao. Yi xue ban = Journal of Sichuan University. Medical science edition*, vol. 41, pp. 284–7, Mar. 2010.
- [111] I. R. Levesque and G. B. Pike, “Characterizing healthy and diseased white matter using quantitative magnetization transfer and multicomponent T(2) relaxometry: A unified view via a four-pool model.,” *Magnetic resonance in medicine*, vol. 62, pp. 1487–96, Dec. 2009.

- [112] V. Vasilescu, E. Katona, V. Simpliceanu, and D. Demco, “Water compartments in the myelinated nerve. III. Pulsed NMR results.,” *Experientia*, vol. 34, pp. 1443–4, Nov. 1978.
- [113] R. Kroeker and R. M. Henkelman, “Analysis of biological NMR relaxation data with continuous distributions of relaxation times,” *Journal of Magnetic Resonance*, vol. 235, pp. 218–235, 1986.
- [114] K. P. Whittall and A. L. MacKay, “Quantitative interpretation of NMR relaxation data,” *Journal of Magnetic Resonance*, vol. 84, pp. 134–152, Aug. 1989.
- [115] R. S. Menon and P. S. Allen, “Application of continuous relaxation time distributions to the fitting of data from model systems and excised tissue.,” *Magnetic resonance in medicine*, vol. 20, pp. 214–27, Aug. 1991.
- [116] R. S. Menon, M. S. Rusinko, and P. S. Allen, “Proton relaxation studies of water compartmentalization in a model neurological system.,” *Magnetic resonance in medicine*, vol. 28, pp. 264–74, Dec. 1992.
- [117] W. A. Stewart, A. L. MacKay, K. P. Whittall, G. R. Moore, and D. W. Paty, “Spin-spin relaxation in experimental allergic encephalomyelitis. Analysis of CPMG data using a non-linear least squares method and linear inverse theory.,” *Magnetic resonance in medicine*, vol. 29, pp. 767–75, June 1993.
- [118] K. P. Whittall, A. L. MacKay, D. A. Graeb, R. A. Nugent, D. K. Li, and D. W. Paty, “In vivo measurement of T2 distributions and water contents in normal human brain.,” *Magnetic resonance in medicine*, vol. 37, pp. 34–43, Jan. 1997.
- [119] S. H. Kolind, B. Mädler, S. Fischer, D. K. B. Li, and A. L. MacKay, “Myelin water imaging: Implementation and development at 3.0T and comparison to 1.5T measurements.,” *Magnetic resonance in medicine*, vol. 62, pp. 106–15, July 2009.

- [120] A. R. Travis and M. D. Does, “Selective excitation of myelin water using inversion-recovery-based preparations.,” *Magnetic resonance in medicine*, vol. 54, pp. 743–7, Sept. 2005.
- [121] G. R. Moore, E. Leung, a. L. MacKay, I. M. Vavasour, K. P. Whittall, K. S. Cover, D. K. Li, S. a. Hashimoto, J. Oger, T. J. Sprinkle, and D. W. Paty, “A pathology-MRI study of the short-T2 component in formalin-fixed multiple sclerosis brain.,” *Neurology*, vol. 55, pp. 1506–10, Nov. 2000.
- [122] T. Andrews, J. L. Lancaster, S. J. Dodd, C. Contreras-Sesvold, and P. T. Fox, “Testing the three-pool white matter model adapted for use with T2 relaxometry.,” *Magnetic resonance in medicine : official journal of the Society of Magnetic Resonance in Medicine / Society of Magnetic Resonance in Medicine*, vol. 54, pp. 449–54, Aug. 2005.
- [123] C. K. Jones, Q.-S. Xiang, K. P. Whittall, and A. L. MacKay, “Linear combination of multiecho data: short T2 component selection.,” *Magnetic resonance in medicine*, vol. 51, pp. 495–502, Mar. 2004.
- [124] L. Vidarsson, S. M. Conolly, K. O. Lim, G. E. Gold, and J. M. Pauly, “Echo time optimization for linear combination myelin imaging.,” *Magnetic resonance in medicine*, vol. 53, pp. 398–407, Feb. 2005.
- [125] C. Laule, S. H. Kolind, T. A. Bjarnason, D. K. B. Li, and A. L. MacKay, “In vivo multiecho T2 relaxation measurements using variable TR to decrease scan time.,” *Magnetic resonance imaging*, vol. 25, pp. 834–9, July 2007.
- [126] A. Haase, “Snapshot FLASH MRI. Applications to T1, T2, and chemical-shift imaging.,” *Magnetic resonance in medicine*, vol. 13, pp. 77–89, Jan. 1990.
- [127] J. Oh, E. T. Han, D. Pelletier, and S. J. Nelson, “Measurement of in vivo multi-

- component T2 relaxation times for brain tissue using multi-slice T2 prep at 1.5 and 3 T.,” *Magnetic resonance imaging*, vol. 24, pp. 33–43, Jan. 2006.
- [128] J. Oh, E. T. Han, M. C. Lee, S. J. Nelson, and D. Pelletier, “Multislice brain myelin water fractions at 3T in multiple sclerosis.,” *Journal of neuroimaging*, vol. 17, pp. 156–63, Apr. 2007.
- [129] T. Prasloski, B. Mädler, Q.-S. Xiang, A. Mackay, and C. Jones, “Applications of stimulated echo correction to multicomponent T(2) analysis.,” *Magnetic resonance in medicine*, vol. 000, pp. 1–12, Oct. 2011.
- [130] T. Prasloski, A. Rauscher, A. L. Mackay, M. Hodgson, I. M. Vavasour, C. Laule, and B. Mädler, “Rapid whole cerebrum myelin water imaging using a 3D GRASE sequence.,” *NeuroImage*, July 2012.
- [131] Y. P. Du, R. Chu, D. Hwang, M. S. Brown, B. K. Kleinschmidt-DeMasters, D. Singel, and J. H. Simon, “Fast multislice mapping of the myelin water fraction using multicompartiment analysis of T2\* decay at 3T: a preliminary post-mortem study.,” *Magnetic resonance in medicine*, vol. 58, pp. 865–70, Nov. 2007.
- [132] D. Hwang, D.-H. Kim, and Y. P. Du, “In vivo multi-slice mapping of myelin water content using T2\* decay.,” *NeuroImage*, vol. 52, pp. 198–204, Aug. 2010.
- [133] S. C. L. Deoni, B. K. Rutt, T. Arun, C. Pierpaoli, and D. K. Jones, “Gleaning multicomponent T1 and T2 information from steady-state imaging data.,” *Magnetic resonance in medicine*, vol. 60, pp. 1372–87, Dec. 2008.
- [134] S. C. L. Deoni, B. K. Rutt, and D. K. Jones, “Investigating exchange and multicomponent relaxation in fully-balanced steady-state free precession imaging.,” *Journal of magnetic resonance imaging*, vol. 27, pp. 1421–9, June 2008.

- [135] S. C. L. Deoni, T. M. Peters, and B. K. Rutt, “High-resolution T1 and T2 mapping of the brain in a clinically acceptable time with DESPOT1 and DESPOT2,” *Magnetic resonance in medicine*, vol. 53, pp. 237–241, Jan. 2005.
- [136] S. C. L. Deoni, H. a. Ward, T. M. Peters, and B. K. Rutt, “Rapid T2 estimation with phase-cycled variable nutation steady-state free precession,” *Magnetic resonance in medicine*, vol. 52, pp. 435–439, Aug. 2004.
- [137] S. C. L. Deoni, T. M. Peters, and B. K. Rutt, “Determination of optimal angles for variable nutation proton magnetic spin-lattice, T1, and spin-spin, T2, relaxation times measurement.,” *Magnetic resonance in medicine*, vol. 51, pp. 194–9, Jan. 2004.
- [138] S. C. L. Deoni, “High-resolution T1 mapping of the brain at 3T with driven equilibrium single pulse observation of T1 with high-speed incorporation of RF field inhomogeneities (DESPOT1-HIFI).,” *Journal of magnetic resonance imaging*, vol. 26, pp. 1106–11, Oct. 2007.
- [139] C. Lenz, M. Klarhöfer, and K. Scheffler, “Limitations of rapid myelin water quantification using 3D bSSFP.,” *Magnetic Resonance Materials in Physics, Biology and Medicine*, vol. 23, pp. 139–51, June 2010.
- [140] C. L. Lankford and M. D. Does, “On the inherent precision of mcDESPOT.,” *Magnetic resonance in medicine*, vol. 000, Mar. 2012.
- [141] C. K. Jones, K. P. Whittall, and A. L. MacKay, “Robust myelin water quantification: averaging vs. spatial filtering.,” *Magnetic resonance in medicine*, vol. 50, pp. 206–9, July 2003.
- [142] M. Alecci, C. M. Collins, M. B. Smith, and P. Jezzard, “Radio frequency magnetic field mapping of a 3 Tesla birdcage coil: experimental and theoretical

- dependence on sample properties.,” *Magnetic resonance in medicine*, vol. 46, pp. 379–85, Aug. 2001.
- [143] D. Le Bihan, C. Poupon, A. Amadon, and F. Lethimonnier, “Artifacts and pitfalls in diffusion MRI.,” *Journal of magnetic resonance imaging*, vol. 24, pp. 478–88, Sept. 2006.
- [144] C. Laule, E. Leung, D. K. Li, a. L. Traboulsee, D. W. Paty, a. L. MacKay, and G. R. Moore, “Myelin water imaging in multiple sclerosis: quantitative correlations with histopathology,” *Multiple Sclerosis*, vol. 12, pp. 747–753, Nov. 2006.
- [145] H. H. Kitzler, J. Su, M. Zeineh, C. Harper-Little, A. Leung, M. Kremenchutzky, S. C. Deoni, and B. K. Rutt, “Deficient MWF mapping in multiple sclerosis using 3D whole-brain multi-component relaxation MRI.,” *NeuroImage*, vol. 59, pp. 4–11, Sept. 2011.
- [146] S. Kolind, L. Matthews, H. Johansen-Berg, M. I. Leite, S. C. R. Williams, S. Deoni, and J. Palace, “Myelin water imaging reflects clinical variability in multiple sclerosis.,” *NeuroImage*, vol. 60, pp. 263–270, Dec. 2011.
- [147] C. Laule, I. M. Vavasour, G. R. W. Moore, J. Oger, D. K. B. Li, D. W. Paty, and a. L. MacKay, “Water content and myelin water fraction in multiple sclerosis. A T2 relaxation study.,” *Journal of neurology*, vol. 251, pp. 284–93, Mar. 2004.
- [148] D. J. Tozer, G. R. Davies, D. R. Altmann, D. H. Miller, and P. S. Tofts, “Correlation of apparent myelin measures obtained in multiple sclerosis patients and controls from magnetization transfer and multicompartamental T2 analysis.,” *Magnetic resonance in medicine*, vol. 53, pp. 1415–22, June 2005.
- [149] S. W. Flynn, D. J. Lang, a. L. Mackay, V. Goghari, I. M. Vavasour, K. P. Whittall, G. N. Smith, V. Arango, J. J. Mann, a. J. Dwork, P. Falkai, and W. G.

- Honer, “Abnormalities of myelination in schizophrenia detected in vivo with MRI, and post-mortem with analysis of oligodendrocyte proteins.,” *Molecular psychiatry*, vol. 8, pp. 811–20, Sept. 2003.
- [150] C. Jones, A. MacKay, and B. Rutt, “Bi-exponential T2 decay in dairy cream phantoms.,” *Magnetic resonance imaging*, vol. 16, pp. 83–5, Jan. 1998.
- [151] E. Kaza, U. Klose, and M. Lotze, “Comparison of a 32-channel with a 12-channel head coil: are there relevant improvements for functional imaging?,” *Journal of magnetic resonance imaging*, vol. 34, pp. 173–83, July 2011.
- [152] G. C. Wiggins, C. Triantafyllou, A. Potthast, A. Reykowski, M. Nittka, and L. L. Wald, “32-channel 3 Tesla receive-only phased-array head coil with soccer-ball element geometry.,” *Magnetic resonance in medicine*, vol. 56, pp. 216–23, July 2006.
- [153] J. Ashburner and K. J. Friston, “Unified segmentation.,” *NeuroImage*, vol. 26, pp. 839–51, July 2005.
- [154] C. a. Olman, L. Davachi, and S. Inati, “Distortion and signal loss in medial temporal lobe.,” *PloS one*, vol. 4, p. e8160, Jan. 2009.
- [155] J. G. Ojemann, E. Akbudak, a. Z. Snyder, R. C. McKinstry, M. E. Raichle, and T. E. Conturo, “Anatomic localization and quantitative analysis of gradient refocused echo-planar fMRI susceptibility artifacts.,” *NeuroImage*, vol. 6, pp. 156–67, Oct. 1997.
- [156] K.-J. Jung, H. Peng, T. Zhao, G. Avidan, and M. Behrmann, “Recovery of signal loss due to an in-plane susceptibility gradient in the gradient echo EPI through acquisition of extended phase-encoding lines.,” *Magnetic resonance imaging*, vol. 28, pp. 777–83, July 2010.



- [157] S. Baudrexel, S. Volz, C. Preibisch, J. C. Klein, H. Steinmetz, R. Hilker, and R. Deichmann, “Rapid single-scan T2\*-mapping using exponential excitation pulses and image-based correction for linear background gradients.,” *Magnetic resonance in medicine*, vol. 62, pp. 263–8, July 2009.
- [158] C.-Y. Yip, J. a. Fessler, and D. C. Noll, “Advanced three-dimensional tailored RF pulse for signal recovery in T2\*-weighted functional magnetic resonance imaging.,” *Magnetic resonance in medicine*, vol. 56, pp. 1050–9, Nov. 2006.
- [159] S. Posse, Z. Shen, V. Kiselev, and L. J. Kemna, “Single-shot T(2)\* mapping with 3D compensation of local susceptibility gradients in multiple regions.,” *NeuroImage*, vol. 18, pp. 390–400, Feb. 2003.
- [160] a. W. Song, “Single-shot EPI with signal recovery from the susceptibility-induced losses.,” *Magnetic resonance in medicine*, vol. 46, pp. 407–11, Aug. 2001.
- [161] J. Frahm, K. D. Merboldt, and W. Hänicke, “Direct FLASH MR imaging of magnetic field inhomogeneities by gradient compensation.,” *Magnetic resonance in medicine*, vol. 6, pp. 474–80, Apr. 1988.
- [162] N. k. Chen and A. M. Wyrwicz, “Removal of intravoxel dephasing artifact in gradient-echo images using a field-map based RF refocusing technique.,” *Magnetic resonance in medicine*, vol. 42, pp. 807–12, Oct. 1999.
- [163] Z. H. Cho and Y. M. Ro, “Reduction of susceptibility artifact in gradient-echo imaging.,” *Magnetic resonance in medicine*, vol. 23, pp. 193–200, Jan. 1992.
- [164] P. J. Reber, E. C. Wong, R. B. Buxton, and L. R. Frank, “Correction of off resonance-related distortion in echo-planar imaging using EPI-based field maps.,” *Magnetic resonance in medicine*, vol. 39, pp. 328–30, Feb. 1998.

- [165] H. Schomberg, “Off-resonance correction of MR images.,” *IEEE transactions on medical imaging*, vol. 18, pp. 481–95, June 1999.
- [166] M. Fernández-Seara and F. Wehrli, “Postprocessing technique to correct for background gradients in image-based  $R^*(2)$  measurements.,” *Magnetic resonance in medicine*, vol. 44, pp. 358–66, Sept. 2000.
- [167] J. D. Port and M. G. Pomper, “Quantification and minimization of magnetic susceptibility artifacts on GRE images.,” *Journal of computer assisted tomography*, vol. 24, no. 6, pp. 958–64, 2000.
- [168] R. Deichmann, O. Josephs, C. Hutton, D. R. Corfield, and R. Turner, “Compensation of susceptibility-induced BOLD sensitivity losses in echo-planar fMRI imaging.,” *NeuroImage*, vol. 15, pp. 120–35, Jan. 2002.
- [169] A. Moghaddam and H. Soltanian-Zadeh, “Mapping of Magnetic field Inhomogeneity and Removal of its Artifact from MR Images,” in *Proceedings of SPIE*, vol. 5032, p. 780, 2003.
- [170] N.-k. Chen, K. Oshio, and L. P. Panych, “Application of k-space energy spectrum analysis to susceptibility field mapping and distortion correction in gradient-echo EPI.,” *NeuroImage*, vol. 31, pp. 609–22, June 2006.
- [171] Y. Li, N. Xu, J. M. Fitzpatrick, V. L. Morgan, D. R. Pickens, and B. M. Dawant, “Accounting for signal loss due to dephasing in the correction of distortions in gradient-echo EPI via nonrigid registration.,” *IEEE transactions on medical imaging*, vol. 26, pp. 1698–707, Dec. 2007.
- [172] Y.-C. Hsu, C.-H. Hsu, and W.-Y. I. Tseng, “Correction for susceptibility-induced distortion in echo-planar imaging using field maps and model-based point spread function.,” *IEEE transactions on medical imaging*, vol. 28, pp. 1850–7, Nov. 2009.

- [173] H. de Leeuw and C. J. G. Bakker, “Correction of gradient echo images for first and second order macroscopic signal dephasing using phase derivative mapping.,” *NeuroImage*, vol. 60, pp. 818–29, Dec. 2011.
- [174] C. J. G. Bakker, H. de Leeuw, K. L. Vincken, E.-J. Vonken, and J. Hendrikse, “Phase gradient mapping as an aid in the analysis of object-induced and system-related phase perturbations in MRI.,” *Physics in medicine and biology*, vol. 53, pp. N349–58, Sept. 2008.
- [175] S. Volz, E. Hattingen, C. Preibisch, T. Gasser, and R. Deichmann, “Reduction of susceptibility-induced signal losses in multi-gradient-echo images: application to improved visualization of the subthalamic nucleus.,” *NeuroImage*, vol. 45, pp. 1135–43, May 2009.
- [176] E. M. Haacke, N. Y. C. Cheng, M. J. House, Q. Liu, J. Neelavalli, R. J. Ogg, A. Khan, M. Ayaz, W. Kirsch, and A. Obenaus, “Imaging iron stores in the brain using magnetic resonance imaging.,” *Magnetic resonance imaging*, vol. 23, pp. 1–25, Jan. 2005.
- [177] C. Laule, P. Kozlowski, E. Leung, D. K. B. Li, A. L. Mackay, and G. R. W. Moore, “Myelin water imaging of multiple sclerosis at 7 T: correlations with histopathology.,” *NeuroImage*, vol. 40, pp. 1575–80, May 2008.
- [178] S. Wharton and R. Bowtell, “Fiber orientation-dependent white matter contrast in gradient echo MRI.,” *Proceedings of the National Academy of Sciences of the United States of America*, vol. 2012, pp. 2–7, Oct. 2012.
- [179] P. Sati, a. C. Silva, P. van Gelderen, M. I. Gaitan, J. E. Wohler, S. Jacobson, J. H. Duyn, and D. S. Reich, “In vivo quantification of T(2)() anisotropy in white matter fibers in marmoset monkeys.,” *NeuroImage*, Aug. 2011.

- [180] J. Cohen-Adad, J. R. Polimeni, K. G. Helmer, T. Benner, J. a. McNab, L. L. Wald, B. R. Rosen, and C. Mainero, “T(2)\* mapping and B(0) orientation-dependence at 7T reveal cyto- and myeloarchitecture organization of the human cortex,” *NeuroImage*, vol. 60, pp. 1006–1014, Jan. 2012.
- [181] P. Sati, P. van Gelderen, A. C. Silva, D. S. Reich, H. Merkle, J. a. de Zwart, and J. H. Duyn, “Micro-compartment specific T2() relaxation in the brain.,” *NeuroImage*, Mar. 2013.

## Appendix I

### Power image noise correction

Magnitude images are obtained from the real and imaginary components of quadrature detection in a straightforward manner. Considering ideal, noiseless signal contributions  $A_R$  and  $A_I$ , the noiseless magnitude is:

$$|M| = \sqrt{A_R^2 + A_I^2} \quad (\text{I.1})$$

The noise contribution of quadrature detection,  $n$  results in two components,  $n_R$  and  $n_I$  with zero means and equal standard deviations,  $\sigma$ :

$$n = n_R + n_I \quad (\text{I.2})$$

$$\sigma = \sqrt{\langle n_R^2 \rangle} = \sqrt{\langle n_I^2 \rangle} \quad (\text{I.3})$$

The influence of this noise on the magnitude image is described as follows:

$$M = A_R + n_R + iA_I + in_I \quad (\text{I.4})$$

$$|M| = \sqrt{(A_R + n_R)^2 + (A_I + n_I)^2} \quad (\text{I.5})$$

The consequence of this non-linear contribution on quantitative T2 calculations is to artificially inflate signal intensity, with the effect being most severe as the decay

approaches the noise floor. However, if we consider the power of the magnitude image:

$$M^2 = (A_R + n_R)^2 + (A_I + n_I)^2 \quad (\text{I.6})$$

$$\langle M^2 \rangle = A_R^2 + A_I^2 + 2A_R \langle n_R \rangle + 2A_I \langle n_I \rangle + \langle n_R^2 \rangle + \langle n_I^2 \rangle \quad (\text{I.7})$$

$$\langle M^2 \rangle = A^2 + 2\sigma^2 \quad (\text{I.8})$$

We see that, in this case, the contribution of noise to the power image is linear and additive. The value of  $2\sigma^2$  corresponds to the magnitude of the image in the absence of signal, i.e. when  $A^2=0$ . For example, in an axial brain image, it is easily calculated from the average background intensity in the corners of the power image. Assigned a value of  $M_0^2$ , this yields a corrected power image,  $M_c$ , where

$$M_c^2 = M^2 - M_0^2 \quad (\text{I.9})$$

In the context of quantitative T2, the transformation from magnitude image to power image is equivalent to:

$$S(TE) = S_0 e^{-\frac{TE}{T_2}} \quad (\text{I.10})$$

$$S^2(TE) = S_0^2 e^{-\frac{2TE}{T_2}} \quad (\text{I.11})$$

where  $S(TE)$  is the signal at a given echo time  $TE$  and  $S_0$  is the signal for  $TE=0$ .

As such, a logarithmic fit can be performed on the power images themselves to calculate T2. In the case of GESFIDE data, corrected power images are used to calculate T2\* and T2<sup>-</sup>.

## Appendix II

### Iteratively re-weighted robust least squares

While a weighted least squares fit allows lower SNR data to have a smaller influence on the fit, a major drawback of this approach is that outliers can still have a major influence on the fit. By iteratively re-weighting the fit based on the mean absolute deviation ( $MAD$ ) of residuals, we can minimize the effect of outliers. The approach consists of the following steps:

1. Calculate initial weights based the SNR of the voxel across the image series.
2. Do an initial weighted least squares fit and compute the nominal residuals,  $r_{nom}$ .
3. Compute the standardized residual  $r_{std}$ , given by

$$r_{std} = 0.6745 \frac{r_{nom}}{K \cdot MAD(r_{nom})} \quad (\text{II.1})$$

where  $K$  is a tuning constant typically set to 4.685.


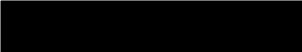
4. Compute the robust weights,  $w_i$ , based on the standardized residual.

$$w_i = \begin{cases} (1 - (r_{std})^2)^2, & |r_{std}| < 1 \\ 0, & |r_{std}| \geq 1 \end{cases} \quad (\text{II.2})$$

5. Repeat the fit, combining the initial weighting the robust weights.
6. If  $MAD(r_{std}) < MAD(r_{nom})$ , then convergence is met. Otherwise, further iterations are performed.

# Appendix III



## Ethics approval for the study of autism using MRI

|   |   |
|---|---|
|    | <b>Office of Research Ethics</b>  |
|   | The University of Western Ontario<br>Room 00045 Dental Sciences Building, London, ON, Canada N6A 5C1<br>Telephone: (519) 661-3036 Fax: (519) 850-2466 Email: ethics@uwo.ca<br>Website: www.uwo.ca/research/ethics |
| <b>Use of Human Subjects - Ethics Approval Notice</b>   |   |
| <hr/>   |   |
| <b>Principal Investigator:</b> Dr. R. Nicolson  |   |
| <b>Review Number:</b> 09519   |   |
| <b>Revision Number:</b>   |   |
| <b>Protocol Title:</b> Magnetic resonance imaging and magnetic resonance spectroscopy of the corpus callosum in autism.   |   |
| <br>  |   |
| <b>Department and Institution:</b> Psychiatry, Children's Hospital of Western Ontario   |   |
| <b>Sponsor:</b> ONTARIO MENTAL HEALTH FOUNDATION  |   |
| <b>Approval Date:</b> 08-Aug-03   |   |
| <b>End Date:</b> 28-Feb-06  |   |
| <b>Documents Reviewed and Approved:</b> Revised UWO protocol form, Letter of information & consent for patients aged 3-20 dated Feb./03, Letter of information & consent for controls aged 3-20 dated Feb./03, Assent form for controls under 13 & Assent form for patients under 13  |   |
| <hr/>   |   |
| <b>Documents Received for Information:</b>  |   |
| <p>This is to notify you that the University of Western Ontario Research Ethics Board for Health Sciences Research Involving Human Subjects (HSREB) which is organized and operates according to the Tri-Council Policy Statement and the Health Canada/ICH Good Clinical Practice Practices: Consolidated Guidelines; and the applicable laws and regulations of Ontario has received and granted full board approval to the above named research study on the date noted above. The membership of this REB also complies with the membership requirements for REB's as defined in Division 5 of the Food and Drug Regulations.</p> <p>This approval shall remain valid until end date noted above assuming timely and acceptable responses to the HSREB's periodic requests for surveillance and monitoring information. If you require an updated approval notice prior to that time you must request it using the UWO Updated Approval Request Form.</p> <p>During the course of the research, no deviations from, or changes to, the protocol or consent form may be initiated without prior written approval from the HSREB except when necessary to eliminate immediate hazards to the subject or when the change(s) involve only logistical or administrative aspects of the study (e.g. change of monitor, telephone number). Expedited review of minor change(s) in ongoing studies will be considered. Subjects must receive a copy of the signed information/consent documentation.</p> <p>Investigators must promptly also report to the HSREB:</p> <ul style="list-style-type: none"><li>a) changes increasing the risk to the participant(s) and/or affecting significantly the conduct of the study;</li><li>b) all adverse and unexpected experiences or events that are both serious and unexpected;</li><li>c) new information that may adversely affect the safety of the subjects or the conduct of the study.</li></ul> <p>If these changes/adverse events require a change to the information/consent documentation, and/or recruitment advertisement, the newly revised information/consent documentation, and/or advertisement, must be submitted to this office for approval.</p> <p>Members of the HSREB who are named as investigators in research studies, or declare a conflict of interest, do not participate in discussion related to, nor vote on, such studies when they are presented to the HSREB.</p> |   |
|    | Chair of HSREB: Dr. Paul Harding  |
| Jan 6, 2006 Sutherland, M.A., Ethics Officer HSREB<br>E-mail: jsutherl@uwo.ca   | Faxed <input checked="" type="checkbox"/> Y <input type="checkbox"/> N<br>Date: 01/06/06  |



# Appendix IV

## Ethics approval for the study of TS using MRI

|   |  |
|---|--|
|    | <b>Office of Research Ethics</b>   |
|   | The University of Western Ontario<br>Room 00045 Dental Sciences Building, London, ON, Canada N6A 5C1<br>Telephone: (519) 661-3036 Fax: (519) 850-2466 Email: ethics@uwo.ca<br>Website: www.uwo.ca/research/ethics                            |
| <b>Use of Human Subjects - Ethics Approval Notice</b>   |  |
| <hr/>   |  |
| <b>Principal Investigator:</b>  | Dr. R Nicolson   |
| <b>Review Number:</b>   | 09484  |
| <b>Revision Number:</b>   |  |
| <b>Protocol Title:</b>  | Magnetic resonance imaging and magnetic resonance spectroscopy of neuronal circuits implicated in tourette syndrome and chronic tic disorders.   |
| <br>  |  |
| <b>Department and Institution:</b>  | Psychiatry, Children's Hospital of Western Ontario   |
| <b>Sponsor:</b>   | CHILD HEALTH RESEARCH INSTITUTE  |
| <b>Approval Date:</b>   | 08-Aug-03  |
| <b>End Date:</b>  | 31-Jan-06  |
| <b>Documents Reviewed and Approved:</b>   | Revised UWO protocol form, Letter of information & consent for patients aged 5-20 dated Feb./03, Letter of information & consent for controls aged 5-20 dated Feb./03, Assent form for controls under 13 & Assent form for patients under 13 |
| <b>Documents Received for Information:</b>  |  |
| <hr/>   |  |
| <p>This is to notify you that the University of Western Ontario Research Ethics Board for Health Sciences Research Involving Human Subjects (HSREB) which is organized and operates according to the Tri-Council Policy Statement and the Health Canada/ICH Good Clinical Practice Practices: Consolidated Guidelines; and the applicable laws and regulations of Ontario has received and granted full board approval to the above named research study on the date noted above. The membership of this REB also complies with the membership requirements for REB's as defined in Division 5 of the Food and Drug Regulations.</p> <p>This approval shall remain valid until end date noted above assuming timely and acceptable responses to the HSREB's periodic requests for surveillance and monitoring information. If you require an updated approval notice prior to that time you must request it using the UWO Updated Approval Request Form.</p> <p>During the course of the research, no deviations from, or changes to, the protocol or consent form may be initiated without prior written approval from the HSREB except when necessary to eliminate immediate hazards to the subject or when the change(s) involve only logistical or administrative aspects of the study (e.g. change of monitor, telephone number). Expedited review of minor change(s) in ongoing studies will be considered. Subjects must receive a copy of the signed information/consent documentation.</p> <p>Investigators must promptly also report to the HSREB:</p> <ul style="list-style-type: none"><li>a) changes increasing the risk to the participant(s) and/or affecting significantly the conduct of the study;</li><li>b) all adverse and unexpected experiences or events that are both serious and unexpected;</li><li>c) new information that may adversely affect the safety of the subjects or the conduct of the study.</li></ul> <p>If these changes/adverse events require a change to the information/consent documentation, and/or recruitment advertisement, the newly revised information/consent documentation, and/or advertisement, must be submitted to this office for approval.</p> <p>Members of the HSREB who are named as investigators in research studies, or declare a conflict of interest, do not participate in discussion related to, nor vote on, such studies when they are presented to the HSREB.</p> |  |
|    | Chair of HSREB: Dr. Paul Harding   |
| Janice Sutherland, M.A., Ethics Officer HSREB<br>E-mail: jsutherl@uwo.ca  | Faxed: Y/N<br>Date: _____  |

# Appendix V

## Ethics approval for pulse sequence development



### Office of Research Ethics

The University of Western Ontario  
Room 4180 Support Services Building, London, ON, Canada N6A 5C1  
Telephone: (519) 661-3036 Fax: (519) 850-2466 Email: ethics@uwo.ca  
Website: www.uwo.ca/research/ethics

### Use of Human Subjects - Ethics Approval Notice

**Principal Investigator:** Dr. R.T. Thompson

**Review Number:** 16253E

**Review Level:** Expedited

**Review Date:** June 24, 2009

**Protocol Title:** Improving Magnetic Resonance Imaging Hardware and Software at 1.5 and 3 Tesla

**Department and Institution:** Nuclear Medicine, St. Joseph's Health Care London

**Sponsor:**

**Ethics Approval Date:** July 28, 2009

**Expiry Date:** June 30, 2014

**Documents Reviewed and Approved:** UWO Protocol, Letter of Information and Consent.

**Documents Received for Information:**

This is to notify you that The University of Western Ontario Research Ethics Board for Health Sciences Research Involving Human Subjects (HSREB) which is organized and operates according to the Tri-Council Policy Statement: Ethical Conduct of Research Involving Humans and the Health Canada/ICH Good Clinical Practice Practices: Consolidated Guidelines; and the applicable laws and regulations of Ontario has reviewed and granted approval to the above referenced study on the approval date noted above. The membership of this REB also complies with the membership requirements for REB's as defined in Division 5 of the Food and Drug Regulations.

The ethics approval for this study shall remain valid until the expiry date noted above assuming timely and acceptable responses to the HSREB's periodic requests for surveillance and monitoring information. If you require an updated approval notice prior to that time you must request it using the UWO Updated Approval Request Form.

During the course of the research, no deviations from, or changes to, the protocol or consent form may be initiated without prior written approval from the HSREB except when necessary to eliminate immediate hazards to the subject or when the change(s) involve only logistical or administrative aspects of the study (e.g. change of monitor, telephone number). Expedited review of minor change(s) in ongoing studies will be considered. Subjects must receive a copy of the signed information/consent documentation.

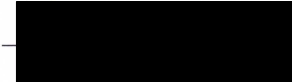
Investigators must promptly also report to the HSREB:

- a) changes increasing the risk to the participant(s) and/or affecting significantly the conduct of the study;
- b) all adverse and unexpected experiences or events that are both serious and unexpected;
- c) new information that may adversely affect the safety of the subjects or the conduct of the study.

If these changes/adverse events require a change to the information/consent documentation, and/or recruitment advertisement, the newly revised information/consent documentation, and/or advertisement, must be submitted to this office for approval.

Members of the HSREB who are named as investigators in research studies, or declare a conflict of interest, do not participate in discussion related to, nor vote on, such studies when they are presented to the HSREB.

Chair of HSREB: Dr. Joseph Gilbert



| Ethics Officer to Contact for Further Information               |   |   |  |
|---|---|---|--|
| <input type="checkbox"/> Janice Sutherland<br>(jsutherl@uwo.ca) | <input type="checkbox"/> Elizabeth Wambolt<br>(ewambolt@uwo.ca) | <input checked="" type="checkbox"/> Grace Kelly<br>(grace.kelly@uwo.ca) | <input type="checkbox"/> Denise Grafton<br>(dgrafton@uwo.ca) |

*This is an official document. Please retain the original in your files.*

cc: ORE File  
LHRI

## Vita

|                                 |  |
|---------------------------------|--|
| <b>Name:</b>                    | Yann Gagnon  |
| <b>Education</b>                | The University of Western Ontario<br>London, Ontario, Canada<br>2007-2013, Ph.D., Medical Biophysics<br><br>The University of Windsor<br>Windsor, Ontario, Canada<br>2001-2006, H.B.Sc., Physics and High Technology   |
| <b>Awards and Scholarships:</b> | Ontario Mental Health Foundation Studentship (2 year)<br><br>Western Graduate Research Scholarship<br><br>Ontario Mental Health Foundation/Autism Ontario Studentship<br><br>Ontario Council on Graduate Studies Autism Scholars Award (declined due to PhD reclassification)<br><br>Schulich Graduate Scholarship<br><br>University of Windsor Entrance Scholarship<br><br>University of Windsor Residence Scholarship<br><br>Burger King BK Scholars Award |
| <b>Related Work Experience:</b> | Graduate Research Assistant<br>Lawson Health Research Institute<br>London, Ontario, 2007-2012<br><br>Research Assistant<br>Centre for Imaging Research and Advanced Materials Characterization<br>Windsor, Ontario, 2006   |

### Submitted manuscripts

1. 'White matter lobar relaxation times in autism' submitted to *NeuroImage Clinical*.

2. 'Transverse relaxation time abnormalities of the brain in Tourette syndrome' submitted to *Brain*.
3. 'Whole brain myelin water mapping using multi-component gradient echo sampling of spin echoes (mcGESSE)' in preparation for submission to *Magnetic resonance in medicine*.

### **Refereed abstracts**

1. Gagnon, Yann, Neil Gelman, Rob Nicolson, and Jean Théberge. Feasibility of Myelin Water Quantification Using Gradient Echo Sampling of Spin Echoes. In Proceedings of the American Association of Physicists in Medicine/Canadian Organization of Medical Physicists Joint Annual Meeting. Vancouver, Canada, 2011.
2. Gagnon, Yann, Neil Gelman, and Jean Théberge. Feasibility of Myelin Water Fraction Quantification Using Multi-component Gradient Echo Sampling of Spin Echoes. In Proceedings of the International Society for Magnetic Resonance in Medicine, 19th Annual Meeting. Montreal, 2011.
3. Gagnon, Yann, and Rob Nicolson. Exploring White Matter Abnormalities in Autism Using Voxel-based Morphometry and Voxel-based Relaxometry. In Proceedings of the 9th Annual International Meeting for Autism Research. Philadelphia, USA, 2010.
4. Gagnon, Yann, Nagalingam Rajakumar, Neil Gelman, Peter Williamson, Dick Drost, Jean Théberge, and Rob Nicolson. Investigating Transverse Relaxation Time Abnormalities in Autism. In Proceedings of the International Society for Magnetic Resonance in Medicine, 18th Annual Meeting, 18:21502150. Stockholm, Sweden, 2010.
5. Gagnon, Yann, Nagalingam Rajakumar, Neil Gelman, Peter Williamson, Dick Drost, Jean Théberge, and Rob Nicolson. Investigating White Matter Abnormalities in Autism Using Voxel-based Relaxometry and Voxel-based Morphometry. In Proceedings of the IX International Congress Autism-Europe, 46. Catania, Italy, 2010.
6. Gagnon, Yann, Tim DeVito, Janet Hendry, Dick Drost, and Rob Nicolson. Quantitative Magnetic Resonance Imaging of Brain Iron Stores in Tourette Syndrome. In Proceedings of the 5th International Scientific Symposium on Tourette Syndrome. New York: Tourette Syndrome Association, 2009.
7. Gagnon, Yann, Rob Nicolson, and Dick Drost. Investigating Transverse Relaxation Time Abnormalities of White Matter in Autism. In Proceedings of the 8th International Meeting for Autism Research. Chicago, USA, 2009.

8. Spring, Robyn, Nagalingam Rajakumar, Yann Gagnon, Dick Drost, and Rob Nicolson. Transverse Relaxation Time Imaging of Frontal Lobe White Matter in Autism. In Proceedings of the 8th International Meeting for Autism Research. Chicago, USA, 2009.
9. Gagnon, Yann, Tim DeVito, Janet Hendry, Neil Gelman, Nagalingam Rajakumar, Peter Williamson, Rob Nicolson, and Dick Drost. Localization of White Matter Transverse Relaxation Time Abnormalities in Autism. In Proceedings of the International Society for Magnetic Resonance in Medicine, 16th Annual Meeting, 4:6262. Toronto, 2008.
10. Gagnon, Yann, Tim DeVito, Janet Hendry, Neil Gelman, Nagalingam Rajakumar, Peter Williamson, Rob Nicolson, and Dick Drost. Transverse Relaxation Time Abnormalities of the Basal Ganglia in Tourette Syndrome. In Proceedings of the International Society for Magnetic Resonance in Medicine, 16th Annual Meeting. Toronto, Canada, 2008.
11. Gagnon, Yann, Tim DeVito, Janet Hendry, Rob Nicolson, and Dick Drost. Localization of Transverse Relaxation Time Abnormalities in Autism. In Proceedings of the 7th International Meeting for Autism Research. London, United Kingdom, 2008.

#### **Other presentations**

1. Gagnon, Yann, Neil Gelman, Rob Nicolson, and Jean Théberge. Feasibility of Myelin Water Quantification Using Gradient Echo Sampling of Spin Echoes. Lawson Health Research Institute Talk on Fridays (TOFS) Seminar Series. London, Canada, 2012.
2. Gagnon, Yann, Neil Gelman, Rob Nicolson, and Jean Théberge. Development of a Novel Myelin Mapping Technique for the Investigation of Brain Abnormalities in Autism. University of Western Ontario Department of Medical Biophysics Seminar Series. London, Canada, 2012.
3. Gagnon, Yann, Neil Gelman, Rob Nicolson, and Jean Théberge. Investigating White Matter Abnormalities in Autism: a New Technique for Whole Brain Myelin Mapping. University of Western Ontario Neuropsychiatry Seminar Series. London, Canada, 2012.
4. Gagnon, Yann, Neil Gelman, Rob Nicolson, and Jean Théberge. Investigating Brain Tissue Abnormalities in Autism Using Magnetic Resonance Imaging. Lawson Health Research Institute Talk on Fridays (TOFS) Seminar Series. London, Canada, 2011.

5. Gagnon, Yann, Neil Gelman, Rob Nicolson, and Jean Théberge. Feasibility of Myelin Water Quantification Using Gradient Echo Sampling of Spin Echoes. University of Western Ontario Department of Medical Biophysics Seminar Series. London, Canada, 2011.
6. Gagnon, Yann, Janet Hendry, Peter Williamson, Neil Gelman, Rob Nicolson, and Jean Théberge. Transverse Relaxation Time Abnormalities of the Basal Ganglia in Tourette Syndrome. University of Western Ontario Psychiatry Research Day. London, Canada, 2011.
7. Gagnon, Yann, Neil Gelman, Rob Nicolson, and Jean Théberge. Feasibility of Myelin Water Quantification Using Gradient Echo Sampling of Spin Echoes. Lawson Research Day. London, Canada, 2011.
8. Gagnon, Yann, Jean Théberge, Rob Nicolson, and Dick Drost. Investigating White Matter Abnormalities in Autism. University of Western Ontario Neuropsychiatry Seminar Series. London, Canada, 2010.
9. Gagnon, Yann, Jean Théberge, Rob Nicolson, and Dick Drost. Investigating White Matter Abnormalities in Autism. University of Western Ontario Psychiatry Research Day. London, Canada, 2010.
10. Gagnon, Yann, Neil Gelman, Rob Nicolson, and Jean Théberge. Multi-component T2 Imaging: Quantifying the Myelin Water Fraction. University of Western Ontario Neuroimaging Journal Club. London, Canada, 2010.
11. Gagnon, Yann, Tim Devito, Neil Gelman, Rob Nicolson, and Dick Drost. Multi-component Transverse Relaxation of Brain Tissue: a Preliminary Study. University of Western Ontario Department of Medical Biophysics Seminar Series. London, Canada, 2009.
12. Gagnon, Yann, Tim DeVito, Neil Gelman, Jean Théberge, Rob Nicolson, and Dick Drost. Investigating Transverse Relaxation Time Abnormalities in Autism. University of Western Ontario Department of Medical Biophysics Seminar Series. London, Canada, 2009.
13. Gagnon, Yann, Jean Théberge, Rob Nicolson, and Dick Drost. Investigating Brain Tissue Abnormalities in Autism Using Magnetic Resonance Imaging. Lawson Health Research Institute Talk on Fridays (TOFS) Seminar Series. London, Canada, 2009.
14. Gagnon, Yann, Tim DeVito, Janet Hendry, Neil Gelman, Nagalingam Rajakumar, Peter Williamson, Rob Nicolson, and Dick Drost. Localization of Pathophysiological Abnormalities of the Brain in Autism. Western Research Forum. London, Canada, 2008.

15. Gagnon, Yann, Tim DeVito, Janet Hendry, Neil Gelman, Nagalingam Rajakumar, Peter Williamson, Rob Nicolson, and Dick Drost. Localization and Characterization of Transverse Relaxation Time Abnormalities in Autism. University of Western Ontario Department of Medical Biophysics Seminar Series. London, Canada, 2008.
16. Gagnon, Yann, Tim DeVito, Janet Hendry, Neil Gelman, Nagalingam Rajakumar, Peter Williamson, Rob Nicolson, and Dick Drost. Localization and Characterization of Pathophysiological Abnormalities in Autism Using Magnetic Resonance Imaging. University of Western Ontario Psychiatry Research Day. London, Canada, 2008.
17. Gagnon, Yann Devito, Tim Nicolson, Rob Drost, Dick. Characterizing Transverse Relaxation Time Abnormalities in Autism: a Review of Current Methods. London Imaging Discovery, 2008.
18. Gagnon, Yann, Tim DeVito, Janet Hendry, Rob Nicolson, and Dick Drost. Localization of Transverse Relaxation Time Abnormalities in Autism. Margaret Moffat Research Day. London, Canada, 2008.
19. Gagnon, Yann, Tim DeVito, Janet Hendry, Neil Gelman, Nagalingam Rajakumar, Peter Williamson, Rob Nicolson, and Dick Drost. Localization of Transverse Relaxation Time Abnormalities of the Brain in Autism. Lawson Research Day. London, Canada, 2008.
20. Gagnon, Yann, and Dick Drost. Structural Demagnetization for Optimizing SPECT/CT Imaging. London Imaging Discovery. London, Canada, 2007.

### **Professional memberships**

- Student member of the International Society for Magnetic Resonance Imaging in Medicine (ISMRM) since 2007.